
ANALYSIS OF CRYSTAL BARREL DATA

MEASUREMENT OF THE DOUBLE POLARIZATION OBSERVABLE E IN THE REACTION $\vec{\gamma}p \rightarrow \eta'p$

von

Farah Noreen Afzal

Masterarbeit in Physik

angefertigt im

Helmholtz-Institut für Strahlen- und Kernphysik

vorgelegt der

Mathematisch-Naturwissenschaftlichen Fakultät

der Rheinischen Friedrich-Wilhelms-Universität Bonn

Oktober 2012

1. Gutachter: Prof. Dr. Reinhard Beck
2. Gutachter: Prof. Dr. Jochen Dingfelder

Contents

1. Introduction	1
1.1. Photoproduction of pseudoscalar mesons	3
1.1.1. The complete experiment and polarization observables	4
1.2. Current data situation	6
1.2.1. Model calculations	7
1.2.2. The η' -MAID model	8
1.3. Structure of the thesis	9
2. The Crystal Barrel/TAPS experiment	11
2.1. The Electron Stretcher Accelerator ELSA	11
2.2. Production of a high energy photon beam	12
2.3. The target	16
2.4. Detection of decay particles	17
2.4.1. The Inner detector	18
2.4.2. Electromagnetic calorimeters	19
2.4.3. The Cherenkov detector	21
2.5. Trigger	21
3. Selection of $\gamma p \rightarrow \eta' p$ events	23
3.1. Data sets	23
3.2. Software	24
3.3. Monte Carlo	24
3.4. Reconstruction of the decay channel $\eta' \rightarrow \gamma\gamma$	25
3.5. Reconstruction of the decay channel $\eta' \rightarrow \pi^0\pi^0\eta \rightarrow 6\gamma$	38
3.5.1. Combinatorics	38
3.5.2. Selection without a kinematic fit	39
3.5.3. Selection with a kinematic fit	44
4. Extraction of the double polarization observable E	51
4.1. The countrate difference $N_{1/2} - N_{3/2}$	51
4.2. Determination of E using the dilution factor	55
4.3. Determination of E using the hydrogen data	65
4.4. Determination of E using the cross section fits	69
4.5. Comparison of the methods	70
4.6. Interpretation of the results	72
4.6.1. Comparison to fit results of Tiator et al.	72
4.6.2. Comparison of $\sigma_{1/2}$ and $\sigma_{3/2}$	74

5. Summary	77
A. Appendix	79
A.1. Example for a xml file	79
A.2. Invariant mass of 2PED events	80
A.3. Pull distributions	81
A.4. The observable E for $\pi^0 \rightarrow \gamma\gamma$	82
A.5. The acceptance for $\eta' \rightarrow \gamma\gamma$	82
A.6. The observable E for $\eta' \rightarrow \pi^0\pi^0\eta \rightarrow 6\gamma$	83
A.7. Comparison of all methods	83
Bibliography	91

1. Introduction

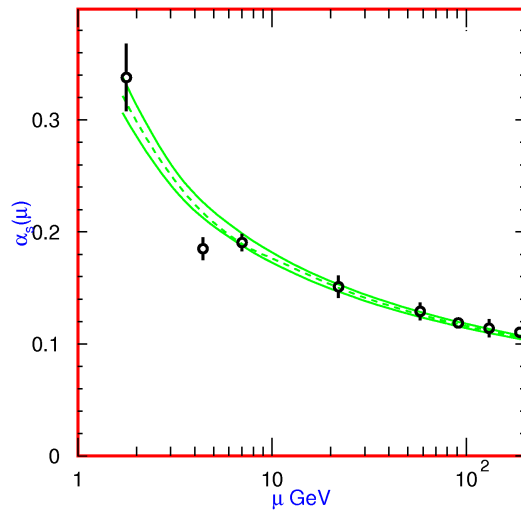
At present, matter in the universe is believed to consist of 12 elementary particles that are fermions. They are grouped on the one hand to the leptons and their antiparticles and on the other hand to the quarks and their antiparticles:

$$\begin{pmatrix} e \\ \nu_e \end{pmatrix}, \begin{pmatrix} \mu \\ \nu_\mu \end{pmatrix}, \begin{pmatrix} \tau \\ \nu_\tau \end{pmatrix}, \begin{pmatrix} u \\ d \end{pmatrix}, \begin{pmatrix} c \\ s \end{pmatrix}, \begin{pmatrix} t \\ b \end{pmatrix}. \quad (1.1)$$

In the first generation, the lightest and most stable particles are present e.g. electron and electron-neutrino, and up and down quark. The second and third generations comprise the heavier and more unstable particles that decay fast. Hence, particles from the first generation form all stable matter.

The interaction between the elementary particles is mediated through bosons. There are 4 fundamental interactions: strong, electromagnetic, weak and gravitational interaction and they are ordered here according to their strength. Furthermore, the fundamental forces differ in their range. While the gravitational and electromagnetic force have an infinite range, the strong and weak force are only dominant in short ranges like in the dimensions of the nucleon. Each force has its own mediator bosons, in the case of strong interaction, they are gluons.

Figure 1.1: The strong coupling constant as a function of the momentum transfer μ [Yea06]. At small momentum transfer, the coupling constant rises due to the confinement of quarks. At higher energies, the coupling constant is very small. This is the range of the asymptotic freedom.



Strongly interacting particles, namely gluons and quarks, carry a color charge. There are three different colors: red, green and blue and their anti-colors. A quark with a certain color has never been observed isolated, only color neutral systems of quarks have been detected until now. Consequently, either a quark and an antiquark form a bound system

1. Introduction

with integer spin (meson, e.g. η') or three quarks build one with half-integer spin (baryon, e.g. nucleon). Both mesons and baryons are grouped together as hadrons.

As already mentioned, two quarks can not be separated to form two single quarks. This is due to the fact that the strong force increases immensely at long distances or low energy and momentum transfers (≤ 1 GeV). It manifests itself in the strong coupling constant α_S describing the strength of the strong force which is shown in figure 1.1. This phenomenon is known as *confinement*. The potential energy of two quarks increases linearly with the distance. At some point the energy is high enough to form a new quark-antiquark pair. At short distances and high momentum transfers ($\gg 1$ GeV), the quarks move almost free inside a hadron. This is the range of the *asymptotic freedom*. In this range, the strong interaction can be described with quantum chromodynamics (QCD) using perturbation theory. But in the order of the nucleon mass, perturbation theory can not be used anymore and phenomenological models are needed to describe the strong interaction.

In constituent quark models, the nucleon is built of three constituent quarks that are valence quarks surrounded by a cloud of quark-antiquark pairs and gluons. The constituent quarks possess the same quantum numbers and degrees of freedoms as the valence quarks, but have different masses. They are bound through a potential inside of the nucleon which depends on the used model. One of these models is the Bonn model that is a relativistically covariant quark model [LMP01]. A linearly rising potential ensures that quark confinement is fulfilled within this model. Furthermore, the potential between the quarks is described by an instanton-induced interaction.

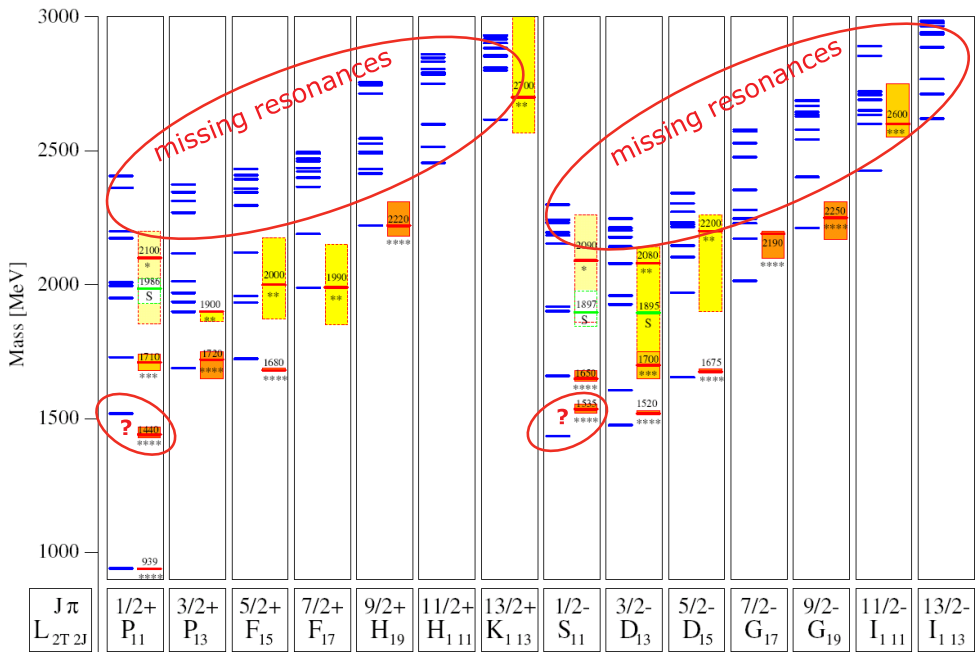


Figure 1.2.: The nucleon excitation spectrum as predicted by the Bonn model (blue lines). Experimentally observed resonances are depicted as well (red lines) with their experimental uncertainties. At higher masses, there are many predicted resonances that have experimentally not been observed so far. At lower masses, the model agrees mostly well with the known resonances. [LMP01]

Excited states or resonances of hadrons are realizable through e.g. a spin-flip or the change of the orbital angular momentum of at least one of the quarks. Figure 1.2 shows the predicted nucleon excitation spectrum (blue lines) in comparison to the experimentally observed resonances (red lines) with their uncertainties (boxes). Each resonance is characterized by its mass and the following quantum numbers: the total angular momentum $J=L+S$ with L being the orbital angular momentum and S the spin, the parity and the isospin T . The latter quantum number considers the indistinguishability of protons and neutrons with respect to the strong force. At low masses, the Bonn model agrees well with the experimental data even though sometimes deviations of the predicted and measured resonance masses occur e.g. $P_{11}(1440)$ and $S_{11}(1535)$. Especially noticeable are the many predicted resonances at masses higher than 2000 MeV that have not been observed until now. There are two possible explanations for this so called “missing resonances”-problem: The Bonn model assumes three constituent quarks. But maybe two of the three quarks inside a baryon form a diquark. Thus, the number of degrees of freedom and therefore the number of predicted states would be reduced. Another possibility suggests the weak coupling of the missing resonances to the πN -channel on which the current knowledge of nucleon resonances is mainly based on. Hence, the investigation of other channels e.g. meson photoproduction off nucleons is an important tool to gain more information about the missing resonances and to simultaneously test the quark models.

1.1. Photoproduction of pseudoscalar mesons

The CBELSA/TAPS experiment in Bonn is specialized in studying photoproduction reactions (compare figure 1.3). An incident photon beam hitting a fixed target of protons or neutrons is used to create different resonances in the intermediate state with total angular momentum J_{N^*} , parity π_{N^*} and isospin T . Thereby, either electric (E) or magnetic (M) multipole radiations induce resonance excitations. While the photon has a spin of $S_\gamma = 1$, a relative orbital angular momentum L_γ to the nucleon and parity π_γ , the nucleon has spin $S_N = 1/2$, $L_N = 0$ and parity $\pi_N = +1$ in the ground state. The excited states subsequently decay mainly via strong interaction back to the ground state by emitting e.g. pseudoscalar mesons with spin $S_M = 0$, a relative orbital angular momentum L_M and parity $\pi_M = -1$. Since different mesons can be produced by the same resonance with different strength, it is important to analyze multiple final states e.g. $\pi^0 p$, ηp or $\eta' p$.

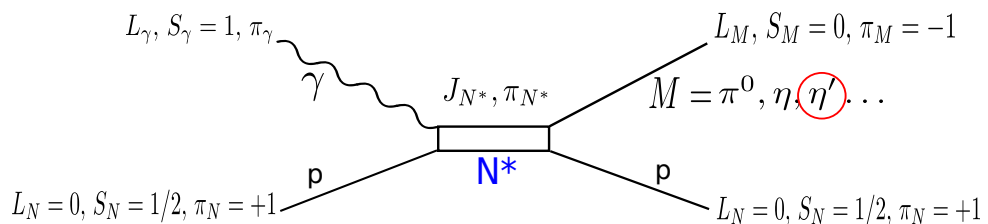


Figure 1.3.: Feynman diagram of a photoproduction reaction. For the π^0 -meson also Δ -resonances are possible in the intermediate state.

In this thesis, the emphasis is put on the photoproduction reaction $\gamma p \rightarrow \eta' p$. The η' meson is of particular interest since in this reaction it only couples to resonances with isospin $T = 1/2$ as the isospin of η' and the nucleon are $T_{\eta'} = 0$ and $T_N = 1/2$, thus reducing the number of contributing resonances. Additionally, its comparatively high mass of 958 MeV ($m_{\pi^0} = 134$ MeV) gives access to the poorly understood regime of high-lying resonances. Considering angular momentum and parity conservation in this photoproduction reaction for both initial and final state in regards to the intermediate state, the following selection rules have to be fulfilled:

$$|J_\gamma - J_N| = |J_\gamma - 1/2| \leq J_{N^*} \leq |J_\gamma + J_N| = |J_\gamma + 1/2| \quad (1.2)$$

$$|L_{\eta'} - J_N| = |L_{\eta'} - 1/2| \leq J_{N^*} \leq |J_{\eta'} + J_N| = |L_{\eta'} + 1/2| \quad (1.3)$$

$$\pi_{N^*} = \pi_N \cdot \pi_\gamma = \pi_\gamma \quad (1.4)$$

$$\pi_{N^*} = \pi_N \cdot \pi_{\eta'} \cdot (-1)^{L_{\eta'}} = (-1)^{1+L_{\eta'}}. \quad (1.5)$$

The last term includes the intrinsic parity of η' : $(-1)^{L_{\eta'}}$. For the lowest order of the photon multipoles ($L_\gamma = 1$), table 1.1 gives an overview over all quantum numbers in the initial and final state along with the photon multipoles E and M and lastly the multipoles for the photoproduction of pseudoscalar mesons. They are denoted as $E_{l\pm}$ and $M_{l\pm}$, where E and M describe the photon multipoles, $l = L_{\eta'}$ is the relative orbital angular momentum of η' relative to the nucleon, and the “+” or “-” states if the total angular momentum of the intermediate state J_{N^*} is given by adding or subtracting the nucleon spin to l .

Photon multipole	initial state $(J_\gamma^{\pi_\gamma}, J_N^{\pi_N})$	intermed. state $J_{N^*}^{\pi_{N^*}}$	final state $(J_N^{\pi_N}, L_{\eta'}^{\pi_{\eta'}})$	photoproduction multipole $E_{l\pm}, M_{l\pm}$	resonance $L_{\eta'2T,2J}(M)$
E1	$\left(1^-, \frac{1}{2}^+\right)$	$\frac{1}{2}^-$	$\left(\frac{1}{2}^+, 0^-\right)$	E_{0+}	$S_{11}(M)$
E1	$\left(1^-, \frac{1}{2}^+\right)$	$\frac{3}{2}^-$	$\left(\frac{1}{2}^+, 2^-\right)$	E_{2-}	$D_{13}(M)$
M1	$\left(1^+, \frac{1}{2}^+\right)$	$\frac{1}{2}^+$	$\left(\frac{1}{2}^+, 1^+\right)$	M_{1-}	$P_{11}(M)$
M1	$\left(1^+, \frac{1}{2}^+\right)$	$\frac{3}{2}^+$	$\left(\frac{1}{2}^+, 1^+\right)$	M_{1+}	$P_{13}(M)$

Table 1.1.: The possible resonances for $J_\gamma = 1$ and all quantum numbers of initial, intermediate and final state.

Furthermore, the masses M of these resonances should lie around or higher than 1892 MeV, since this corresponds to the threshold of η' photoproduction in the center of mass system. One way of extracting some information about the resonances’ properties is the determination of the photoproduction multipoles.

1.1.1. The complete experiment and polarization observables

In order to relate the photoproduction multipoles to experimentally measurable observables, the photoproduction process is considered from a scattering theoretical point of view

in the following. The scattering process between initial (i) and final state (f) particles is described in general with the scattering S-matrix. It is composed of two terms:

$$S = 1 + iT, \quad (1.6)$$

where the first term denotes the case of no scattering and the second one contains the dynamic of the interaction process between the initial and final state particles with the transition matrix T . Its components T_{fi} consider energy- and momentum conservation, normalization factors of the particles' wave functions, and lastly the invariant amplitude $M_{fi} \propto \langle f | F | i \rangle$ describing the momentum and spin of the particles:

$$T_{fi} = -i(2\pi)^4 \delta^{(4)}(p_f - p_i) \cdot f_{Normalization} \cdot M_{fi}. \quad (1.7)$$

The invariant amplitude for the photoproduction of a single pseudoscalar meson off a nucleon can be expressed in four complex spin amplitudes F_i with $i = 1, 2, 3, 4$ using the Chew-Goldberger-Low-Nambu (CGLN) parameterization [CGLN57]:

$$F = iF_1 \vec{\sigma} \cdot \vec{\epsilon} + F_2(\vec{\sigma} \cdot \vec{q})(\vec{\sigma}(\vec{k} \times \vec{\epsilon})) + iF_3(\vec{\sigma} \cdot \vec{k})(\vec{q} \cdot \vec{\epsilon}) + iF_4(\vec{\sigma} \cdot \vec{q})(\vec{q} \cdot \vec{\epsilon}). \quad (1.8)$$

Here, \vec{k} and \vec{q} are the momentum unit vectors of the photon and the meson, $\vec{\epsilon}$ is the polarization vector for the incoming photon and $\vec{\sigma}$ are the nucleon's spin matrices [KS03]. For a complete description of a photoproduction process, the knowledge of the absolute value of the 4 complex amplitudes, their three relative phases to each other and one global phase is required. The determination of the global phase is not possible through the measurement of observables [CT97]. Furthermore, eight observables are necessary in order to extract the relative phases and the absolute values of the 4 amplitudes uniquely. This means, the measurement of the differential cross section alone is not enough to determine the CGLN-amplitudes. Using a polarized beam and/or a polarized target gives the opportunity to measure in total 16 observables as listed in table 1.2. There are four categories of polarization observables, namely the single polarization observables where either the photon or target or recoil nucleon is polarized, and three groups containing combinations of the latter polarizations (beam-target, beam-recoil, target-recoil). According to Chiang and Tabakin [CT97], the measurement of the differential cross section together with all three single polarization observables and 4 carefully chosen double polarization observables of different categories allows the unambiguous determination of the CGLN-amplitudes except for the global phase, and is referred to as the *complete experiment* [BDS75].

category	observables			
non/single	$\frac{d\sigma}{d\Omega}$	Σ	T	P
beam-target	G	H	E	F
beam-recoil	$O_{x'}$	$O_{z'}$	$C_{x'}$	$C_{z'}$
target-recoil	$T_{x'}$	$T_{z'}$	$L_{x'}$	$L_{z'}$

Table 1.2.: In total 16 polarization observables are available.

Currently, the beam-target and all of the single polarization observables are accessible at the CBELSA/TAPS experiment that provides linearly (P_{lin}) or circularly (P_{circ}) polarized

beam photons in combination with a longitudinally (P_z) or transversely polarized target (P_x or P_y). For this case, the differential cross section is given by [BDS75]:

$$\frac{d\sigma}{d\Omega}(\theta, \Phi) = \frac{d\sigma}{d\Omega}(\theta)[1 - P_{lin}\Sigma \cos(2\Phi) + P_x(-P_{lin}\mathbf{H} \sin(2\Phi) + P_{circ}\mathbf{F}) \\ - P_y(P_{lin}\mathbf{P} \cos(2\Phi) - \mathbf{T}) - P_z(-P_{lin}\mathbf{G} \sin(2\Phi) + P_{circ}\mathbf{E})]. \quad (1.9)$$

In this thesis, the analyzed data was obtained with a circularly polarized photon beam and longitudinally polarized target. Thus, the double polarization observable E is accessible and the differential cross section reduces to:

$$\frac{d\sigma}{d\Omega}(\theta) = \frac{d\sigma}{d\Omega}(\theta)[1 - P_z P_{circ} \mathbf{E}(\theta)]. \quad (1.10)$$

The observable E is a helicity asymmetry and describes the preferred coupling of η' and the photon to spin 1/2 or spin 3/2 resonances¹. It can be parametrized with the CGLN-amplitudes as following [Fas92]:

$$E \propto -Re\{|F_1|^2 + |F_2|^2 - 2 \cos \theta F_2 F_1^* + \sin^2 \theta (F_1 F_4^* + F_2 F_3^*)\}. \quad (1.11)$$

The CGLN-amplitudes can be written as a sum of multipole amplitudes with definite angular momentum and parity. As an example the CGLN-amplitude F_1 is given here [KS03]:

$$F_1 = \sum_{l=0}^{\infty} (lM_{l+} + E_{l+})P'_{l+1} + [(l+1)M_{l-} + E_{l-}]P'_{l-1}, \quad (1.12)$$

where P_l are Legendre polynomials and P'_l their derivatives.

As a next step, the resonances' properties such as the mass, the width and photon couplings to spin 1/2 or spin 3/2 resonances ($A_{1/2}$ and $A_{3/2}$) can be extracted from the multipole amplitudes in the case of a successful performance of a complete experiment.

1.2. Current data situation

Until 6 years ago, the data situation for the photoproduction of η' off the nucleon was very poor. Only few data points describing the cross section existed based on a few hundred events [Eea68, Sea76, Pea98]. New data for the differential cross section of η' in photoproduction off a proton was obtained for a beam photon energy range of 1.5 GeV-2.2 GeV with the CEBAF Large Acceptance Spectrometer (CLAS) at the Thomas Jefferson National Accelerator facility using 2×10^5 events [Dea06]. The CLAS data improved even more in precision until 2009 covering a larger energy and angular range for the differential cross section [Wea09]. The CBELSA/TAPS collaboration also presented high precision data of the differential cross section for the photoproduction reaction $\gamma p \rightarrow \eta' p$ [Cea09] and for η' photoproduction off the deuteron [Jea11].

¹With the photon having a spin of $S_\gamma=1$ and the nucleon $S_N = 1/2$, two spin configurations with total spin of 1/2 or 3/2 are possible.

1.2.1. Model calculations

Due to apparent deviations between the CLAS and CBELSA/TAPS results, especially for higher energies (compare figure 1.4), the differential cross section was fitted separately for both results by Huang et al. [HHN12].

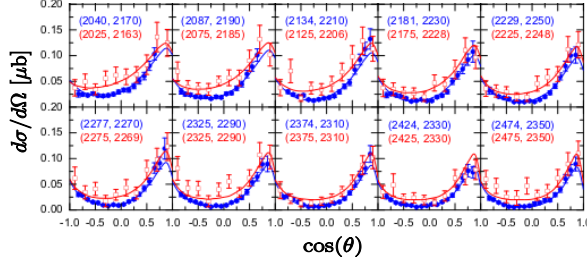


Figure 1.4.: The differential cross section for 10 energy bins obtained by CLAS (blue) and CBELSA/TAPS (red) together with the fits of Huang et.al. to both data sets (solid blue and red lines). [HHN12]

Figure 1.5 shows the cross section which was calculated by integrating the fitted differential cross section data of the CLAS and CBELSA/TAPS data, respectively. Furthermore, the fits' results were constrained by including the data of the reactions $NN \rightarrow NN\eta'$ and $\pi N \rightarrow \eta'N$, aside from the photoproduction data [Wea09, Cea09, Jea11] in their analysis. Since the lifetime of the resonances is very short ($\propto 10^{-24}$ s) as the resonances decay strongly, the resonances have a broad width and overlapping of resonances occurs as it is shown in figure 1.5.

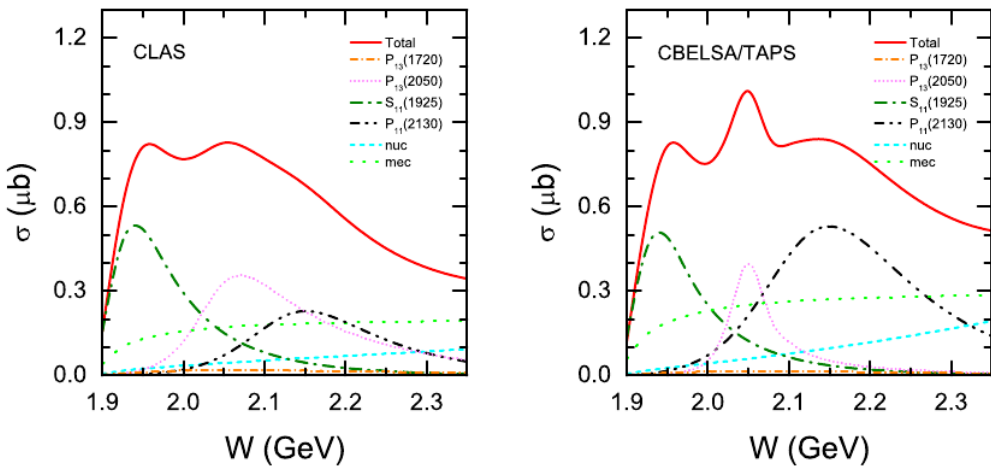


Figure 1.5.: The predicted cross section of Huang et al. after fitting the differential cross section data of CLAS and CBELSA/TAPS, respectively. The decomposition of the cross section into four resonances and nucleonic and mesonic background contributions are shown as well. [HHN12]

For the fit, background contributions from nonresonant processes such as t-channel processes where either the ρ or the ω meson is exchanged in the intermediate state, are considered. This background is referred to in figure 1.5 as “mec” which is short for mesonic current. Additionally, nucleon exchange contributions are included as well (“nuc”: nucleonic current).

It was found that at least the three resonances $P_{13}(2050)$, $S_{11}(1925)$ and $P_{11}(2130)$ together with the known sub-threshold resonance $P_{13}(1720)$ are needed to describe the data well. All resonances can be identified with listed PDG resonances ($P_{13}(2040)^*$, $S_{11}(1895)^{**}$ and $P_{11}(2100)^*$) [PDG12]. The one or two stars indicate the low knowledge of these resonances’ properties. Thus, deviations in the mass are quite imaginable.

According to the fit results, the $S_{11}(1925)$ resonance is responsible for the rise of the cross section near threshold. While the $P_{11}(2130)$ resonance dominates for higher energies, the $P_{13}(2050)$ resonance reproduces the structure of the cross section observed at $W = 2.05 \text{ GeV}$. The deviations between the CLAS and the CBELSA/TAPS data are taken into account mainly by varying the width and strength of the $P_{13}(2050)$ and $P_{11}(2130)$ resonances. Predictions for polarization observables are not yet available.

1.2.2. The η' -MAID model

Based on the earlier CLAS data [Dea06], L.Tiator et al. also performed fits to the differential cross section data using the η' -MAID model [Tia07, Tia12]. Within this model, only the t-channel background contributions are taken into account in combination with a set of resonances. All other nonresonant background is assumed to be negligible. The four resonances S_{11} , P_{13} , P_{11} and D_{13} are considered to play an important role in the photoproduction of η' .

	fit 1				fit 2			
resonance	M^* [MeV]	Γ_{tot} [MeV]	$\chi_{1/2}$	$\chi_{3/2}$	M^* [MeV]	Γ_{tot} [MeV]	$\chi_{1/2}$	$\chi_{3/2}$
$S_{11}(M^*)$	2123	132	87	-	1904	157	157	-
$P_{11}(M^*)$	-	-	-	-	2083	51	25	-
$P_{13}(M^*)$	1958	123	11	-39	1926	146	-15	10
$D_{13}(M^*)$	2143	212	102	-2	2100	91	65	-65

	fit 3			
resonance	M^* [MeV]	Γ_{tot} [MeV]	$\chi_{1/2}$	$\chi_{3/2}$
$S_{11}(M^*)$	1961	358	209	-
$P_{11}(M^*)$	2083	51	18	-
$P_{13}(M^*)$	2065	74	-30	-57
$D_{13}(M^*)$	2100	120	78	-94

Table 1.3.: The three fit results of the η' -MAID model for the mass, the width and the effective couplings $\chi \propto A$ to the resonances for both spin configurations. Fit 1 does not include a P_{11} resonance. [Tia07, Tia12]

It was found that three different fit solutions for the resonances' parameters reproduce the data equally well. This shows again, that a measurement of the cross section alone is not enough to constrain the properties of the resonances. The fit results are listed in table 4.1, the results of the fits are shown in figure 1.6a).

Most of the resonances obtained from the three fits are consistent with one of the following PDG-resonances: $S_{11}(1895)^{**}$, $P_{13}(1900)^{**}$, $P_{13}(2040)^*$, $D_{13}(2080)^{**}$, $S_{11}(2090)^*$ and $P_{11}(2100)^*$ [PDG12]. Exceptions are the $P_{13}(1958)$ from fit 1 and $S_{11}(1961)$ from fit 3, whose parameters have the greatest deviations from the PDG-values. These could be possible candidates for missing resonances.

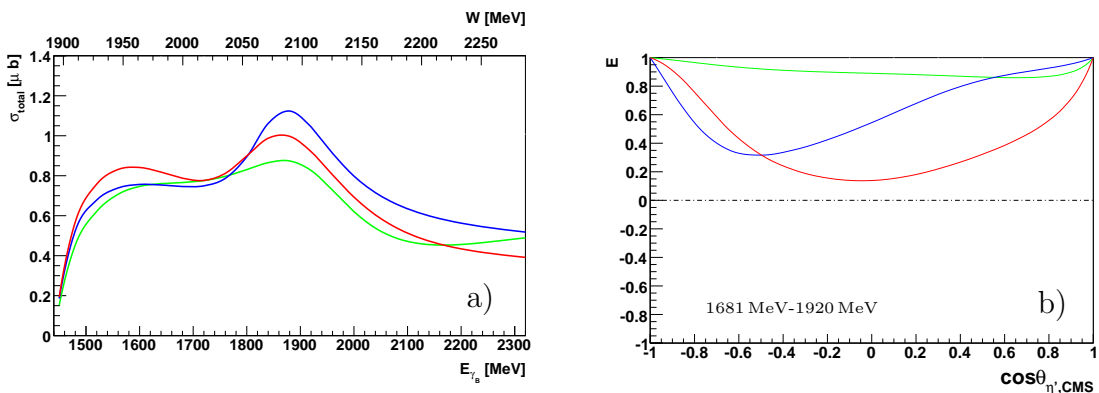


Figure 1.6.: Left: the predicted cross section of the η' -MAID model based on the differential cross section data of CLAS. All three fits (fit 1: green, fit 2: blue and fit 3: red) with different resonance properties show a similar behavior for the cross section. Right: the predictions of the double polarization observable E as a function of $\cos\theta_{\eta',CMS}$ for an energy range of 1681 MeV-1920 MeV. The colors corresponds to the same fits as in the left plot. [Tia07, Tia12]

Not only predictions for the cross section exist, but also for the polarization observables. Figure 1.6b) shows the prediction of the three fits for the polarization observable E for an energy range of 1681 MeV-1920 MeV. In contrast to the cross section, the development of E differs for all three fits. Thus, E is more sensitive to the resonances' parameters than the cross section.

1.3. Structure of the thesis

A first step towards the complete experiment in the reaction $\gamma p \rightarrow \eta' p$, is the determination of the double polarization observable E . Therefore, the reaction has to be reconstructed from the measured data with the CBELSA/TAPS experiment. An overview of the experimental setup is given in chapter 2. The decay modes $\eta' \rightarrow \gamma\gamma$ and $\eta' \rightarrow \pi^0\pi^0\eta \rightarrow 6\gamma$ were analyzed and details to the selection processes are given in chapter 3. Subsequently, the observable E is extracted from the data using three different methods and the results are compared to the η' -MAID model predictions (compare chapter 4).

2. The Crystal Barrel/TAPS experiment

For the investigation of the proton excitation spectrum, a high energy photon beam in combination with a fixed proton target is used. Thereby, a circularly polarized photon beam and a longitudinally polarized target are essential for the extraction of the double polarization observable E . Besides, the excited states are only accessible through their decay particles which are identified by a well suited detector setup. The following chapter gives an overview of the CBELSA/TAPS experiment at the Electron Stretcher Accelerator ELSA, which meets the previously mentioned demands.

2.1. The Electron Stretcher Accelerator ELSA

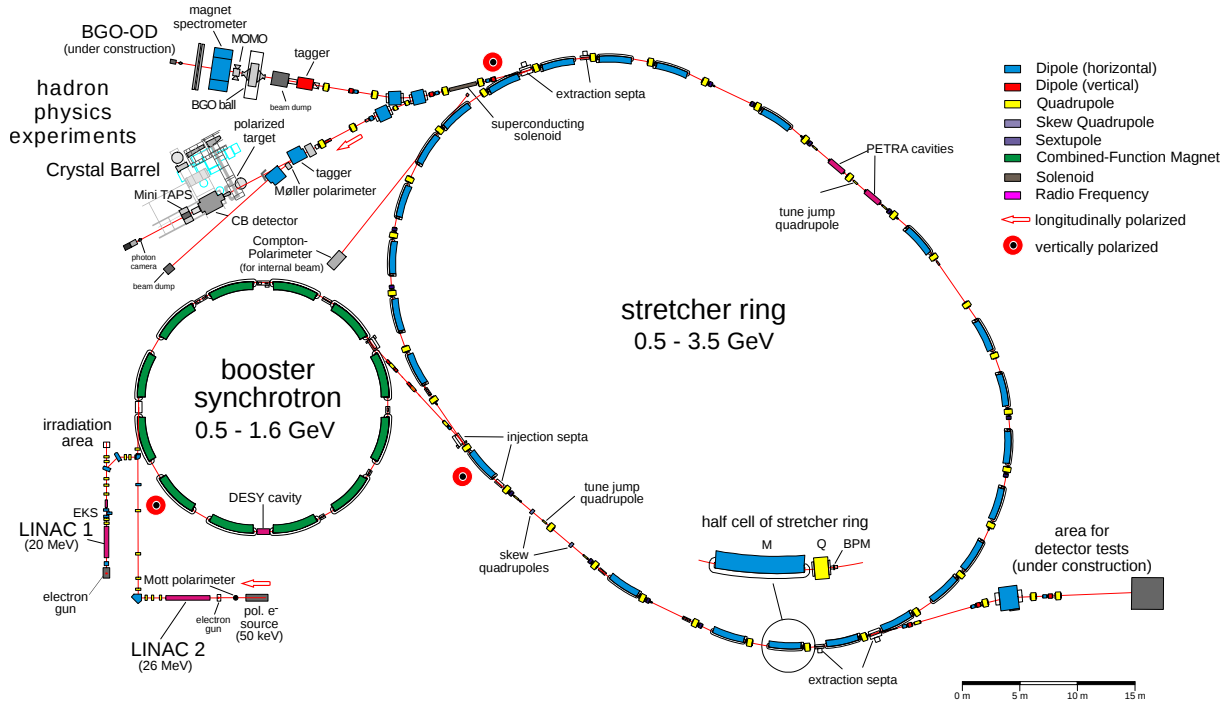


Figure 2.1.: An overview of ELSA, with two LINACs, a booster synchrotron, the stretcher ring and two hadron physics experiments.

The Electron Stretcher Accelerator ELSA (see figure 2.1) provides two electron sources and further accelerates the electrons in three stages. While the first electron source emits unpolarized electrons from a 48 keV thermal source, the second one ejects longitudinally polarized electrons which are needed for the circularly polarized photons (see section 2.2). These polarized electrons are produced using a circularly polarized laser beam directed at a GaAs-crystal which leads to photoemission. A polarization degree of 80% is achieved [Hil06] that is measured with the Mott polarimeter.

The first stage of acceleration is performed by a LINAC increasing the energy of the electrons up to 26 MeV. This pre-acceleration is required to further accelerate the electrons in the booster synchrotron. It is composed of 12 magnets which serve as bending as well as focussing magnets. The electrons reach an energy of 1.6 GeV before being injected into the stretcher ring as a pulsed beam with a frequency of 50 Hz.

The stretcher ring consists of 16 FODO-cells¹ arranged on a circumference of 164.4 m and it can be operated in three different modes: In the *stretcher mode*, the electrons are slowly extracted to the experimental area without further acceleration. The second mode is the so called *post-accelerator mode*. Thereby, the electron bunches are accumulated and accelerated again up to a maximum energy of 3.5 GeV. The CBELSA/TAPS experiment is run by this mode. During the last mode (*storage mode*), the electron beam is kept for several hours in the stretcher ring with a constant energy in order to study synchrotron-radiation [Hil00]. At the moment, only the *stretcher mode* is used.

The data analyzed in this thesis was measured with longitudinally polarized electrons. In order to transport polarized electrons through the different accelerators to the CBELSA/-TAPS experiment, the spin direction of the electrons is changed two times as depicted in figure 2.1. Since circular accelerators are only capable of conserving the vertical component of the polarization, the spin of the electron is switched from longitudinal to vertical direction and back via solenoids and dipole magnets. Besides, depolarizing effects² can occur during acceleration that cannot be compensated easily for higher energies. Therefore, the maximum beam energy of polarized electrons is limited to 2.35 GeV [Nea98].

2.2. Production of a high energy photon beam

The accelerated electrons of a constant beam energy E_0 are subsequently guided towards a radiator. The electrons interact with the radiator material mostly through bremsstrahlung since this process dominates for higher energies. The goniometer, shown in figure 2.2a, provides six different radiators which are mounted on a wheel placed inside the goniometer tank. Aside from the radiators, the goniometer contains a cromox screen and two wires inserted in two holes to monitor the electron beam position and profile.

If unpolarized photons are needed, one of the four copper radiators of different thickness (12, 50, 150 and 300 μm) is inserted in the beam-line and an unpolarized electron beam is

¹One cell is made of a horizontally focussing quadrupole (F) and either a drift pathway or a dipole magnet (O), followed by a horizontally defocussing quadrupole (D) and another drift pathway (O). Thus, focussing of the beam in both horizontal and vertical plane is achieved.

²E.g. betatron oscillation, magnet misalignments and field errors.

used. Replacing the copper radiator with a diamond crystal, which is located at the center of the wheel, yields linearly polarized photons. Lastly, it is possible to gain a circularly photon beam utilizing longitudinally polarized electrons in combination with the Møller radiator³ that consists of a $20\ \mu\text{m}$ thick ferromagnetic foil surrounded by a solenoid. In this case, the electron transfers partially its polarization p_e energy dependent onto the bremsstrahlung photon. The helicity transfer increases with the beam photon's energy which is shown in figure 2.2b. It is well understood in quantum electrodynamics and is described by

$$\frac{p_\gamma}{p_e} = \frac{E_\gamma}{E_0} \frac{(3 + 1 - E_\gamma/E_0)}{3 - (2(1 - E_\gamma/E_0)) + 3(1 - E_\gamma/E_0)^2} \quad [\text{Ols59}]. \quad (2.1)$$

In order to calculate the double polarization observable E , the determination of the photon polarization p_γ is essential. The ascertainment of the photon polarization p_γ is accomplished by measuring the electron polarization p_e and the energy of the bremsstrahlung photon E_γ [Kam09] which are explained in the next sections.

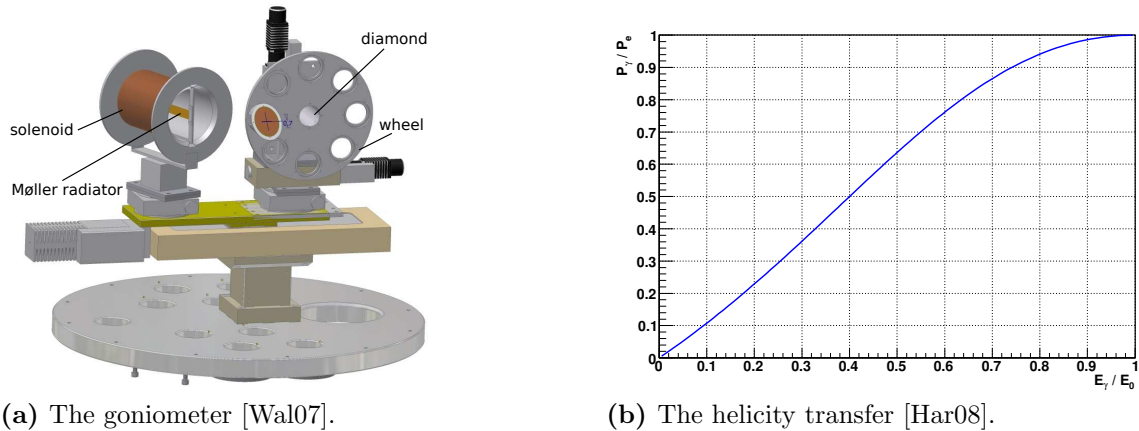


Figure 2.2.: The goniometer (left) contains all the radiators: copper, diamond and the Møller radiator, that comprises a ferromagnetic foil surrounded by a solenoid. The energy dependency of the helicity transfer from electron to bremsstrahlung photon is shown as well (right).

The tagging system

The electrons of the primary beam with known energy E_0 lose energy when producing bremsstrahlung. The knowledge of the electron energy E_e after the bremsstrahlung process allows the determination of the bremsstrahlung photon energy E_{γ_B} via $E_{\gamma_B} = E_0 - E_e$. Thereby, the recoil energy of the nucleus can be neglected. The bremsstrahlung electrons are deflected in the magnetic field of the dipole magnet according to their momenta. The bending radius of an electron and thus its momentum is determined by a hit registered in one of the organic scintillator detectors (compare figure 2.3). With the relativistic

³In general, circularly polarized photons can be produced using any radiator. The advantage of the Møller radiator is the possibility to measure the polarization degree of the electron beam as well.

energy-momentum relation the electron energy can be calculated. 96 overlapping plastic scintillator bars cover an electron energy range of $0.021 \cdot E_0$ to $0.825 \cdot E_0$ with an energy resolution of $0.1\%E_{\gamma_B}$ - $6\%E_{\gamma_B}$. In the high energy region of E_e , additional 480 plastic scintillating fibers enhance the energy resolution to $0.1\%E_{\gamma_B}$ - $0.4\%E_{\gamma_B}$ [FP04]. Both detectors are connected to photomultipliers which allows a fast readout with a time resolution of 635 ps for the scintillator bars and 1.694 ns for the fibers [Har08].

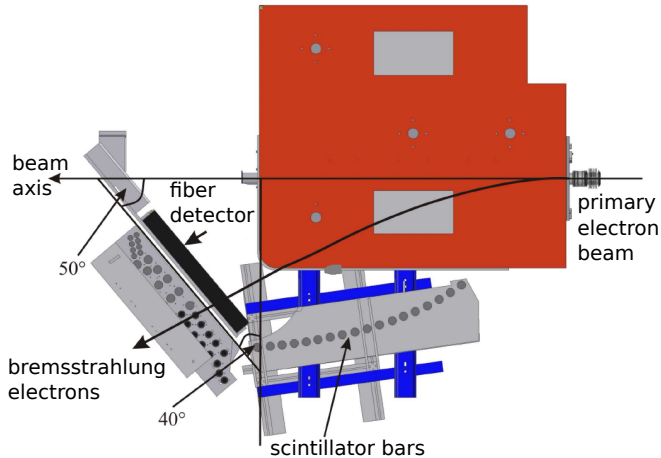


Figure 2.3: Schematic view of the tagging system consisting of a dipole magnet (red), scintillating bars and fibers [FP09]. The electrons are deflected in the magnetic field after the bremsstrahlung process.

Furthermore, the dipole magnet filters the electrons that did not interact with the radiator from the photon beam. They are guided through another dipole magnet towards the electron beam dump (see figure 2.6).

The Møller polarimeter

When the electrons hit the radiator material, they can interact via Møller scattering, which is elastic electron-electron scattering. If one uses a radiator with polarized electrons, the differential cross section for Møller scattering depends on both, the radiator and the beam polarizations (P_j^R and P_i^e). Since the electron beam helicity is changed for every spill of ELSA, the spins of the beam and the radiator electrons are aligned either parallel ($\uparrow\uparrow$) or antiparallel ($\uparrow\downarrow$) to each other. The differential cross sections for both spin configurations are given by:

$$\frac{d\sigma}{d\Omega_{(\uparrow\downarrow,\uparrow\uparrow)}} = \frac{d\sigma}{d\Omega_{unpol.}} \cdot \left(1 \pm \sum_{i,j} a_{ij} P_i^e P_j^R \right), \quad i, j = x, y, z, \quad (2.2)$$

with the tensor components a_{ij} describing the geometrical dependency of the polarization. Taking the asymmetry of the countrates for the spin configurations, yields

$$A = \frac{N_{\uparrow\downarrow} - N_{\uparrow\uparrow}}{N_{\uparrow\downarrow} + N_{\uparrow\uparrow}} = \frac{N_{\uparrow\downarrow} - N_{\uparrow\uparrow}}{2 \cdot N_{unpol.}} = \sum_{i,j} a_{ij} P_i^e P_j^R. \quad (2.3)$$

The Møller radiator is magnetized by the magnetic field of 80 Gauss provided by the solenoid [Ebe06]. This allows the alignment of the electron spins in the plane of the foil,

which can be positioned in an angle of $\alpha = \pm 20^\circ$ towards the beam direction. Hence, the radiator polarization has two components unequal 0: $P_x^R = P^R \cdot \sin \alpha$ and $P_z^R = P^R \cdot \cos \alpha$. Consequently, the asymmetry can be simplified to

$$A(\alpha) = a_{xx}P_x^e P_x^R + a_{zz}P_z^e P_z^R = a_{xx}P_x^e P^R \sin \alpha + a_{zz}P_z^e P^R \cos \alpha, \quad (2.4)$$

assuming the $a_{xz} = a_{zx}$ components are close to 0. Furthermore, it is possible to align the radiator not only at $+\alpha$, but also at $-\alpha$ and hence measure the asymmetry for both angles. Taking the average of $A(\alpha)$ and $A(-\alpha)$, the electron polarization can be calculated if the polarization P_z^R along with a_{zz} are known:

$$P_z^e = \frac{\bar{A}}{a_{zz}P^R \cos \alpha}. \quad (2.5)$$

More detailed information about the calculation process can be found in [Kam09]. The measurement of the Møller electrons is explained in the following. The scattered electrons are deflected with the dipole magnet depending on their momenta towards different angles θ . Here, θ is the angle between the electron flight and the beam direction. In the case of symmetric Møller scattering, both outgoing electrons have the same energy ($E_0/2$) as shown in figure 2.4 and are emitted at $\theta_{CMS} = 90^\circ$. At the corresponding lab angles, the Møller detector consisting of four lead glass modules is placed⁴, as shown in figure 2.4. Via coincidence measurement between the upper and the lower detectors, a Møller event is identified since the background reactions e.g. bremsstrahlung and Mott scattering emit only one electron. It is notable that an asymmetry of the countrates between antiparallel and parallel spin configurations is measurable around $\theta_{CMS} = 90^\circ$ due to the Pauli principle: The total wave function of the Møller electrons has to be antisymmetric. In the case of parallel spin alignment, the spatial wave function has to be antisymmetric. The expansion of the antisymmetric spatial wave function in Legendre polynomials only contains polynomials of uneven order⁵ which are zero for $\theta_{CMS} = 90^\circ$. Hence, the countrate for a parallel spin configuration is much smaller than for antiparallel aligned spins.

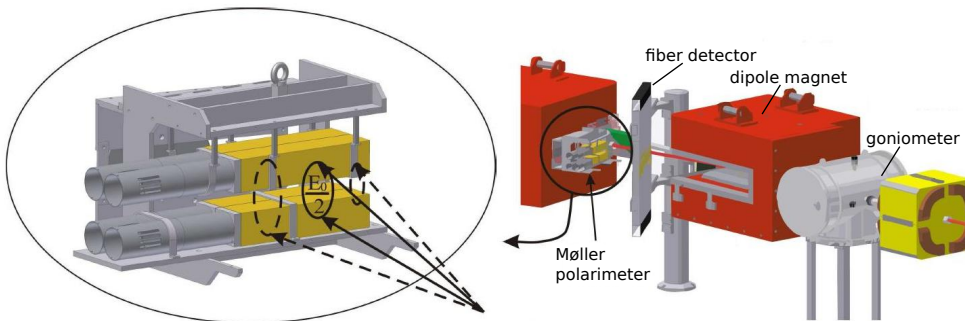


Figure 2.4.: The Møller polarimeter consisting of four lead glass modules (yellow) which are positioned behind the tagging hodoscope (right) [FP09].

⁴Only these angles are possible for Møller detection since the rest is covered by the tagging system.

⁵Since it holds for the Legendre polynomials: $P_l(-\cos \theta) = (-1)^l P_l(\cos \theta)$, the spatial wave function ($\Psi_{spatial} \propto P_l(\cos \theta)$) is antisymmetric only if l is uneven.

2.3. The target

To measure the double polarization observable E, a polarized target is needed aside from a circularly polarized photon beam. Ideally, a target made of only protons would be most suitable since reactions involving a proton are desired. But as protons have a low magnetic momentum compared to electrons due to their higher mass, it would require a high magnetic field of above 10 T in combination with very low temperatures in the region of 20 mK to polarize such a target which is experimentally not feasible [Bea99]. Besides, such target could only be a hydrogen target which is not polarizable.



Figure 2.5.: The cryostat of the butanol target (left) [Wal07] and a view of the front part of the cryostat comprising the internal holding coil and target (right) [Bea99].

Instead, a butanol target (C_4H_9OH) doped with paramagnetic radicals is used in the CBELSA/TAPS experiment. Applying a magnetic field of 2.5 T strength at a temperature of 300 mK is sufficient to polarize the electrons of the impurities to nearly 100% in the butanol target [Bea99]. The established polarization is transferred to the proton dynamically via irradiation of microwaves. Choosing the right microwave frequency leads to transitions between electron- and nucleus Zeeman levels [Roh03]. Furthermore, butanol has the advantage of having only contributions of carbon and oxygen atoms aside from hydrogen which only produce unpolarized background. Hence, only the hydrogen nuclei are polarized up to 80% in the butanol target.

The magnetic field is provided by a superconducting magnet placed around the target during the polarization mode. Whilst measurement, the magnet is removed to avoid restrictions for the angular acceptance range and the Crystal Barrel detector is positioned at its place. In order to preserve the polarization nevertheless, the frozen spin technique is implemented. Lowering the temperature below 70 mK allows the necessity of a lower magnetic field which is generated by an internal holding coil (see figure 2.5) [Bea99]. Thereby, the relaxation times increase to a few hundred hours so that the target has to be repolarized every two or three days [Har08].

The target material is placed inside a Teflon cylinder with a length of 1.88 cm and a diameter of 2 cm and it is surrounded by a cryostat which is shown in figure 2.5. The target areal density can be calculated by

$$n_{T,B} = \frac{N_A \rho l}{A} = 8.706 \cdot 10^{23} \text{ cm}^{-2}, \quad (2.6)$$

with N_A : Avogadro constant, $\rho = 0.57 \text{ g/cm}^3$: density of butanol, l :length of the target and $A = 74.1216 \text{ g/mol}$: mass number of butanol. The target areal density of the polarized part of the target is subsequently $n_{T,B} = 0.8706 \cdot 10^{23} \text{ cm}^{-2}$ since there are ten hydrogen atoms per butanol molecule.

Unpolarized liquid hydrogen and carbon target

To estimate the hydrogen component of all reactions measured with the butanol target, it is important to have reference measurements with a hydrogen and a carbon target. The hydrogen target [Ham09] is composed of a Kapton cell with a length of 5.1 cm and a diameter of 3 cm. Liquid hydrogen is filled in the cell with a heat-exchanger via two tubes. Since the binding energy of the hydrogen electron is very low with 13.6 eV in comparison to the energies involved in the experiment, the protons are assumed to be quasi-free. The target areal density is given by $n_{T,H} = 2.16 \cdot 10^{23} \text{ cm}^{-2}$ as described above, whereby the density is $\rho = 0.0708 \text{ g/cm}^3$ and $A = 1 \text{ g/mol}$.

The carbon target that is in use since the beamtime of November 2011, is made of foamed carbon. Its dimensions are chosen in a way that its areal density of $n_{T,C} = 6.173 \cdot 10^{23} \text{ cm}^{-2}$ is almost equal to the unpolarizable components of the butanol target [Jür12]. For the carbon target, the same Teflon cylinder and cryostat are used as in the case of the butanol target in order to create the same conditions when measuring with the carbon target.

2.4. Detection of decay particles

The goal of the detector setup is the identification of the decay particles of the desired photoproduction reaction (e.g. $\gamma p \rightarrow \eta' p \rightarrow \gamma\gamma p$). The detector setup specializes in detecting photons in the final state. Since photons are massless particles, the energy also corresponds to the absolute value of the momentum. The complete 4-momentum of a photon can be reconstructed if the direction of flight in polar angle θ and azimuthal angle Φ is known aside from the energy E_γ :

$$p_\gamma = \begin{pmatrix} E_\gamma \\ E_\gamma \cos \Phi \sin \theta \\ E_\gamma \sin \Phi \sin \theta \\ E_\gamma \cos \theta \end{pmatrix}. \quad (2.7)$$

Spherical coordinates are suited best here since the Crystal Barrel detector encloses the target and thus the reaction point like a stretched sphere. Furthermore, it is necessary to know whether or not the detected particles belong to the same reaction. Thus, a measurement of the time passed between production and detection of the particles is very important. Moreover, the information of the particle charge helps to distinguish between different particles.

In the next sections, an overview of the most important components of the detector system and their purpose is given.

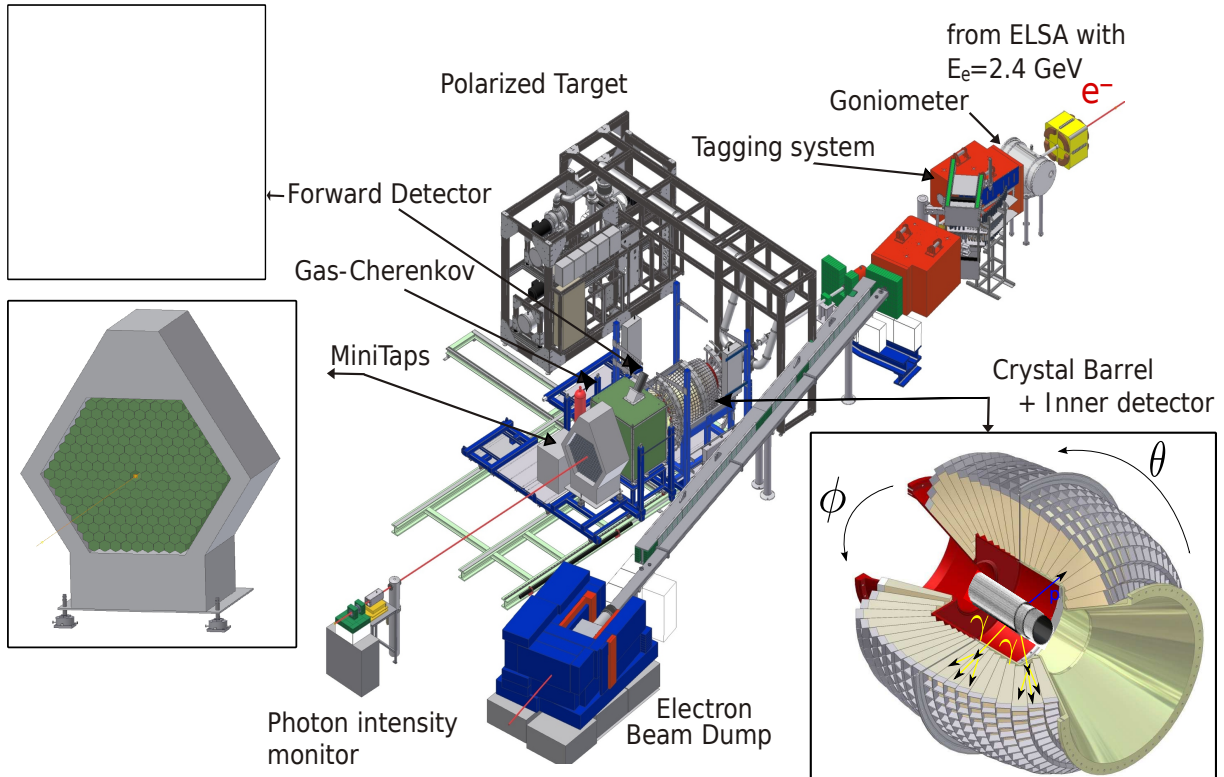


Figure 2.6.: Overview of the CBELSA/TAPS experiment.

2.4.1. The Inner detector

The Inner detector surrounds the target cylindrically and consists of 513 scintillating fibers which are organic scintillators. The core of the fiber is made of polystyrene ($n=1.6$) [Fös00], a polymer which contains benzene ring structures, and which represents the active medium. Scintillation light occurs through deexcitation of the free valence electrons of the molecule which occupy the π -molecular orbitals. A wavelength shifter is added to the solid plastic solvent to make it transparent for the scintillation light [Leo94].

The fiber core is surrounded by the cladding material Polymethylmethacrylat ($C_5H_8O_2$, $n=1.45$) [Fös00]. Due to the different refractive indices of core and cladding, a fraction of the emitted light is transported through the fibers via total reflection to lightguides which pass the light to photomultipliers. This, aside from the short decay time, ensures a fast time signal with a time resolution of 2.093 ± 0.013 ns [Har08].

Since the fiber material has a low density and a low Z , it is not well suited for the detection of photons, but for minimal ionizing particles. Thus, it is possible to distinguish charged particles (e.g. protons) from neutral particles (e.g. photons) with a certainty of 98.25% [Fös00].

Figure 2.7 shows how the fibers are placed in three layers on carbon fiber cylinders of 40 cm length. While the fibers of the outer layer are oriented parallel to the beam axis, the middle and inner layer fibers are rotated by $+25.7^\circ$ and -24.5° , respectively. The vertex of a charged particle can be determined if at least two fiber layers are hit. An angular resolution of 0.4° in θ and 0.1° in Φ is obtained with this detector. Furthermore, the Inner detector reaches an angular coverage of 23° - 166° in θ [Grü06].

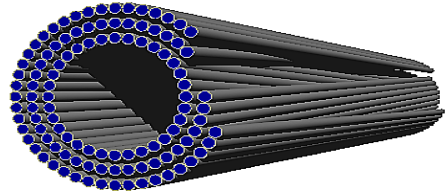


Figure 2.7.: Schematic view of the Inner detector [Wal07].

2.4.2. Electromagnetic calorimeters

The energy and the angles of the decay photons are measured with three calorimeters: Crystal Barrel, Forward detector and MiniTAPS.

Crystal Barrel

The Crystal Barrel detector encloses the Inner detector and is a homogeneous electromagnetic calorimeter consisting of 1230 thallium doped CsI crystals. Respectively, 60 crystals form one ring covering the complete azimuthal angle Φ . In total, there are 21 such rings achieving an angular coverage from 30° to 156° in polar angle θ , with the 21st ring having only 30 crystals (see figure 2.6).

The photons deposit their energy in the calorimeter by interacting with the detector material mainly via pair production and the thereby produced electrons and positrons mostly through bremsstrahlung. The combination of pair production and bremsstrahlung processes lead to the development of an electromagnetic shower.

Each crystal has a length of 30 cm which corresponds to approximately 16.22 radiation lengths. Hence, a photon with an energy of 2 GeV can be contained completely inside the detector [Aea92]. The transversal extension of the shower is ascertained with the Molière radius of 3.8 cm. The shower is usually spread over several crystals so that by determining the focal point of the shower, an angular resolution better than 2° can be reached [Jun04]. The relative energy resolution increases with the energy of the primary photon and is described by

$$\frac{\sigma_E}{E} = \frac{2.5\%}{\sqrt[4]{E/\text{GeV}}}$$

[Aea92]. The CsI(Tl) crystals are inorganic scintillators: The absorbed energy of the primary photons causes excitation of electrons into the conduction or exciton band where they move until they encounter an impurity center (thallium) and lose their energy to the impurity center which then deexcite by emitting light of 520-590 nm. The range of the wavelength of the emitted scintillation light is shifted with the help of a wavelength shifter to the sensitive range of the photodiodes. These photodiodes convert the light into

an electronic signal which is proportional to the deposited energy of the photons [Wen08].

The readout of the Crystal Barrel detector is slow due to the long decay times of the scintillation light of $1\text{ }\mu\text{m}$ and since there are slow preamplifiers that follow the photodiodes [Win06]. Therefore, the Crystal Barrel detector does not provide a time information for the detected particles.

The Forward detector

The Forward detector is a part of the Crystal Barrel and consists of 90 CsI(Tl) crystals which are arranged in three rings at an angular range of 11.18° - 27.54° in θ . The geometrical, angular resolution of each crystal is down to 5.4° in θ and 12° in Φ direction [Fun08]. There are two main differences between the Forward detector and the Crystal Barrel: Firstly, the readout of the crystals is performed with photomultipliers instead of photodiodes, thus attaining a faster readout with a time resolution of $1.861 \pm 0.016\text{ ns}$ [Har08]. This is very essential since most of the decay particles are boosted in beam direction due to the fixed target.

Secondly, 180 plastic scintillating plates are placed in front of the crystals in such way that two plates cover one crystal [Wen04]. They are used for charge identification similar to the scintillating fibers of the Inner detector. The scintillation light of the plates is guided within optical fibers to photomultipliers. The fibers are placed in a 5 mm large gap between the Crystal Barrel and the Forward detector.

The MiniTAPS detector

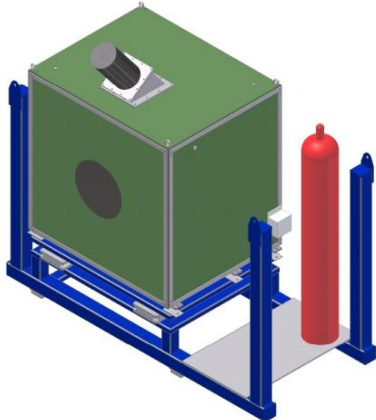
The MiniTAPS detector is located at a distance of 2.10 m from the target center and it covers almost completely the remaining angular range of $\theta = 1^\circ$ - 12° in forward direction. Together with the Crystal Barrel and the Forward calorimeter, nearly 95 % of 4π are covered in solid angle. The angular resolution is given by 0.2° in θ [Dah08].

The MiniTAPS detector comprises 216 hexagonally formed BaF₂- crystals with a height of 59 mm and a depth of 25 cm which equals 12 radiation lengths [Nov91]. BaF₂ has a fast (0.9 ns) and a slow (630 ns) scintillating component. Due to the fast one and the fast readout through photomultipliers, it is possible to achieve a time resolution of $0.872 \pm 0.006\text{ ns}$ [Har08]. The energy of the particles can be measured with a precision of [Dre04]

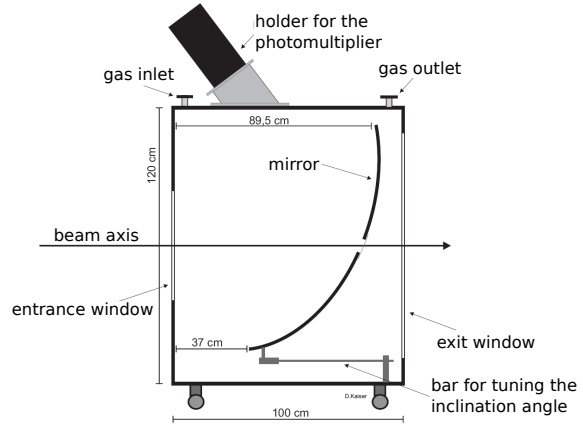
$$\frac{\sigma_E}{E} = 1.12\% + 2.54\% \cdot E^{-1/2}[\text{GeV}]. \quad (2.8)$$

Plastic scintillators with a thickness of 5 mm are attached in front of the crystals for the determination of charged particles passing through the detector. Moreover, a time resolution of $3.06 \pm 0.05\text{ ns}$ is reached with these scintillators [Har08].

2.4.3. The Cherenkov detector



(a) Cherenkov detector [Wal07].



(b) Schematic view [Kai07].

Figure 2.8.: Electrons and positrons passing through the Cherenkov detector emit Cherenkov light that is collected with a parabolic mirror and passed to the photomultiplier.

When a high energy beam photon hits the target, especially a solid state target like butanol, a lot of electromagnetic background is created via interaction of the beam photon with the target through pair production and Compton scattering. These electrons and positrons are highly relativistic and therefore boosted to very small θ angles. In order to prevent the further process of all emitted trigger signals coming from the MiniTAPS detector, a gas Cherenkov detector is placed between the Crystal Barrel and the MiniTAPS detector. It is filled with CO₂ which gives a veto signal only if an electron or positron passes the detector with an energy higher than 17.4 MeV⁶. The emitted Cherenkov light is focused on the photomultiplier with a concave mirror (see figure 2.8b). Electrons and positrons are detected with an efficiency of $99.72 \pm 0.45\%$. [Kai07]

2.5. Trigger

The trigger is composed of a Field Programmable Gate Array (FPGA) module which evaluates whether or not the registered signals of the detectors belong to a desired event [Win06]. The evaluation process is performed as follows. The first-level trigger involves all detectors except for the Crystal Barrel detector since the signal processing time should not be above 250 ns. It qualifies the detector signals based on certain conditions. The conditions for the trigger *trig42c* are listed in table 2.1. Thereby, each trigger condition involves a coincidental signal of the tagging system and a anti-coincidental with the Cherenkov signal. In the case of the trigger *trig41*, the Cherenkov signal is left out [Har08].

⁶Pions emit Cherenkov light at energies above 4.7 GeV.

If the condition of the first trigger level is fulfilled, the cluster multiplicity is considered in the second trigger level. The electromagnetic shower initiated by a photon is usually spread over several crystals in the Crystal Barrel detector, thus coincidental signals are emitted from these crystals which are described as one cluster. Sometimes, the shower of several particles overlap. Then, the energy of a single particle, which is called Particle Energy Deposit (PED), is determined through local maxima within one cluster. The number of clusters is ascertained by the Fast Cluster Encoder (FACE) within $6 \mu\text{s}$ [Fle01]. It determines the shower focal point, counts the number of crystals involved in a cluster and gives the number of total clusters. The trigger needs in total about $10 \mu\text{s}$ to determine if one event should be stored. In the case of rejection the detector electronics is reset. Else, the data of all detectors is stored by the data acquisition.

	first-level trigger	second-level trigger
1	tagging system + !Cherenkov + Inner(1)	≥ 2
2	tagging system + !Cherenkov + MT(1)	≥ 1
3	tagging system + !Cherenkov + FD(1)	≥ 1
4	tagging system + !Cherenkov + FD(2)	-
5	tagging system + !Cherenkov + FD(1) + MT(1)	-
6	tagging system + !Cherenkov + MT(3)	-

Table 2.1.: Overview of the different trigger conditions [Win06] for the so called trig42c data trigger. In the first trigger level, a signal from the tagging system and no signal from the Cherenkov detector are required in combination with at least one hit (in brackets) in one of the other detectors (Inner detector (Inner), Forward detector (FD) or MiniTAPS (MT) detector). Once one of these conditions is fulfilled, the number of clusters in the Crystal Barrel detector is considered in the second level trigger.

3. Selection of $\gamma p \rightarrow \eta' p$ events

In this chapter, an overview of the selection process for suitable events regarding the $\eta' p$ final state is given. Table 3.1 shows the η' decay channels with the highest branching ratios. Since the energy of π^\pm is not always contained completely in the calorimeter crystals, it is not possible to reconstruct the decay modes number I, II or IV a). The two decay channels $\eta' \rightarrow \gamma\gamma$ and $\eta' \rightarrow \pi^0\pi^0\eta \rightarrow 6\gamma$, both with only photons in the final state, can be measured and reconstructed with the CBELSA/TAPS experiment. The decay mode number IV b) also has photons in the final state but compared to the III and V decay mode, the branching ratio is lower and therefore it is not analyzed in this thesis.

No.	decay mode	Branching ratio
I	$\pi^+\pi^-\eta$	43.2%
II	$\rho^0\gamma(\rightarrow \pi^+\pi^-\gamma)$	29.3% (29.3%)
III	$\pi^0\pi^0\eta(\rightarrow 6\gamma)$	21.7% (8.6%)
IV a) b)	$\omega\gamma(\rightarrow \pi^+\pi^-\pi^0\gamma)$ $\omega\gamma(\rightarrow \pi^0\gamma\gamma)$	2.8% (2.5%) 2.8% (0.23%)
V	$\gamma\gamma$	2.2%

Table 3.1.: The decay modes of η' and the corresponding branching ratios [PDG12]. In brackets the most probable decay channels of the intermediate states together with the branching ratios for these particular decay channels are given.

3.1. Data sets

The data analysis described in the next sections is based on mainly three beamtimes with the CBELSA/TAPS experiment from 2007 to 2009 (see table 3.2). In all three cases, the measurements were done with the longitudinally polarized butanol target in combination with a circularly polarized photon beam achieving an energy up to 2.35 GeV. In order to avoid systematic effects, the data was taken for both positive and negative target polarizations. Besides, both right- and lefthanded circularly polarized beam photons are available since the electron polarization direction can be rotated every other spill by 180°. Additionally, it is necessary to analyze data taken with the hydrogen (beamtime November 2008) and carbon target (beamtime November 2011) in order to determine the dilution factor which is needed to ascertain the double polarization observable E (see next chapter). All data sets used either *trig42c* or *trig41*.

Beamtime	Target	Target polarization	Files
24.11.2007 - 18.12.2007	Butanol	positive	1038
	Butanol	negative	809
22.09.2009 - 09.10.2009	Butanol	positive	657
	Butanol	negative	846
12.11.2009 - 18.12.2009	Butanol	positive	1615
	Butanol	negative	1606
5.11.2008 - 27.11.2008	Hydrogen	unpolarized	629
11.11.2011 - 28.11.2011	Carbon	unpolarized	1212
28.11.2011 - 13.12.2011	Carbon	unpolarized	586

Table 3.2.: Overview of amount of data taken at beamtimes in November 2007, September 2009 and November 2009 with the butanol target, November 2008 with the hydrogen target and November 2011 with the carbon target.

3.2. Software

The measured raw data is first saved as a zebra file and after applying a preselection process it is saved as a ROOT file. The software ExPlORA¹, which was specially constructed for the CBELSA/TAPS experiment, is used to analyze the data. It is based on the objectoriented CERN-framework ROOT and it is controlled by many interleaved xml files [Pio07]. Besides, it is easily possible to extend it by using plugins written in C++, so that one can individually adapt ExPlORA to their needs. In this thesis the xml files are used for combining all involved particles of a photoproduction reaction in all possible ways and the plugin for applying cuts and filling histograms.

An example for a xml file is given in the appendix (compare figure A.1). For the determination of the double polarization observable E additional ROOT macros were written.

3.3. Monte Carlo

In order to apply acceptance corrections and for the purpose of comparison, it is important to generate simulated data. This is done with the event simulation package CBGEANT which is based on GEANT3². The Crystal Barrel, the Forward, the Inner, the MiniTAPS and the Cherenkov detector are implemented in CBGEANT aside from the different targets. This allows an investigation of the kinematics of the decay particles and an evaluation of the detection efficiency for a certain reaction. Thus, it helps to perform acceptance corrections on the data. For the beam photons an energy range from 1447 MeV to 2320 MeV is chosen since the production threshold of η' lies at 1447 MeV. Besides, the number of generated beam photons have a $1/E_{\gamma_B}$ - dependency due to the

¹Extended Pluggable Objectoriented Root Analysis

²GEometry ANd Tracking, which was constructed for CERN

bremsstrahlung process.

The following reactions were generated with 5×10^6 events each:

- $\gamma_B p_{in} \rightarrow p_{out} \eta' \rightarrow p_{out} \gamma\gamma$
- $\gamma_B p_{in} \rightarrow p_{out} \eta' \rightarrow p_{out} \pi^0 \pi^0 \eta \rightarrow p_{out} 6\gamma$

For a better understanding of the background in the data, 2×10^6 events were generated of:

- $\gamma_B p_{in} \rightarrow p_{out} \omega \rightarrow \pi^0 \gamma p_{out} \rightarrow p_{out} 3\gamma$
- $\gamma_B p_{in} \rightarrow p_{out} \eta \rightarrow \pi^0 \pi^0 \pi^0 p_{out} \rightarrow p_{out} 6\gamma$
- $\gamma_B p_{in} \rightarrow p_{out} \pi^0 \pi^0 \pi^0 \rightarrow p_{out} 6\gamma$
- $\gamma_B p_{in} \rightarrow p_{out} \pi^0 \pi^0 \eta \rightarrow p_{out} 6\gamma$.

To compare the simulated reactions with the data, all reactions have been simulated with the hydrogen, the carbon and the butanol target.

3.4. Reconstruction of the decay channel $\eta' \rightarrow \gamma\gamma$

In the case of η' decaying into two photons, there are three particles in the final state, namely one proton and two photons. Therefore, the analysis is confined to 3PED events. For events, where the proton is not detected (2PED events), the spectra have a significant lower signal to background ratio (compare figure A.2). Thus, they are not taken into account for the further analysis.

In order to reconstruct the complete reaction $\gamma_B p_{in} \rightarrow \eta' p_{out}$, the knowledge of the initial and final state is required. The initial state is kinematically defined by the beam photon which has an energy of E_{γ_B} and hits the resting target proton with mass $m_p = 938.27 \text{ MeV}$ in z direction (at $\theta = 0^\circ$):

$$p_{\gamma_B} = \begin{pmatrix} E_{\gamma_B} \\ 0 \\ 0 \\ E_{\gamma_B} \end{pmatrix}, p_{p_{in}} = \begin{pmatrix} m_p \\ 0 \\ 0 \\ 0 \end{pmatrix} \quad (3.1)$$

The energy of the beam photons is calculated from the registered hits in the tagging system (compare 2.2). Often more than one beam photon correlates to an event in the detector setup. Therefore, new reactions are created, each of them having the same final state particles but a different beam photon in the initial state. In average around 15 beam photons are assigned to the same final state particles without applying any kinematics cuts.

The final state particles are divided into two groups: uncharged and charged particles. Two uncharged (photons) and one charged (proton) particles are selected for reconstructing the desired reaction. Thereby, reactions involving neutrons instead of protons are

3. Selection of $\gamma p \rightarrow \eta' p$ events

suppressed³.

The four-momenta of the two photons are given by equation (2.7). Adding the two four-momenta of the photons p_{γ_1} and p_{γ_2} yields the invariant mass $m_{\gamma\gamma}$:

$$\begin{aligned} m_{\gamma\gamma} &= \sqrt{(p_{\gamma_1} + p_{\gamma_2})^2} \\ &= \sqrt{(E_{\gamma_1} + E_{\gamma_2})^2 - (\vec{p}_{\gamma_1} + \vec{p}_{\gamma_2})^2}. \end{aligned} \quad (3.2)$$

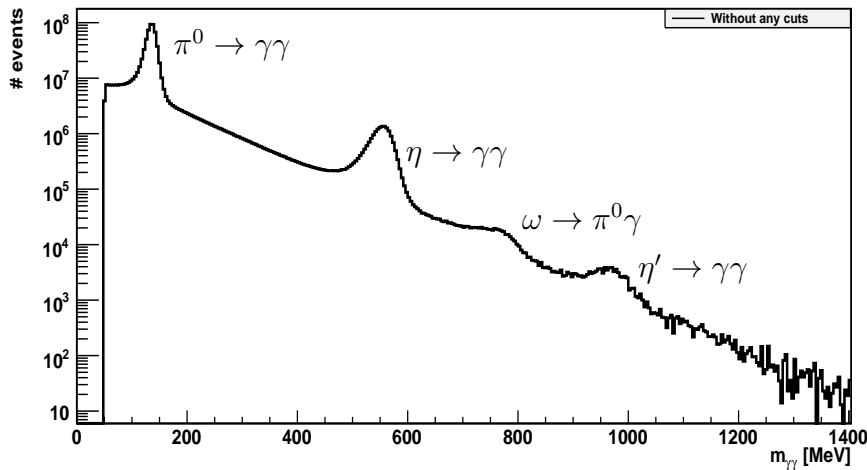


Figure 3.1.: The invariant mass is shown after the charge cut. Whereas the π^0 - and the η -peaks are clearly visible, the η' - and the ω -peaks are slightly visible as well.

The invariant mass spectrum for the butanol target is shown in figure 3.1. Since not only η' decays into two photons but also π^0 (98.8%) and η (39.3%), there are peaks visible at 135 MeV and 548 MeV aside from the η' -peak at 958 MeV [PDG12]. A fourth peak is located at approximately 780 MeV which belongs to $\omega \rightarrow \pi^0\gamma$ (8.2%) [PDG12]. The angular resolution is sometimes not high enough to distinguish between the two photons belonging to the π^0 of the ω decay. Thus, they are regarded as one photon so that together with the third photon the ω is seen in the $\gamma\gamma$ spectrum. Besides, it could also be the case that one of the three photons with very low energy was not detected.

All peaks are located above a background which contains incompletely reconstructed reactions aside from combinatorial background of the beam photons. The countrate decreases with higher masses due to the $1/E_{\gamma_B}$ -dependency of the bremsstrahlung beam photons' cross section.

Since the signal to background ratio is low for η' , it is necessary to reduce the background with suitable cut conditions that are presented in the following.

³The beam photons can interact with neutrons as well in the case of the butanol and the carbon target.

Time of the particles

The CBELSA/TAPS experiment has several detectors which provide time information of the particles with Time to Digital Converters (TDCs) or multi-hit TDCs. A TDC quantifies the time difference between a “start”- and a “stop”-signal. The same signal is used as start-signal for all detectors. As soon as a detector registers a hit, a stop-signal is given out in reference to the start-signal. The time difference of both signals is shown e.g. for the beam photon in figure 3.2 a). A prompt peak is clearly visible around 0 ns. Since the tagging system has a very high count rate, a lot of timely uncorrelated events are registered as well. They form a flat background not only beside the prompt peak but also underneath it as depicted in figure 3.2 a). The decrease at the left side of the prompt peak marks the dead time of the tagging system. Therefore only a few entries exist there. The time information of the decay particles is provided by several detectors. The superposition of all individual detector time spectra are shown in figure 3.2 b)-d). As the tagging system has a better time resolution compared to the other detectors (compare section 2.2), the prompt peaks of the decay particles are not as defined and thin as the one of the beam photons’ spectrum. The structures at the right side of the prompt peak are physically of no significance. They occur due to reflections in the Inner or in the MiniTAPS detector.

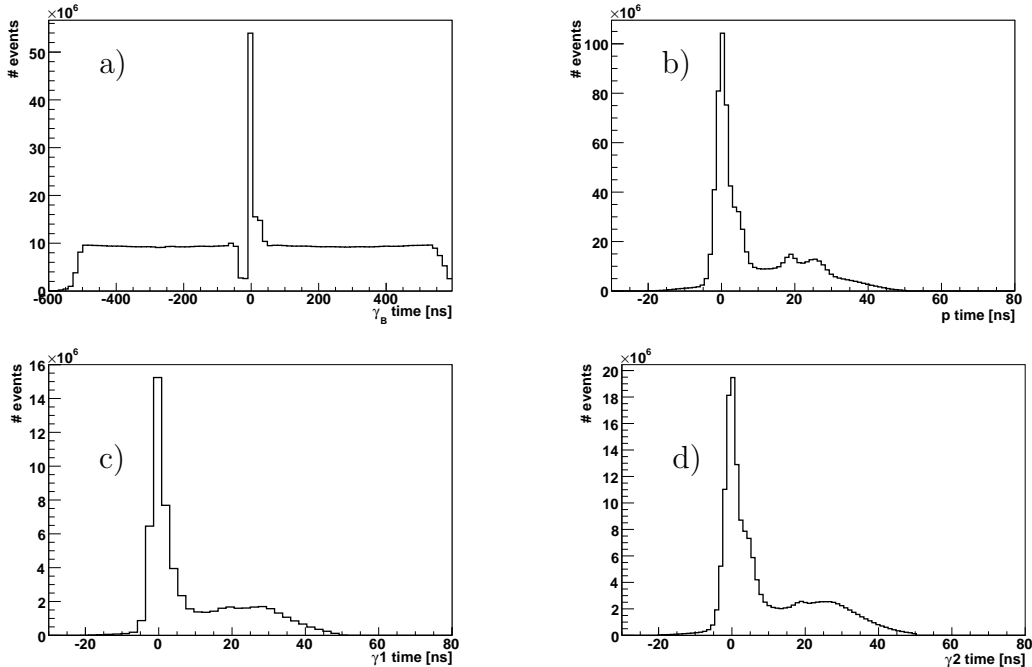


Figure 3.2.: Time of all the particles involved in a reaction: a) shows the beam photon, b) the proton and c) and d) the γ_1 and γ_2 time spectra, respectively. Thereby, the numbering of the decay photons is chosen randomly.

Since particles belonging to one reaction should be coincidental within a certain time frame, a cut of $-20 \text{ ns} < t_{particle} < 50 \text{ ns}$ is applied at first for all decay particles. Secondly,

3. Selection of $\gamma p \rightarrow \eta' p$ events

a cut to the reaction time is applied, whereas the reaction time is defined by

$$t_{reaction} := t_{\gamma_B} - t_{decayparticle}. \quad (3.3)$$

and is shown in figure 3.3. The protons always have a time information because all the charge sensitive detectors (Inner, Forward and MiniTAPS detector) have a fast readout and thus provide a time information. The reconstructed η' only has a time information if at least one the photons is detected in the Forward or in the MiniTAPS detector. If both photons have a time information, then the mean value is assigned to η' . Thereby, it is ensured that the photons' times do not differ more than 20 ns from each other. Since photons move with the velocity of light, their time signal does not underlie fluctuations. In contrast to this, protons have different time of flights depending on which detector they hit. They need for instance approximately up to 16 ns to reach the MiniTAPS detector. Therefore, the time of η' is used for $t_{decayparticle}$ whenever available. Otherwise the proton time is used.

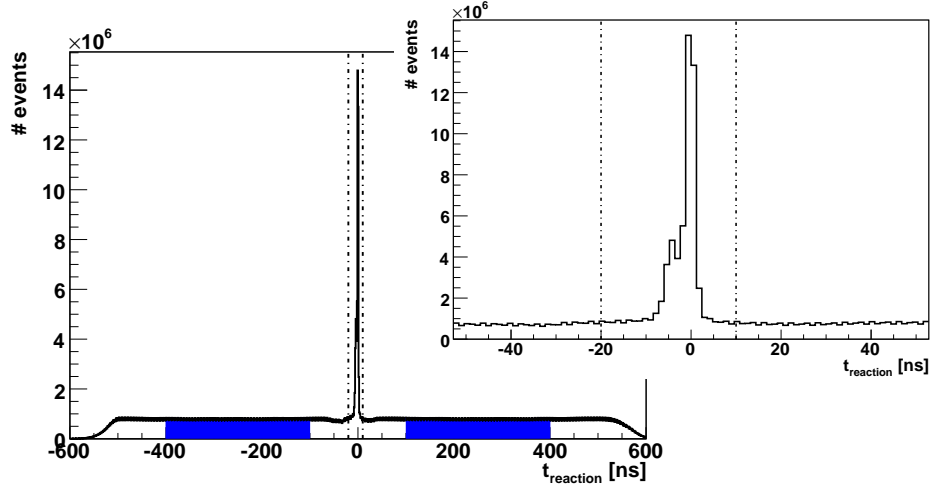


Figure 3.3.: The reaction time is depicted here together with the cut boundaries as dotted lines. Zoomed in (small plot), a small sidepeak is visible which originates from the time of flight of the protons. The blue areas of the sidebands are used to estimate and subtract the background located underneath the prompt peak.

Considering the proton time of flight, a cut of $-20 \text{ ns} < t_{reaction} < 10 \text{ ns}$ is applied (see figure 3.3). However, this cut alone does not eliminate all time background since a part of the background is located underneath the prompt peak as well. This background is estimated by assuming that it is as uniformly distributed as the background in the sidebands left and right from the prompt peak is. A sideband subtraction is used in order to get rid of this background in all histograms: Events belonging to the sidebands within a range from -400 ns to -100 ns and from 100 ns to 400 ns (compare blue area in figure 3.3) are filled in one histogram and in another the prompt peak events are filled (H_{prompt} , red curve in figure 3.4). $H_{sideband}$ is subsequently scaled down in order for the blue area to be equally large as the area underneath the prompt peak ($H_{sideband}$, blue curve in figure

3.4). Thus, the background corrected histogram ($H_{corrected}$, green curve in figure 3.4) is filled with

$$H_{corrected} = H_{prompt} - s \cdot H_{sideband}, \quad (3.4)$$

whereas s is the scaling factor of $s = \frac{30ns}{600ns} = \frac{1}{20}$ and corresponds to the ratio of prompt peak range to the sum of sideband ranges. This entire procedure will be referred to as the time-cut from now on.

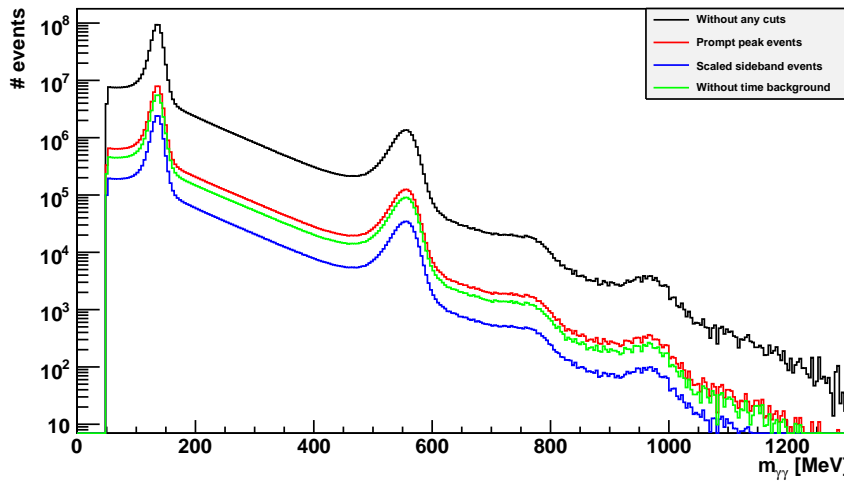


Figure 3.4.: The invariant mass distribution is shown for the prompt peak events (red), the sideband events (blue), the background corrected histogram (green) and before the time-cut is applied to the data (black).

Comparing the invariant mass spectrum before and after the time-cut, shows that the time-cut reduces time coincidental events beside and underneath the η' -peak. Thus, multiple countings of the same reaction is reduced.

For the further analysis, only the background corrected histograms are shown.

Missing mass

The outgoing protons p_{out} of the reaction $\gamma_B p_{in} \rightarrow \eta' p_{out}$ can have a kinetic energy from 0 MeV up to 1442 MeV which follows from energy conservation:

$$\begin{aligned} E_{\gamma_B} + m_p &= E_{kin,p} + E_{kin,\eta'} + m_p + m_{\eta'} \\ \Leftrightarrow E_{\gamma_B} - m_{\eta'} &= E_{kin,p} + E_{kin,\eta'}. \end{aligned} \quad (3.5)$$

Here, the beam photon energy E_{γ_B} lies in the range of $1447 \text{ MeV} < E_{\gamma_B} < 2320 \text{ MeV}$ (compare section 3.4) and the η' mass is $m_{\eta'} = 957.78 \text{ MeV}$. A comparison of the measured kinetic energy of the protons to the calculated kinetic energy (see figure 3.5) shows that

3. Selection of $\gamma p \rightarrow \eta' p$ events

protons can only be stopped completely in the calorimeters if their kinetic energy is lower than approximately 400 MeV. Protons are minimal-ionizing particles and do not initiate an electromagnetic shower like the photons. For higher kinetic energies, the protons only deposit an energy of about 250 MeV in the crystals. Since it is not possible to know if indeed the complete energy of the proton is contained in the detectors, the proton four-momentum can not be reconstructed from the measured proton energy.

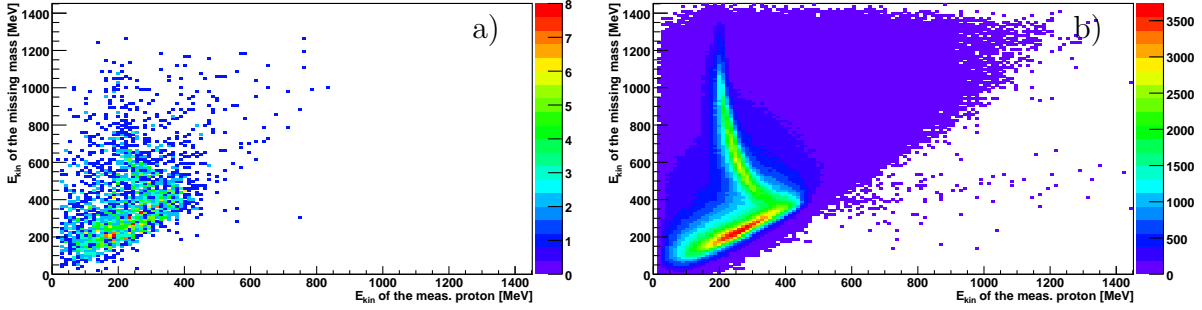


Figure 3.5.: The kinetic energy of the calculated proton (missing mass see (3.7)) as a function of the measured kinetic energy of the proton is shown for the butanol a) and for the Monte Carlo butanol data b).

But since the four-momenta of the initial state particles together with the four-momentum of η' are known, the missing proton four-momentum can be calculated as follows:

$$\begin{pmatrix} E_{p_{out}} \\ \vec{p}_{p_{out}} \end{pmatrix} = \begin{pmatrix} E_{\gamma_B} \\ \vec{p}_{\gamma_B} \end{pmatrix} + \begin{pmatrix} m_p \\ 0 \end{pmatrix} - \begin{pmatrix} E_{\eta'} \\ \vec{p}_{\eta'} \end{pmatrix} \quad (3.6)$$

The mass of this vector, the so-called missing mass $m_{missing}$, should be distributed around the proton mass and is used to impose another constraint.

$$m_{missing} = \sqrt{(E_{\gamma_B} + m_p - E_{\eta'})^2 - p_{x,\eta'}^2 - p_{y,\eta'}^2 - (E_{\gamma_B} - p_{z,\eta'})^2} \quad (3.7)$$

Figure 3.6 shows the missing mass spectrum after applying all cuts. A clear peak is visible around 938 MeV. Besides, the missing mass spectrum is slightly asymmetric at higher masses because more background exists there. This can be explained through the dependency of the missing mass on the beam photon energy (compare equation (3.7)). After applying a cut on the beam photon energy (see section 3.4), a beam photon is assigned more often falsely to a set of decay particles for higher beam photon energies than for lower ones (compare figure 3.12). This results in a higher calculated missing mass.

As figure 3.6 shows, a false assignment only happens rarely. These events are rejected by the means of a 3σ -cut on the missing mass of $797 \text{ MeV} < m_{missing} < 1079 \text{ MeV}$. The cut boundaries are determined by fitting a Gaussian curve to the hydrogen target data

in order to choose events involving the hydrogen protons of butanol and not the carbon protons.

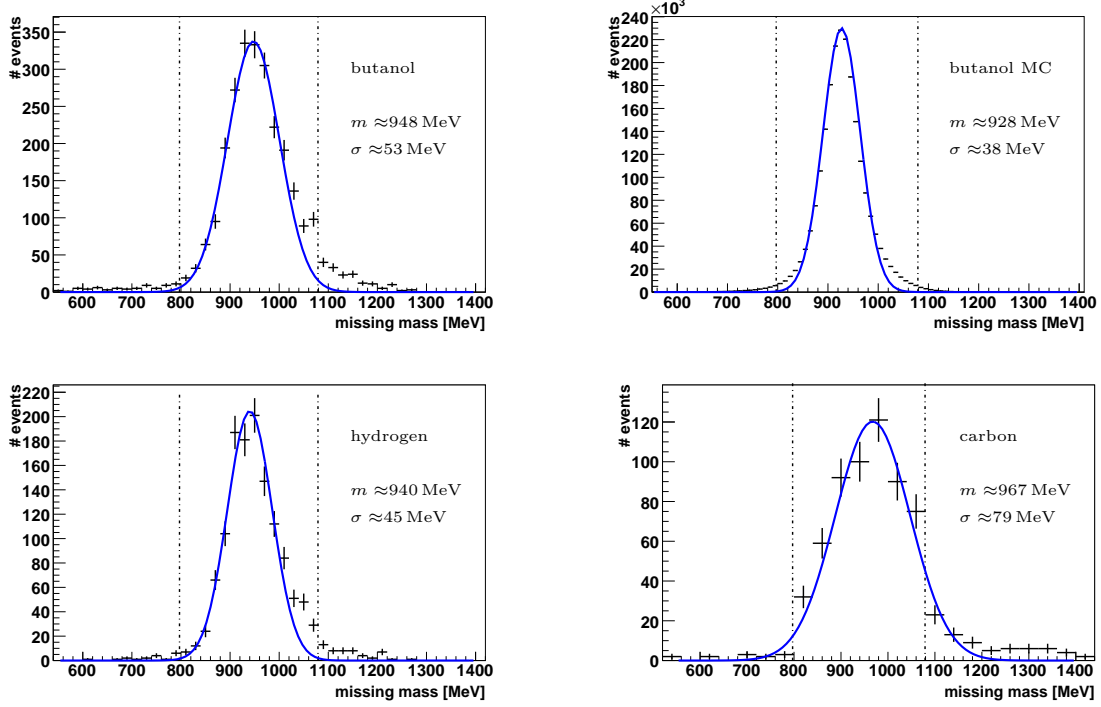


Figure 3.6.: The missing mass spectrum after applying all cuts for the different targets. A Gaussian fit on the hydrogen spectrum is used to determine the 3σ cut boundaries (dashed lines). The mean value and the standard deviation are given for all spectra. On the top right side, the Monte Carlo spectrum for the butanol target is shown.

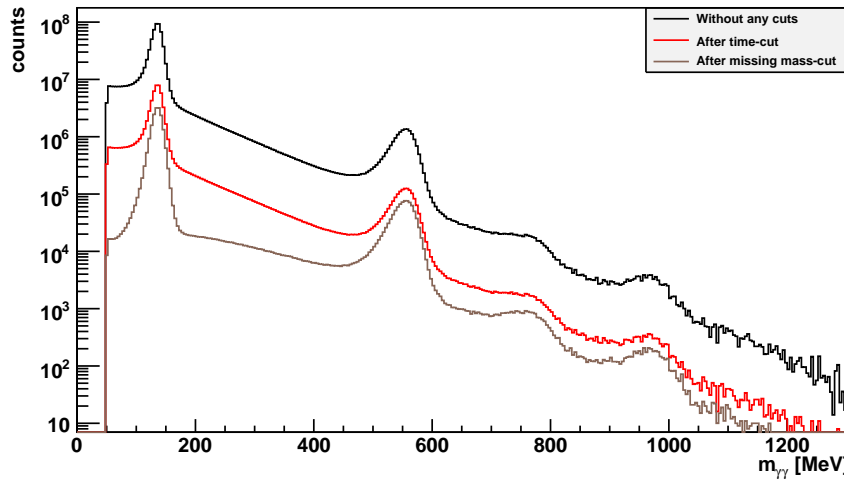


Figure 3.7.: The invariant mass distribution after applying no cuts at all (black), the time-cut (red) and after additionally applying the missing mass cut (brown).

3. Selection of $\gamma p \rightarrow \eta' p$ events

In comparison to the hydrogen target data, the missing mass spectrum is slightly broader for the butanol target and much broader for the carbon target data. The reason for this behavior is the Fermi motion of the bound nucleons in carbon. Thus, one gets an additional Fermi momentum which shifts the missing mass spectrum towards higher masses. The Monte Carlo spectrum for the butanol target for the reaction $\gamma_B p_{in} \rightarrow p_{out} \eta' \rightarrow p_{out} \gamma\gamma$ is slightly thinner than the corresponding data spectrum because the Fermi motion is not considered in the Monte Carlo data.

Figure 3.7 shows the impact of the missing mass-cut on the invariant mass spectrum. The background, especially between the π^0 and η peaks, is reduced a lot as well as the background on the left and right side of the η' peak.

Although the energy of the protons is not available, the angles Φ and θ of the protons are measured and can be used for other cut conditions.

Coplanarity and cut on the θ -difference

In the initial state the beam photon moves in z direction towards the resting target. Thus the x- and y- components of the total initial momentum p_x and p_y are zero. Considering momentum conservation, the total transversal momenta p'_x and p'_y of the final state have to vanish as well. It means that the projected three-momentum vectors of η' and proton in the xy-plane perpendicular to the beam direction have to cancel each other out by lying back to back (see figure 3.8). It is also possible to obtain this condition in the following way:

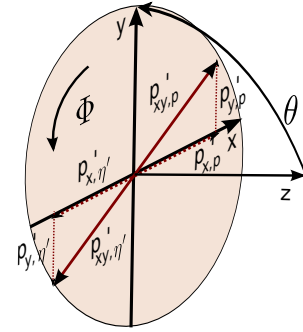


Figure 3.8.: The η' and proton momenta are projected in the xy-plane where the x- and y components of each particle cancel each other out in the lab frame.

$$p'_x = |\vec{p}_{\eta'}| \cos \Phi_{\eta'} \sin \theta_{\eta'} + |\vec{p}_p| \cos \Phi_p \sin \theta_p \stackrel{!}{=} 0 \quad (3.8)$$

$$p'_y = |\vec{p}_{\eta'}| \sin \Phi_{\eta'} \sin \theta_{\eta'} + |\vec{p}_p| \sin \Phi_p \sin \theta_p \stackrel{!}{=} 0. \quad (3.9)$$

Rewriting equation (3.9) to $\sin \theta_{\eta'} = -\frac{|\vec{p}_p| \sin \Phi_p \sin \theta_p}{|\vec{p}_{\eta'}| \sin \Phi_{\eta'}}$ and inserting it in equation (3.8) yields

$$\begin{aligned} -\frac{\cos \Phi_{\eta'}}{\sin \Phi_{\eta'}} |\vec{p}_p| \sin \Phi_p \sin \theta_p &= -|\vec{p}_p| \cos \Phi_p \sin \theta_p \\ \Leftrightarrow \tan \Phi_{\eta'} &= \tan \Phi_p. \end{aligned} \quad (3.10)$$

The condition (3.10) is only fulfilled if $\Delta\Phi = \Phi_p - \Phi_{\eta'} = 180^\circ$ ⁴ holds. This is used to further reduce the background with a 3σ -cut of $-18.3^\circ < (\Delta\Phi - 180^\circ) < 17.7^\circ$ which is obtained again through a Gaussian fit on the hydrogen spectrum. The Φ symmetry of the detector system is mirrored in the Φ distributions (see figure 3.9).

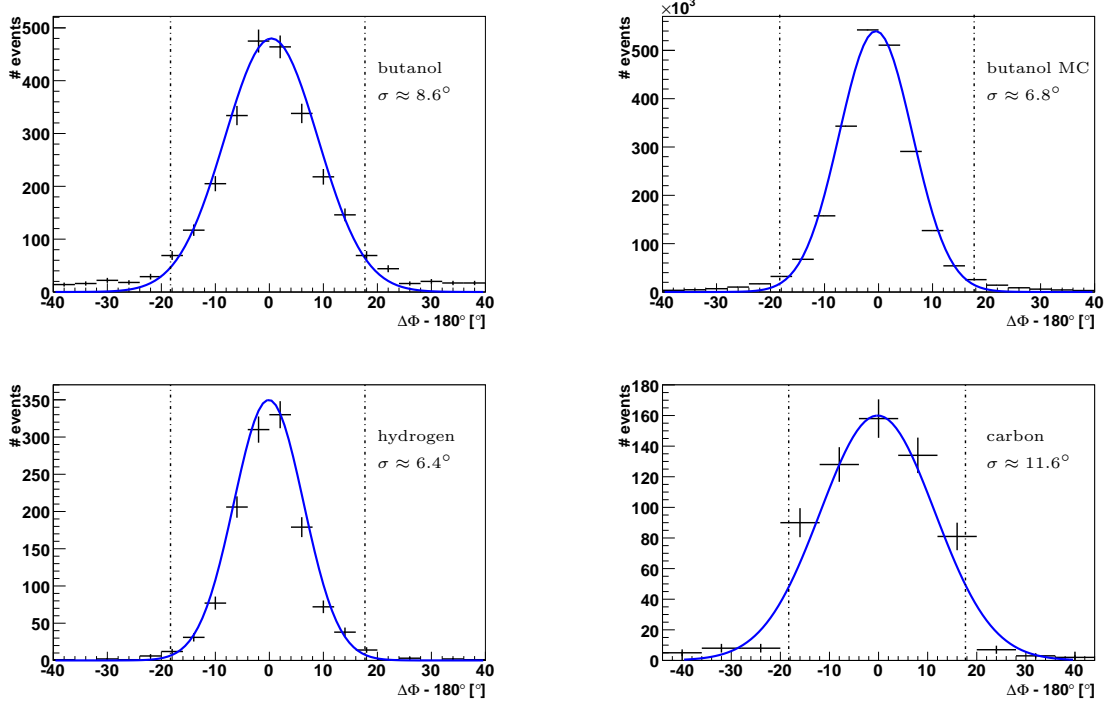


Figure 3.9.: The Φ -difference between proton and η' is shown in the lab system for all target materials and the butanol Monte Carlo data. The dashed lines mark the chosen cut boundaries. Gaussian functions are fitted to the data (blue) and the standard deviations are given as well.

So far, the reaction was discussed only in the lab frame where the target is at rest. Boosting this system to the center of mass system, one finds a condition that the θ angle difference of proton and η' has to fulfill. Since p_x and p_y are zero in the lab frame and the boost direction is in z direction, p_x^* , p_y^* are also zero in the center of mass system. Taking into account that in the center of mass system the total momentum vanishes, it holds $|\vec{p}_p^*| = |\vec{p}_{\eta'}^*|$ and for the z-component of the momenta of η' and proton:

$$\begin{aligned} p_{z,\eta'}^* = -p_{z,p}^* &\Leftrightarrow |p_{\eta'}^*| \cos \theta_{\eta'}^* = -|p_p^*| \cos \theta_p^* \\ &\Leftrightarrow \cos \theta_{\eta'}^* = -\cos \theta_p^*. \end{aligned} \quad (3.11)$$

This is only fulfilled if $\Delta\theta^* = \theta_{\eta'}^* - \theta_p^* = 180^\circ$. Since the proton energy cannot be measured, the center of mass system angle θ_p^* is not accessible. Therefore this condition can not be used for the analysis. Instead, the measured angle of the proton θ_p is compared to the

⁴ $\Delta\Phi$ can also be zero, but this is physically not reasonable since this would result in an enhancement of both proton and η' momenta and not in a cancellation.

3. Selection of $\gamma p \rightarrow \eta' p$ events

angle of the calculated proton θ_{mm} . Ideally, both angles should be the same. Thus a 3σ -cut of $-10.6^\circ < (\theta_{mm} - \theta_p) < +10.4^\circ$ is applied (see figure 3.11).

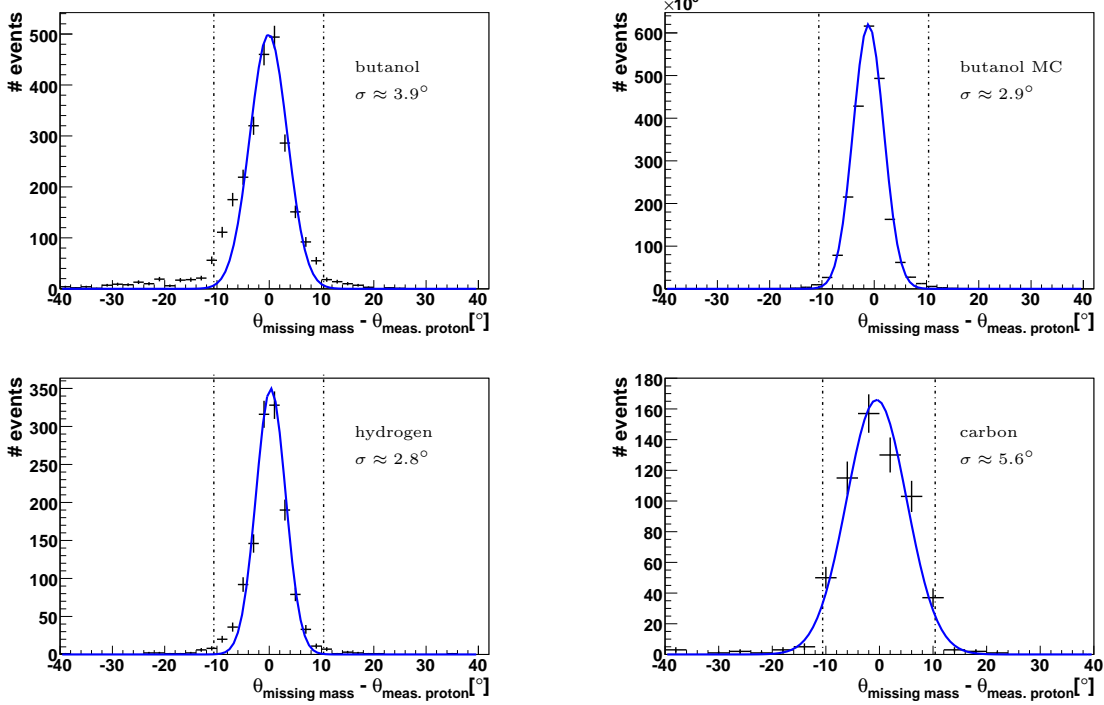


Figure 3.10.: The θ -difference of the calculated and the measured proton is depicted here together with the cut boundaries as dashed lines. The standard deviation of the fit results (blue) are given as well.

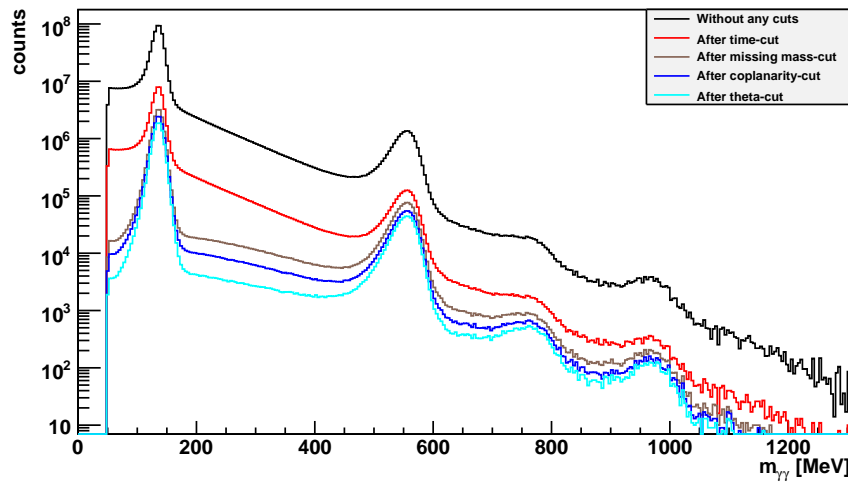


Figure 3.11.: The invariant mass distribution is shown after each of the applied cuts: In red the spectrum after applying the time-cut, in brown the missing-mass cut and in dark and light blue the influence of the coplanarity- and theta-difference-cut, respectively.

Unlike the Φ distributions, the θ distributions are slightly asymmetric due to the asymmetric form of the missing mass spectrum. Figure 3.11 shows the effect of the coplanarity- and θ -difference-cut on invariant mass. Compared to the missing mass-cut and the time-cut not many events are rejected as background events. Since the background is reduced more than the η' peak, the coplanarity- and theta-cuts improve the signal to background ratio.

Energy of the beam photons

The knowledge of the η' four-momentum is used to calculate the beam photon energy corresponding to a reconstructed η' and proton. Quadrating equation (3.6) and using the PDG mass values $m_{\eta'} = 958$ MeV and $m_p = 938$ MeV yields

$$\begin{aligned} m_p^2 &= (E_{\gamma_B} + m_p - E_{\eta'})^2 - (\vec{p}_{\gamma_B} - \vec{p}_{\eta'})^2 \\ m_p^2 &= E_{\gamma_B}^2 + m_p^2 + 2E_{\gamma_B}m_p + E_{\eta'}^2 - 2(E_{\gamma_B} + m_p)E_{\eta'} - \vec{p}_{\gamma_B}^2 - \vec{p}_{\eta'}^2 + 2\vec{p}_{\gamma_B}\vec{p}_{\eta'}. \end{aligned} \quad (3.12)$$

Using $\vec{p}_{\gamma_B}^2 = E_{\gamma_B}^2$, $E_{\eta'}^2 - \vec{p}_{\eta'}^2 = m_{\eta'}^2$ and $2\vec{p}_{\gamma_B}\vec{p}_{\eta'} = 2E_{\gamma_B}|p_z|_{\eta'}$, gives

$$0 = 2E_{\gamma_B}m_p - 2E_{\gamma_B}E_{\eta'} - 2m_pE_{\eta'} + m_{\eta'}^2 + 2E_{\gamma_B}|p_z|_{\eta'}. \quad (3.13)$$

Thus the beam photon energy is calculated by

$$E_{\gamma_B,cal.} = \frac{-0.5 \cdot m_{\eta'}^2 + m_pE_{\eta'}}{(m_p - E_{\eta'} + |p_z|_{\eta'})}. \quad (3.14)$$

A comparison of the calculated and measured beam photon energy helps to choose the beam photons which initiated the reactions involving η' . These events are found distributed around the diagonal, shown in figure 3.12 as a black line. Besides, a lot of events are accumulated below the diagonal which correspond to beam photons that belong to π^0 or/and η photoproduction reactions, because in that case the wrong meson mass, namely $m_{\eta'} (> m_{\pi^0}, m_\eta)$, is subtracted in the nominator of equation (3.14). These events do not exist in the Monte Carlo spectrum belonging to η' .

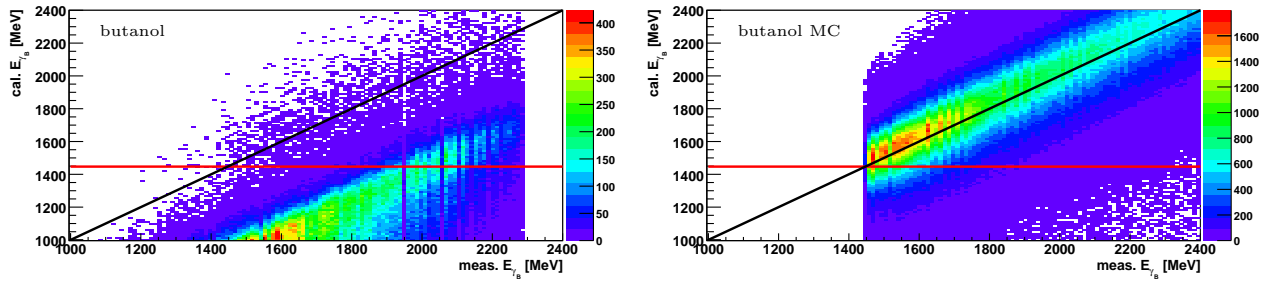


Figure 3.12.: The measured beam photon energy is plotted against the calculated beam photon energy after applying the cuts that were discussed so far. The black line shows the diagonal around which η' events are distributed and the red line marks the applied cut. Underneath the diagonal events belonging to π^0 - and η -reactions are located. These events do not exist in the Monte Carlo data of η' .

Since the production threshold of η' lies at $E_{\gamma_B} = 1447$ MeV, this value is chosen to apply a cut on the calculated beam photon energy (red line in figure 3.12). This removes the majority of events with π^0 , η or ω in the final state from the invariant mass spectrum as it was indicated by the beam photon energy histograms (compare figure 3.13).

After applying the energy-cut additionally to the previously discussed cuts, there remains in average approximately 1.19 beam photons per set of decay particles, which indicates the successful reduction of combinatorial background through all the applied cuts so far.

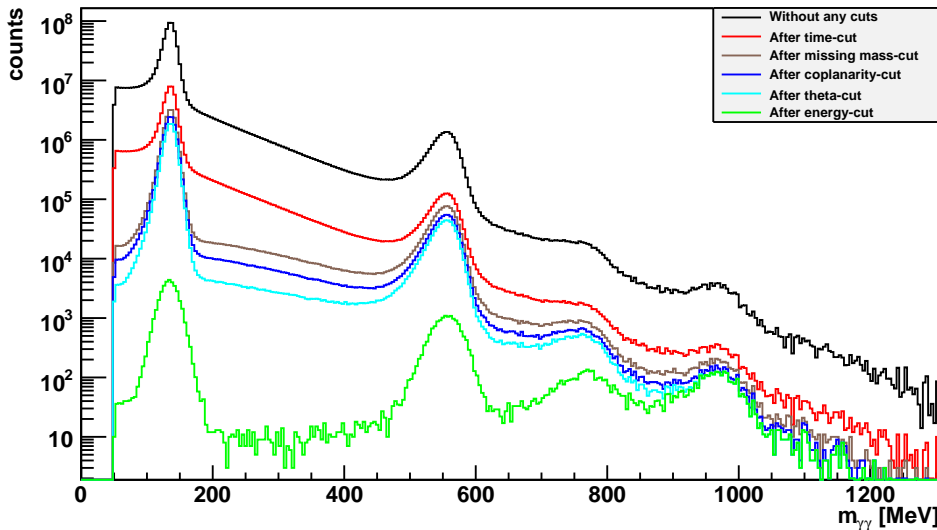


Figure 3.13.: The invariant mass distribution is shown after each of the applied cuts: In red the spectrum after applying the time-cut, in brown the missing mass-cut and in dark and light blue the influence of the coplanarity- and the θ -difference-cut, respectively. Furthermore, in green the invariant mass is depicted after applying the energy-cut.

Invariant mass

After applying all the previously described cuts, a little background together with the π^0 -, η - and ω -peaks remain. Therefore, a last 3σ -cut is applied on the invariant mass of $862 \text{ MeV} < m_{\gamma\gamma} < 1054 \text{ MeV}$. In this range, around 2400 candidates for η' exist and these events are used to calculate the double polarization observable E in chapter 4. The data is fitted with the sum of three Gaussian functions for the η -, ω - and η' -peaks and a polynomial function of second order⁵ to describe the background (see figure 3.14). Within the cut boundaries, approximately 65% of the selected events belong to the η' peak. It seems, there is almost no overlap of the η' - and ω -peak. A comparison with the Monte Carlo data of η' and ω , that are scaled to approximately the same height, also show no indication for a large overlap between the ω - and η' -peak. The remaining background is therefore

⁵Fit results of the polynomial function: $f(x) = -324 + 1.2 \cdot x - 0.0008 \cdot x^2$.

assumed to consist of events involving unpolarized nuclei or incorrect reconstructed events and it needs further investigation in the future.

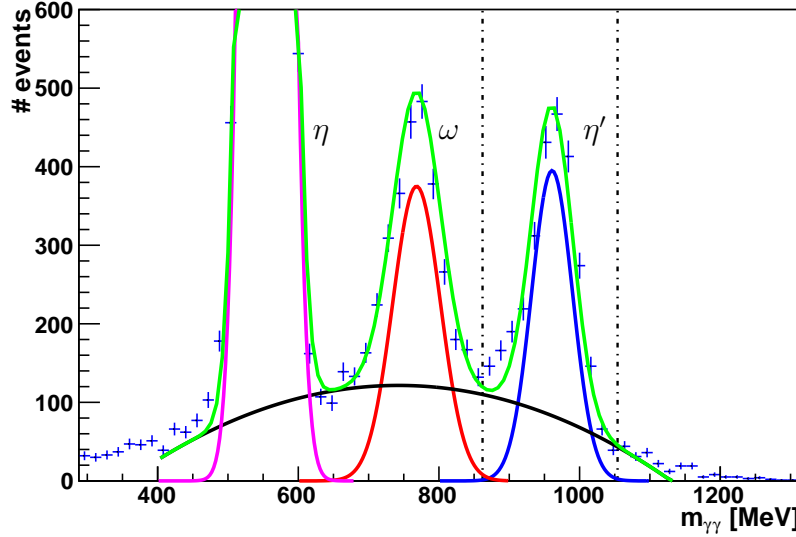


Figure 3.14.: The invariant mass is shown after all cuts (blue points) together with the applied cut boundaries (dashed lines). The η , ω and η' are fitted with Gaussian curves and the background with a polynomial function of second order (black line). The sum of all Gaussian functions together with the polynomial function is plotted in green.

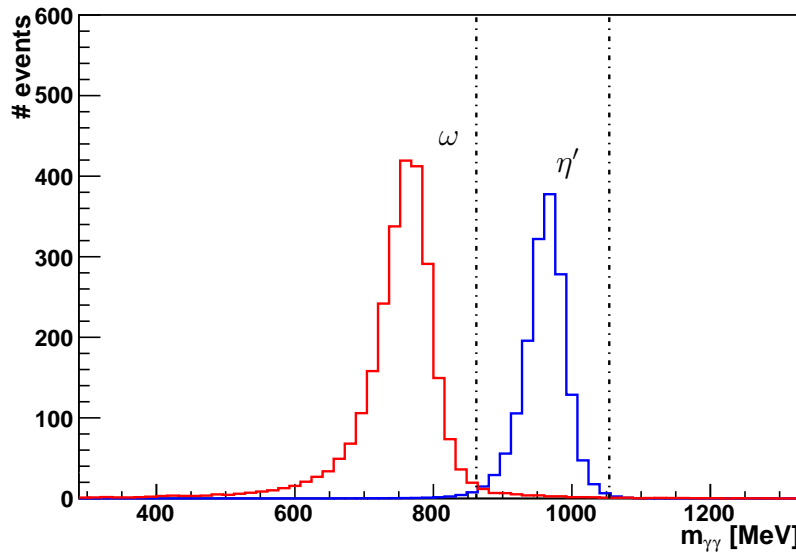


Figure 3.15.: The invariant mass distributions of the η' (blue) and the ω (red) Monte Carlo data after applying all cuts.

3.5. Reconstruction of the decay channel

$$\eta' \rightarrow \pi^0 \pi^0 \eta \rightarrow 6\gamma$$

The analysis of the decay channel $\eta' \rightarrow \pi^0 \pi^0 \eta \rightarrow 6\gamma$ poses a greater challenge than the analysis of the previous analyzed decay mode $\eta' \rightarrow \gamma\gamma$, mainly due to two differences:

- The six decay photons have to be combined pairwise to two π^0 and one η which leads to 45 combinatorial possibilities in total as it is explained in more detail in section 3.5.1.
- There are concurrent photoproduction reactions like $\gamma_B p_{in} \rightarrow \pi^0 \pi^0 \pi^0 p_{out}$ or $\gamma_B p_{in} \rightarrow \pi^0 \pi^0 \eta p_{out}$. Thus, this decay channel is not very clean.

In this thesis, two approaches are presented to effectively reduce all background, namely without and with a kinematic fit.

3.5.1. Combinatorics

The six photons of the final state have to be combined first pairwise to one of the decay mesons before being combined to η' : 15 possibilities exist for combining two out of six photons as a new particle. Thereby, the order of the photons is irrelevant. For each of the 15 pairs of photons, there are six potential ways to combine two out of the four remaining photons to a second particle. This leaves only one possibility for the last pair of photons to build a third particle.

In total there are

$$N_{combinations} = \binom{6}{2} \cdot \binom{4}{2} \cdot \binom{2}{2} = 15 \cdot 6 \cdot 1 = 90 \quad (3.15)$$

possibilities to build $\pi^0 \pi^0 \eta$ from six photons. But since the two π^0 are indistinguishable particles and lead to the same η' particle, there are 45 distinct ways per event to combine all six photons to different η' .

Additionally, there is more combinatorial background due to the up to 15 possible beam photons in the initial state that can be assigned to the same six photons in the final state. Thus, there are at most $45 \cdot 15 = 675$ possibilities for the same event. Normally, each of these possibilities has to be investigated individually in order to find the right combination for a certain event.

In order to avoid a time intensive analysis, the number of possibilities is reduced from the very beginning. Therefore, not all of the 15 possibilities for the first pair of photons are taken into account but only those whose mass corresponds to the η mass in the range of $488 \text{ MeV} < m_{\gamma\gamma} < 608 \text{ MeV}$ ⁶. The invariant mass of the first pair of photons is depicted

⁶It does not matter if the η particle is selected first or one of the π^0 because the order of the particles does not change the resulting η' particle.

as the black curve in figure 3.16. The π^0 -peak is clearly visible whereas the η -peak is barely. Besides, a large background is visible due to falsely combined photons. For those pairs that survived the η cut, the six possibilities for the second pair of photons is shown as the red curve in figure 3.16. The η -peak is not visible anymore and the number of events has dropped significantly since concurrent reactions with $3\pi^0$ in the final state are mostly suppressed. A 3σ -cut on the invariant mass $m_{\gamma\gamma}$ is applied with $104 \text{ MeV} < m_{\gamma\gamma} < 164 \text{ MeV}$ in order to find the best suited combinations for a π^0 . The invariant mass of the third pair of photons is shown as the blue curve. Again, the same cut is applied to choose only the sets of six photons with the last pair of photons corresponding to a π^0 . The boundaries for the cuts on the meson masses are ascertained by fitting a Gaussian curve to the π^0 - and η -peaks in the invariant mass spectrum of the previously analyzed decay channel $\eta' \rightarrow \gamma\gamma$. Thus it is made sure that the applied 3σ -cuts do not reject more events than necessary.

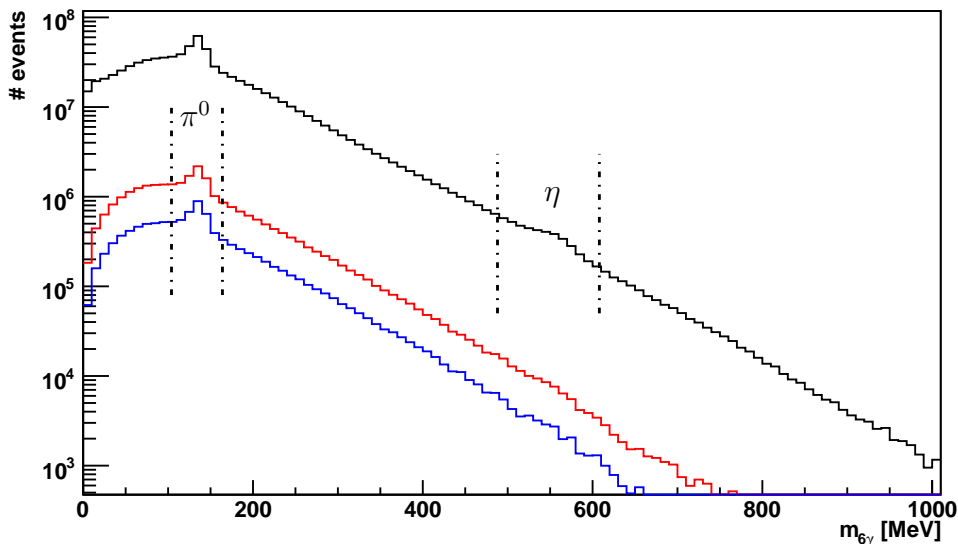


Figure 3.16.: All 15 combinations for the invariant mass of the first pair of photons is shown in black. After the pairs with their masses being near the η -mass are selected, all six combinations for the remaining four photons are plotted as the red curve. Now a π^0 is selected with a cut on the $m_{\gamma\gamma}$. The combinations are reduced once more by demanding the third meson to be a π^0 as well (blue curve).

3.5.2. Selection without a kinematic fit

Once the most suitable candidates of six photons belonging to η' are chosen, the η' four-momentum and thus the invariant mass of the six photons is calculated similar to $m_{\gamma\gamma}$ in

3. Selection of $\gamma p \rightarrow \eta' p$ events

section 3.4:

$$m_{6\gamma} = \left(\sum_{i=1}^6 p_{\gamma_i} \right)^2. \quad (3.16)$$

The same cut conditions as described in section 3.4, that is the time-, missing mass-, coplanarity- and θ -difference-conditions have to be fulfilled here as well. An overview of the applied cut boundaries is given in table 3.3.

cut	cut boundaries
time	$-16 \text{ ns} < t_{reaction} < 5 \text{ ns}$
missing mass	$838 \text{ MeV} < m_{missing} < 1078 \text{ MeV}$
coplanarity	$-20.4^\circ < (\Delta\Phi - 180^\circ) < 18.6^\circ$
θ -difference	$-11.3^\circ < (\theta_{mm} - \theta_p) < 11.3^\circ$
energy	$E_{\gamma_B,cal.} > 1447 \text{ MeV}$

Table 3.3.: An overview of the used cut boundaries.

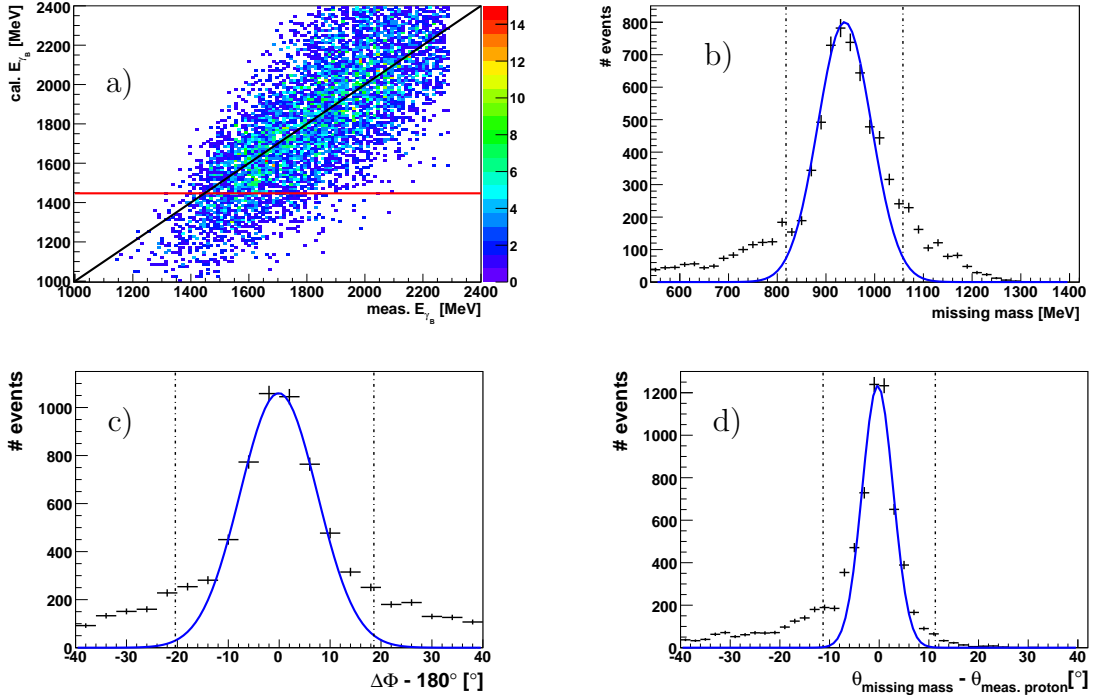


Figure 3.17.: Figure a) shows the calculated energy of the beam photons plotted against the measured beam photon energy. The black line marks the diagonal and the red line, the cut on the calculated energy. From b)-d) the missing mass, the $\Delta\Phi$ - and the θ -difference spectra are depicted together with their cut boundaries (dashed lines). All distributions are shown after applying the cuts listed in table 3.3 and after applying a $3\pi^0$ -anticut (see next section).

Figure 3.17 shows the calculated beam photon energy in dependency of the measured energy a), the missing mass spectrum b), the $\Delta\Phi$ distribution c) and the θ -difference

distribution d) after all cuts listed in table 3.3 are applied (including $3\pi^0$ -anticut which is explained in the following section). In general, more background exists in these spectra compared to those belonging to the decay channel $\eta' \rightarrow \gamma\gamma$ due to the larger combinatorial background. Since the $t_{reaction}$ spectrum looks similar to the one of the decay mode $\eta' \rightarrow \gamma\gamma$, it is not shown here.

The influence of the cuts on the invariant mass is depicted in figure 3.18. Not until the coplanarity-cut is applied, the η' -peak can be set apart from the background which is spread around and underneath the η' -peak. The signal to background ratio is improved even more through the θ -difference- and energy-cut.

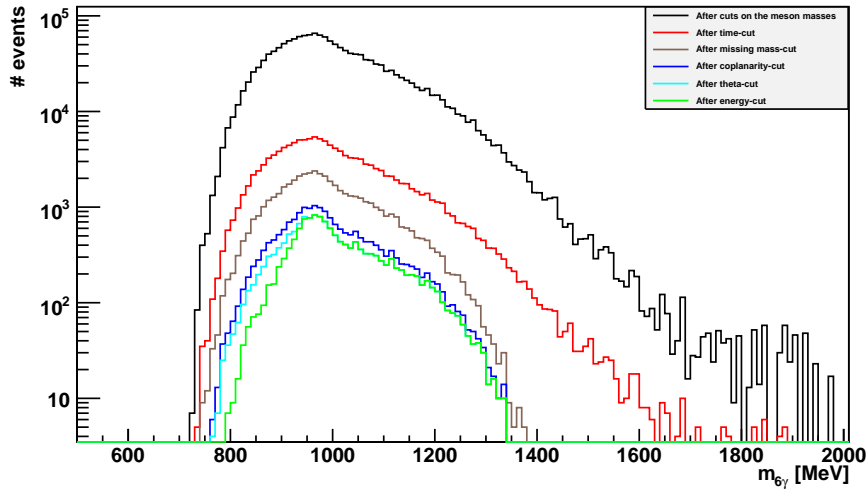


Figure 3.18.: The invariant mass is shown after each of the applied cuts, listed in table 3.3.

Comparison with $\pi^0\pi^0\pi^0$ in the final state

In order to investigate whether a large amount of the background, which is seen in figure 3.18, originates from $3\pi^0$ events, the six photons of the final state are combined to $3\pi^0$, if possible. In figure 3.19 a)-d), the energy of the reconstructed $3\pi^0$ vector is plotted in dependency of the relativistic parameter $\gamma = E_{3\pi^0}/m_{6\gamma}$. A comparison with the Monte Carlo simulations of direct $3\pi^0$ production ($\gamma_B p_{in} \rightarrow p_{out} 3\pi^0$) and $\gamma_B p_{in} \rightarrow p_{out} \eta \rightarrow p_{out} 3\pi^0$ explains that the distribution of the butanol data consists of both previously mentioned reactions. The $3\pi^0$ belonging to η are distributed around a line with a gradient of m_η as it can be expected considering the formula for γ . In contrast to this, the directly produced $3\pi^0$ have a much broader spectrum.

Sometimes it happens that an event belonging to $\pi^0\pi^0\eta$ is reconstructed as a $3\pi^0$ event. This is possible if the six photons of the final state are combined pairwise in such way that per chance each mass of the three photon pairs corresponds to the π^0 mass within a certain range. The other way around is of course also possible: $3\pi^0$ events can be falsely identified as $\pi^0\pi^0\eta$ events which explains most of the background in the $m_{6\gamma}$ distribution. The generated Monte Carlo events of η' confirm this statement since some of the six

3. Selection of $\gamma p \rightarrow \eta' p$ events

generated, decay photons of η' are falsely combined to $3\pi^0$ and are therefore observed in a histogram that belongs to reconstructed $3\pi^0$ events (compare figure 3.19 b)).

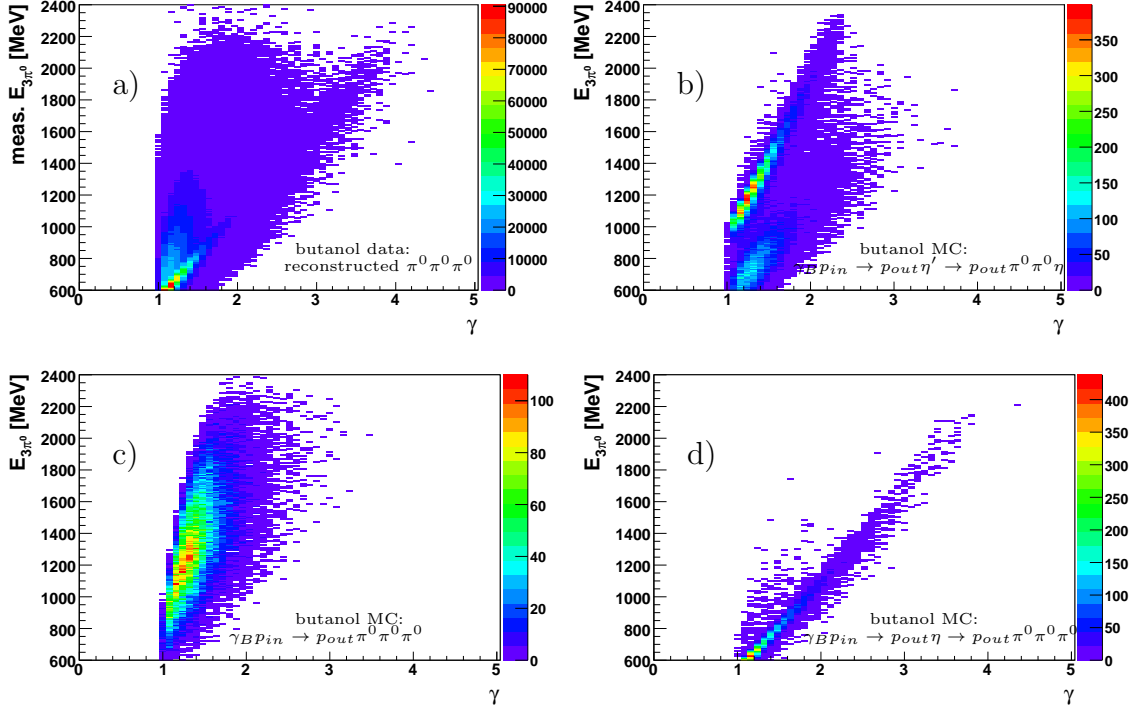


Figure 3.19.: The energy of the reconstructed $3\pi^0$ events is plotted here in dependence of the relativistic $\gamma = E_{3\pi^0}/m_{6\gamma}$. A comparison with different Monte Carlo simulations explains that the data spectrum consists of $\eta \rightarrow 3\pi^0$ and directly produced $3\pi^0$, but also to a small amount of η' events where the six photons are falsely combined to $3\pi^0$ events.

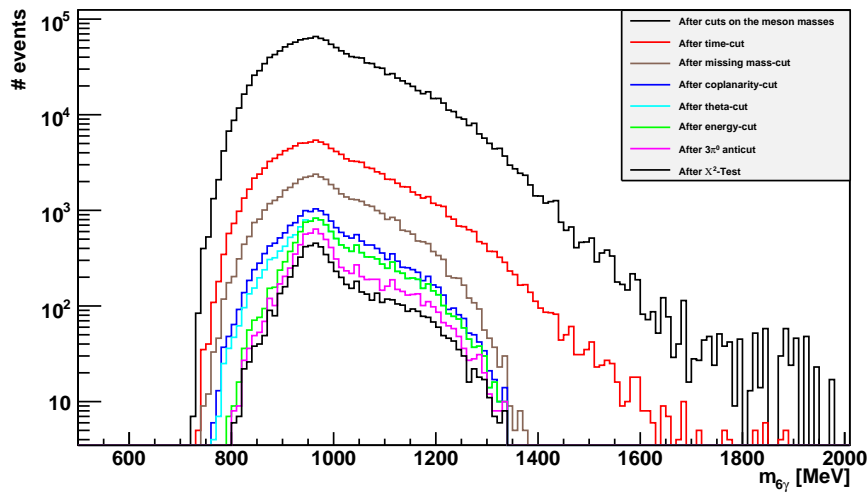


Figure 3.20.: The invariant mass distributions are shown for each of the applied cuts.

In order to reduce the background from $3\pi^0$ events, an anticut is applied by rejecting all the $\pi^0\pi^0\eta$ events that could be reconstructed as a $3\pi^0$ event as well. According to the Monte Carlo simulations, approximately 8% of η' events are rejected falsely in this process. But in exchange 65% of all existing $3\pi^0$ background is suppressed. Thus, the η' -peak is seen more clearly due to this anticut (compare the pink curve in figure 3.20).

The χ^2 -Test

In order to reduce all the remaining combinatorial background, a χ^2 -Test is implemented which ascertains the combination of $\pi^0\pi^0\eta$ where the meson masses are being closest to the PDG mass values. Additionally, the difference of calculated and measured beam photon energy is considered as well:

$$\begin{aligned} \chi^2 = & \frac{(m_{\gamma\gamma}^\eta - m_{\eta,PDG})^2}{\sigma_\eta^2} + \frac{(m_{\gamma\gamma}^{\pi_1^0} - m_{\pi^0,PDG})^2}{\sigma_{\pi^0}^2} + \frac{(m_{\gamma\gamma}^{\pi_2^0} - m_{\pi^0,PDG})^2}{\sigma_{\pi^0}^2} \\ & + \frac{(E_{\gamma_B,cal} - E_{\gamma_B,meas})^2}{\sigma_{E_{\gamma_B}}^2}. \end{aligned} \quad (3.17)$$

The combination with the minimal χ^2 -value is chosen, whereas the σ -values of the meson masses are chosen as explained in section 3.5.1 and $\sigma_{E_{\gamma_B}}$ is estimated as 5 MeV. The invariant mass of the six photons after all cuts is shown in figure 3.21. A clear peak exists around the η' mass which sits on top of a background. The cut on the invariant mass is subsequently chosen in a way that as much as possible background events are rejected: $883 \text{ MeV} < m_{6\gamma} < 1033 \text{ MeV}$. Around 4000 events are chosen thereby. 70% of these events belong to the signal (blue Gaussian curve) and 30% to background events (green Gaussian curve).

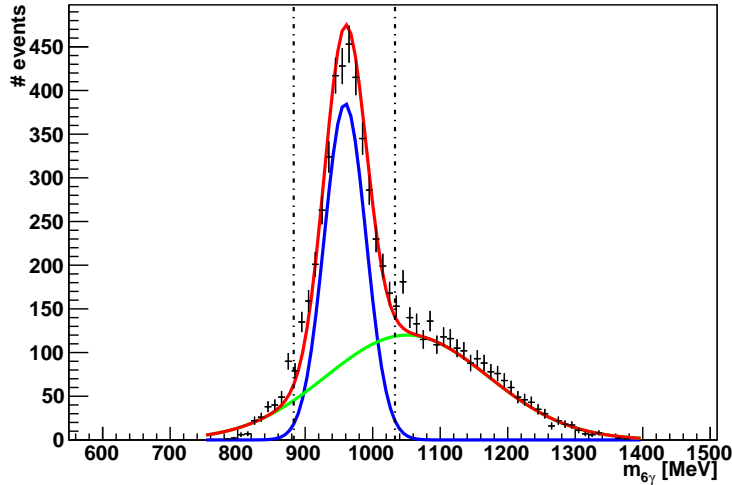


Figure 3.21.: The invariant mass $m_{6\gamma}$ is plotted after all the applied cuts with the cut boundaries as dashed lines. The background and η' -peak are fitted by two Gaussian curves (green and blue). The sum of both Gaussian curves (red) describes the data well.

3.5.3. Selection with a kinematic fit

In order to improve the resolution of the obtained $\eta' \rightarrow \pi^0 \pi^0 \eta$ reaction and thus improve the signal to background ratio, a kinematic fit is applied to the data.

The kinematic fit changes the measured values in such way that energy and momentum are conserved exactly. This is not automatically fulfilled since due to the detector resolutions every measured variable is afflicted with an uncertainty. Furthermore, the best combination is chosen by taking the combination with the highest probability. Thereby, the deviations of the changed measured values from the original values are minimized while considering energy and momentum conservation. Detailed information about the working principle of the kinematic fit can be found in [vP03] and it is briefly explained in the following section.

Basic principle

The energy and the angles θ and Φ are measured for the beam photon and all six photons of the final state. All the measured values can be put in a 21 dimensional vector \vec{y} . Each component y_i , $i = 1, 2, \dots, 21$, has a measurement error σ_i that is estimated using Monte Carlo simulations and considering properties of the electromagnetic shower.

The quantities y_i represent measurements of the true values η_i with ϵ_i being the deviations of both values. It holds

$$\vec{y} = \vec{\eta} + \vec{\epsilon}, \quad (3.18)$$

while ϵ_i follows a normal distribution with an expectation value of zero and a standard deviation σ_i .

The *hypothesis* that is tested (in this case $\gamma p \rightarrow \pi^0 \pi^0 \eta p$) poses in total seven constraints considering energy- and momentum conservation and additionally the masses of the intermediate state particles. The three parameters of the proton (E_p , θ_p and Φ_p) in the final state \vec{x} can be calculated since the number of constraints (seven) is larger than the number of unmeasured values (three). The constraints can be Taylor approximated as linear functions and they can be written as functions of \vec{x} and \vec{y} :

$$f_{1\dots 7}(\vec{x}, \vec{\eta}) = f_{1\dots 7}(\vec{x}, \vec{y} - \vec{\epsilon}) = 0. \quad (3.19)$$

During the kinematic fit, solutions for \vec{x} and \vec{y} are found by varying y_i in such way that the constraints are fulfilled exactly. It is done by minimizing the function

$$M = \vec{\epsilon}^T (C_y)^{-1} \vec{\epsilon} = \sum_{i=0}^{21} \frac{(y_i - \eta_i)^2}{\sigma_i^2} = \sum_{i=0}^{21} \frac{\epsilon_i^2}{\sigma_i^2}. \quad (3.20)$$

The constraints are considered through Lagrange-multiplicators. The matrix C_y represents the covariance matrix of the measured values y_i . If the measurements of the 21 parameters are not correlated, the covariance matrix is a diagonal matrix with the variances of the measured parameters σ_i^2 as entries which is almost always fulfilled. The

values of M should follow a χ^2 -distribution $f(\chi^2)$ with four degrees of freedom (compare figure 3.22). This can be used to evaluate the success/goodness of the kinematic fit. Since the number of degrees of freedom is known together with the minimum $\chi_{min}^2 = M$ value, the probability for a given χ^2 -value to lie above the calculated χ_{min}^2 can be determined:

$$CL = P(\chi^2 > \chi_{min}^2) = \int_{\chi_{min}^2}^{\infty} f(\chi^2) d\chi^2. \quad (3.21)$$

The P value or confidence level (CL) corresponds to e.g. the depicted area in figure 3.22 relative to the entire area underneath the function $f(\chi^2)$. If the errors follow indeed a normal distribution, then the CL-values should follow a uniform distribution with values in the range from zero to one. Those events corresponding truly to the desired reaction do not need to change the measured quantities a lot in order to fulfill all constraints. Therefore, they have low χ_{min}^2 -values and high CL-values. For background reactions however, the χ_{min}^2 values are much higher which result in small CL-values.

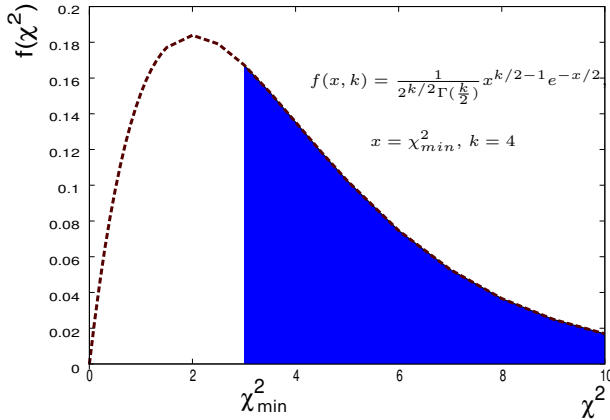


Figure 3.22.: The χ^2 -distribution for four degrees of freedom. The blue area corresponds to the probability that a given χ^2 -value is higher than the calculated χ_{min}^2 -value.

If the hypothesis is true, then all so called pull values

$$pull(y_i) = \frac{y_i - \eta_i}{\sqrt{\sigma^2(y_i) - \sigma^2(\eta_i)}} = \frac{\epsilon_i}{\sigma_i}, \quad i = 1, 2, \dots, 21, \quad (3.22)$$

should follow a standard Gaussian distribution since in average the same amount of values should be increased and decreased by the fit. A shift in the spectrum indicates systematic errors in the measurement that are not considered. Additionally, a deviation of $\sigma = 1$ suggests a wrong estimation of the errors σ_i . A broader spectrum means the errors were assumed too small and a narrower spectrum denotes the opposite. These deviations can be fixed by scaling the errors with factors depending on the detector component (Tagging System, Crystal Barrel, Forward and MiniTaps detector) that performed the measurement. The in total 12 factors are subsequently given as an input to the kinematic fit. In the diploma thesis of P. Nuhn the scaling factors were determined for this particular hypothesis $\gamma p \rightarrow \pi^0\pi^0\eta$ and for data obtained with the hydrogen target [Nuh12]. Since

3. Selection of $\gamma p \rightarrow \eta' p$ events

the goal of the selection process is to choose the events that belong to the polarizable protons of hydrogen atoms in the butanol target, the same scaling factors are taken when applying the kinematic fit to the butanol data.

Application to data

As a first step the missing mass- and coplanarity-cut of $790 \text{ MeV} < m_{missing} < 1090 \text{ MeV}$ and $-20^\circ < \Delta\Phi < +20^\circ$ are applied in order to pass only kinematically relevant events to the kinematic fit. The kinematic fit considers all possible combinations to pair the photons in the final state and takes the combination with the minimal χ^2 -value. Thus, almost all combinatorial background is eliminated by the fit. Only, the different possible beam photons in the initial state remain as combinatorial background. Therefore and to make sure the beam photon belongs indeed to the final state particles, it is important to apply a time-cut of $-20 \text{ ns} < t_{reaction} < 10 \text{ ns}$ additionally to the kinematic fit. Furthermore, the energy-cut is kept in the analysis process as well. Lastly, it is important to investigate the consistency of the proton angles of the fit with the measured ones within 3σ . These cuts are referred to as the θ - and Φ -cut in this section.

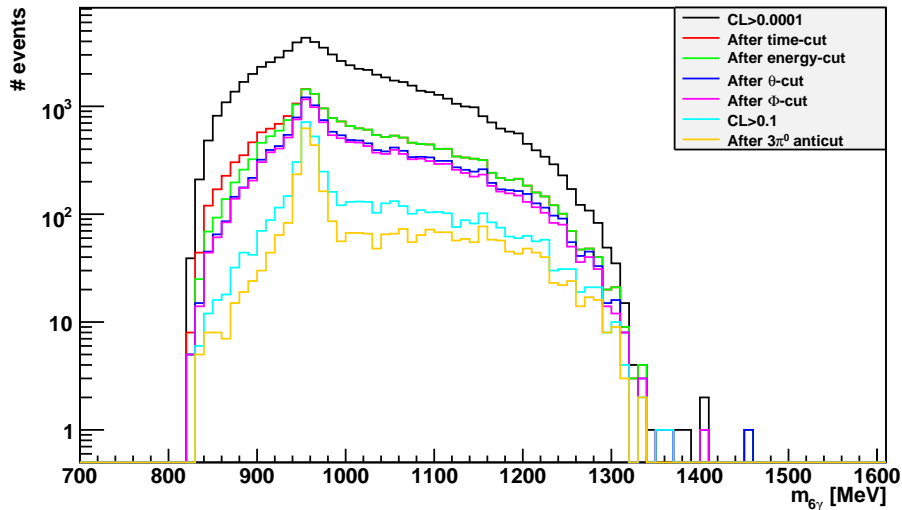


Figure 3.23.: The invariant mass $m_{6\gamma}$ is plotted for all cuts separately.

Figure 3.23 shows the result of the kinematic fit for the invariant mass with $CL > 0.0001$ (black) and the influence of the cuts. After applying the previously described cuts, there still remains a lot of background similar to the histograms without a kinematic fit. This is also mirrored in the pull histograms which do not resemble a Gaussian distribution and are much broader than the Monte Carlo pull histograms. An example is given in figure 3.24a)

for Φ_γ that was measured with the Crystal Barrel⁷. In order to suppress more background, a cut on the CL of $CL > 0.10$ is used since the background reactions accumulate at small CL-values. Now, the η' -peak sets itself clearly apart from the background (turquoise histogram in figure 3.23). Additionally, the data is also kinematically fitted with the hypothesis $\gamma p \rightarrow \pi^0\pi^0\pi^0$. A $3\pi^0$ -anticut is applied by rejecting all events that have a higher CL than 0.1 for this hypothesis. The signal to background ratio improves even more thereafter (orange histogram in figure 3.23). This is also confirmed by the pull histogram in figure 3.24 b) that agrees well the Monte Carlo data after both cuts on the confidence level. Judging from the Monte Carlo data, approximately 82% of the existing $3\pi^0$ -background is eliminated due to this anticut.

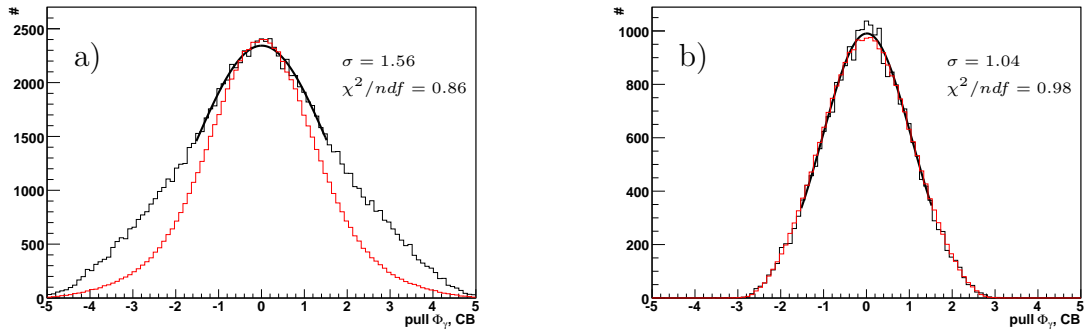


Figure 3.24.: The pull distribution for the angle Φ of the photons that are measured with the Crystal Barrel and in black a Gaussian fit for a range of ± 2 . The scaled Monte Carlo histogram is shown in red (for comparison reasons). Figure a) shows the pull distribution with a cut of $CL > 0.0001$ and in b) after applying a cut of $CL > 0.1$ in combination with the anticut.

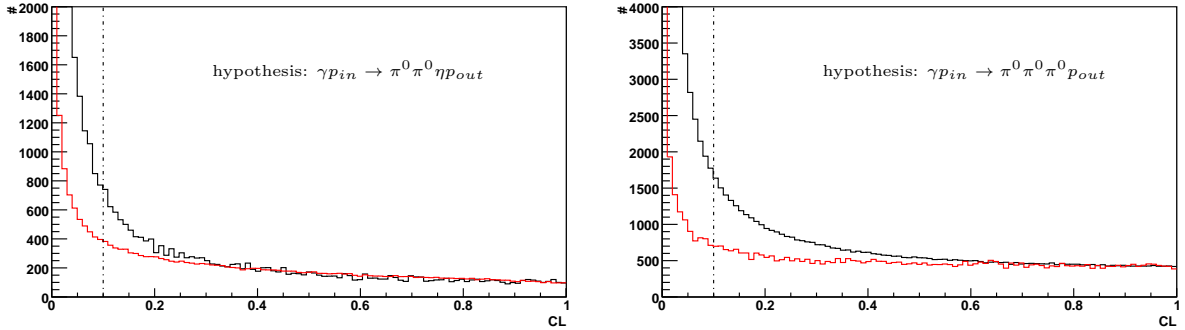


Figure 3.25.: The confidence level distributions for both hypotheses are shown here. In red the corresponding Monte Carlo distributions are depicted. The data indicates a much higher slope towards small CL-values due to the background reactions. It also shows that with the cut on the confidence level (dashed line) not only background events are rejected.

⁷The 21 pull distributions are merged to 12 pull distributions depending on the detector the quantity is measured (Tagging system, Crystal Barrel, Forward and MiniTaps detector). Respectively, three pull distributions for the energy and the angles belong to the same detector. All 12 distributions can be found in A.3. Since the errors of \sqrt{E} follow rather a normal distribution than E , the coordinate system of choice is (\sqrt{E}, θ, Φ) for the kinematic fit.

3. Selection of $\gamma p \rightarrow \eta' p$ events

Finally, the invariant mass-cut is applied (compare figure 3.26). Since the η' -peak is much narrower after the kinematic fit in comparison to the one without a kinematic fit, events within a range of $928 \text{ MeV} < m_{6\gamma} < 988 \text{ MeV}$ are selected. The entire spectrum can be described by two overlapping Gaussian functions. While the blue one describes the η' -peak, the much broader green curve describes the remaining background. Approximately, 1700 events are chosen within the cut boundaries with 87% signal and 13% background contamination. Thus, the application of the kinematic fit improves immensely the signal to background ratio. A comparison with the hydrogen data indicates that the kinematic fit works as well for the butanol data.

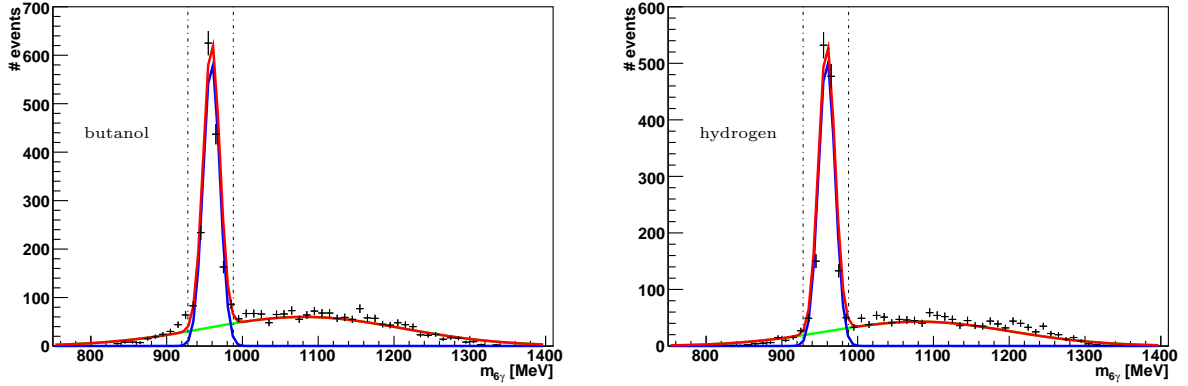


Figure 3.26.: The invariant mass $m_{6\gamma}$ for both butanol and hydrogen data. The η' -peak and the background are fitted by two Gaussian functions (blue and green). The overlap of those (red) agrees well with the data.

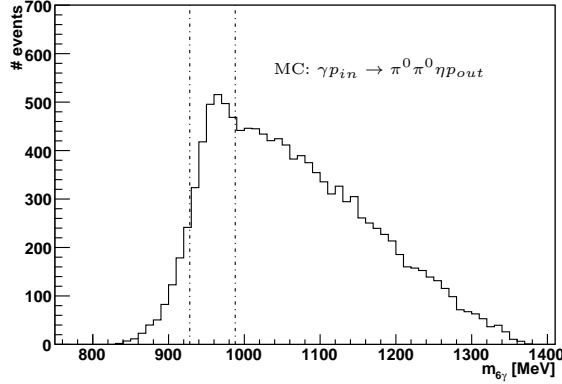


Figure 3.27.: The invariant mass distribution for the photoproduction reaction $\gamma p_{in} \rightarrow \pi^0 \pi^0 \eta p_{out}$ that could contribute to the background underneath the η' -peak.

There are two background reactions that contribute most probably to the remaining background underneath the η' -peak. The first reaction is as already mentioned $\gamma p_{in} \rightarrow \pi^0 \pi^0 \pi^0 p_{out}$. Judging from the Monte Carlo data, its influence should be very small after

the anticut. But there is also the photoproduction reaction $\gamma p_{in} \rightarrow \pi^0\pi^0\eta p_{out}$ whose invariant mass is shown in figure 3.27. Since this reaction contains the exact same final state particles ($\pi^0\pi^0\eta$) as in the desired η' decay mode $\eta' \rightarrow \pi^0\pi^0\eta$, these events fulfill all cut conditions. From the Monte Carlo data it seems therefore, there could be more background underneath the η' -peak than expected from the Gaussian fits to the data. Since the cross sections for both reactions in this energy range are unknown, it is difficult to estimate the exact amount of the background.

4. Extraction of the double polarization observable E

In this chapter, three different methods are described for the determination of the double polarization observable E for the previously selected events. Thereby, each step is presented for both η' -decay channels individually. A comparison of the different methods regarding their statistical and systematical errors is given afterwards. Lastly, the results are compared to the existing predictions of the photoproduction of η' .

4.1. The countrate difference $N_{1/2} - N_{3/2}$

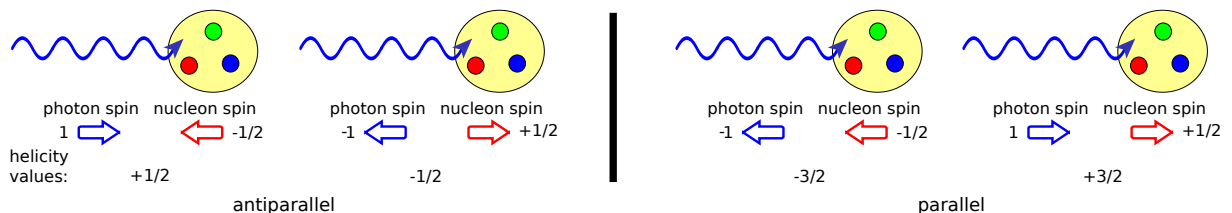


Figure 4.1.: The possible spin configurations of beam photon and target proton. The total spin can be $1/2$ or $3/2$. This leads to four possible helicity values, namely $-3/2$, $-1/2$, $1/2$ and $3/2$.

As mentioned in the introduction, the observable E is a helicity asymmetry, where the helicity is defined as the projection of the spin vector of a particle to its momentum vector. A first information about E can be gained by simply looking at the countrate difference of antiparallel to parallel spin configurations of beam photon and target proton. With the photon having a spin of $s = 1$ and the proton of $s = 1/2$, the total spin is either $1/2$ or $3/2$. There are four possible helicity configurations as depicted in figure 4.1. If the spin is aligned in beam direction, which corresponds to the momentum direction, the sign of the helicity is positive, else negative. In this way, two of the four possibilities belong to an antiparallel, and the other two to a parallel spin configuration.

For the calculation of the countrate difference, the two histograms belonging to antiparallel and parallel spin configurations are added up, respectively. Besides, all butanol beamtimes, that is November 2009 (N09), November 2007 (N07) and September 2009

(S09) are added up as well in order to increase the statistics:

$$N_B^{1/2} = N^{\uparrow\downarrow} + N^{\downarrow\uparrow} = N_{N09}^{\uparrow\downarrow} + N_{N09}^{\downarrow\uparrow} + N_{N07}^{\uparrow\downarrow} + N_{N07}^{\downarrow\uparrow} + N_{S09}^{\uparrow\downarrow} + N_{S09}^{\downarrow\uparrow} \quad (4.1)$$

$$N_B^{3/2} = N^{\uparrow\uparrow} + N^{\downarrow\downarrow} = N_{N09}^{\uparrow\uparrow} + N_{N09}^{\downarrow\downarrow} + N_{N07}^{\uparrow\uparrow} + N_{N07}^{\downarrow\downarrow} + N_{S09}^{\uparrow\uparrow} + N_{S09}^{\downarrow\downarrow} \quad (4.2)$$

The countrate difference $N_B^{1/2} - N_B^{3/2}$ of the invariant mass spectrum is shown in figure 4.2 for both analyzed decay channels of η' . In both histograms, a positive peak is visible around the η' mass which indicates an overall dominance role of spin 1/2 resonances in the photoproduction of η' . Simultaneously, the resemblance of both histograms in the range of the η' mass speaks in favor of a good selection process.

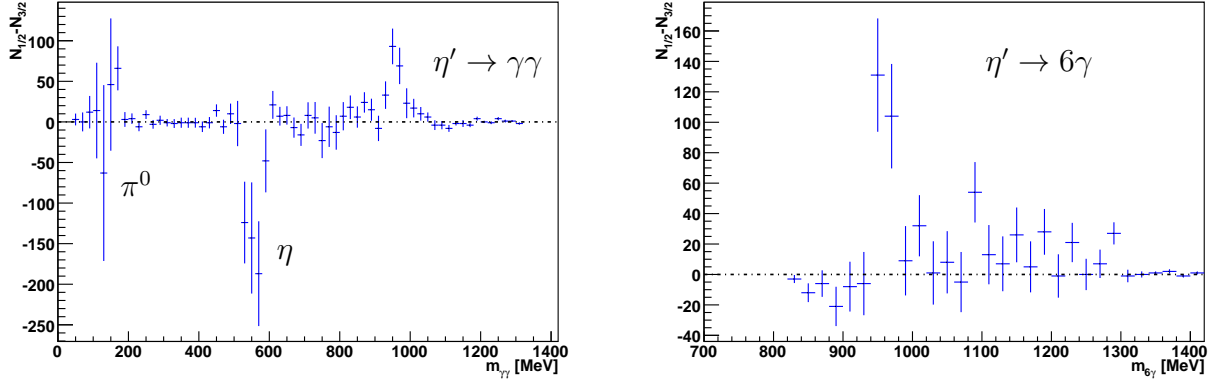


Figure 4.2.: The countrate difference of the invariant mass spectrum for both decay channels. The zero crossing is indicated by the dashed lines. For both decay channels a clear positive peak is visible.

As a next step, the countrate difference's dependency on the beam photon energy is investigated. Figure 4.3 shows the development of the beam photon energy for both spin 1/2- and 3/2-configurations in black and red, respectively. The resulting countrate difference can be seen in figure 4.4. Due to the very low statistics and thus low countrate difference the statistical error bars are very large. The countrate difference spectrum for the $\eta' \rightarrow \gamma\gamma$ decay channel indicates strong spin 1/2-resonance contributions at $E_{\gamma_B} = 1700$ MeV and at $E_{\gamma_B} = 2000$ MeV.

The countrate difference histogram of the $\eta' \rightarrow 6\gamma$ decay channel shows a positive sign for the entire beam photon energy range as well: Almost every point of the $N_{3/2}$ -histogram lies below the $N_{1/2}$ -histogram and is thus consistent with the $\eta' \rightarrow \gamma\gamma$ results. But, especially for higher beam photon energies, the countrate difference for $\eta' \rightarrow 6\gamma$ differs a lot from $\eta' \rightarrow \gamma\gamma$. A possible explanation for this lies in the probable polarized background contribution for $\eta' \rightarrow 6\gamma$ (compare section 3.5.3). It seems, the contributions from polarized background events are not negligible small. Therefore, it does not seem prudent to continue the determination of E with this decay channel. The results for the observable E for $\eta' \rightarrow 6\gamma$ is given nevertheless in figure A.6.

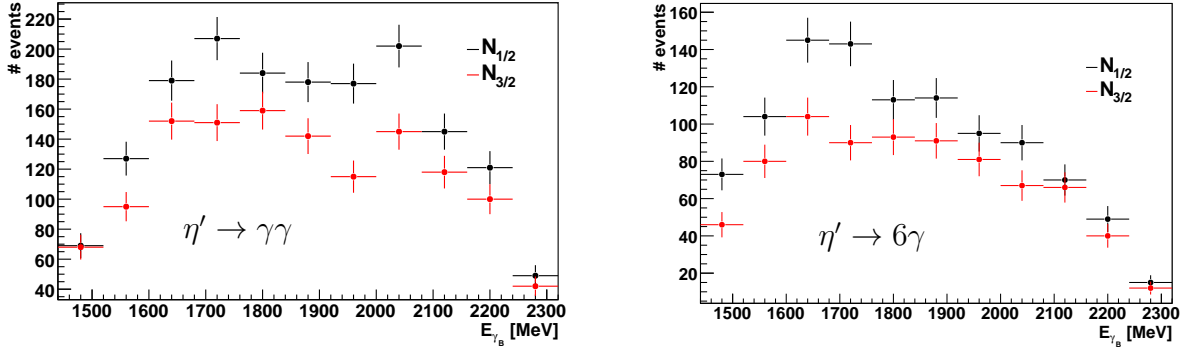


Figure 4.3.: The beam photon energy distributions for antiparallel (black) and parallel (red) spin configuration. The distributions of both decay channels are compared.

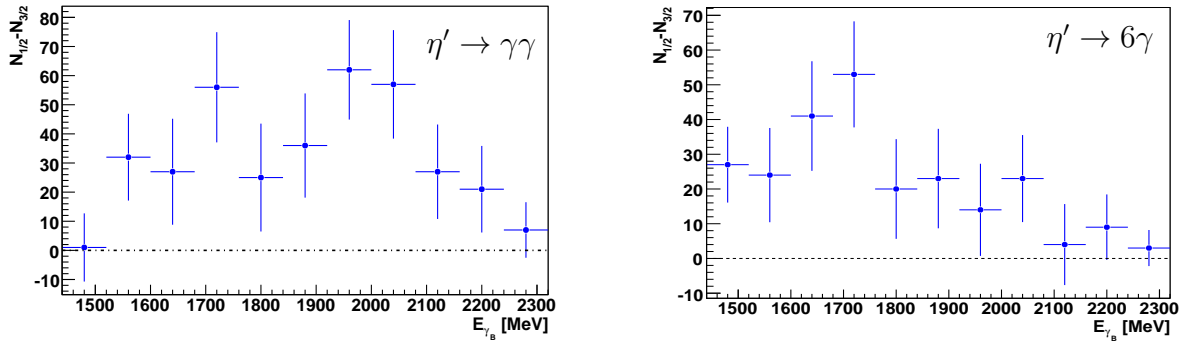


Figure 4.4.: The dependency of the countrate difference on the beam photon energy for both decay channels is depicted. The countrate difference has an overall positive sign for both decay channels.

Aside from the beam photon energy, the observable E also depends on $\cos \theta_{\eta'}$. Therefore the countrate difference is also plotted in dependency of $\cos \theta_{\eta'}$ in the center of mass system (CMS) for four different energy bins (compare figure 4.5). Whereas figures 4.2 and 4.4 suggest an overall spin 1/2-resonances dominance, the $\cos \theta$ -plots show that sometimes also spin 3/2 resonances could play a role. E.g. when the sign of the countrate gets negative or if the countrate difference results in zero, it could indicate contributions of spin 3/2 resonances. Another possible explanation for a countrate difference of zero is the existence of non-resonant background at the corresponding beam photon energy and angle $\cos \theta_{\eta'}$.

4. Extraction of the double polarization observable E

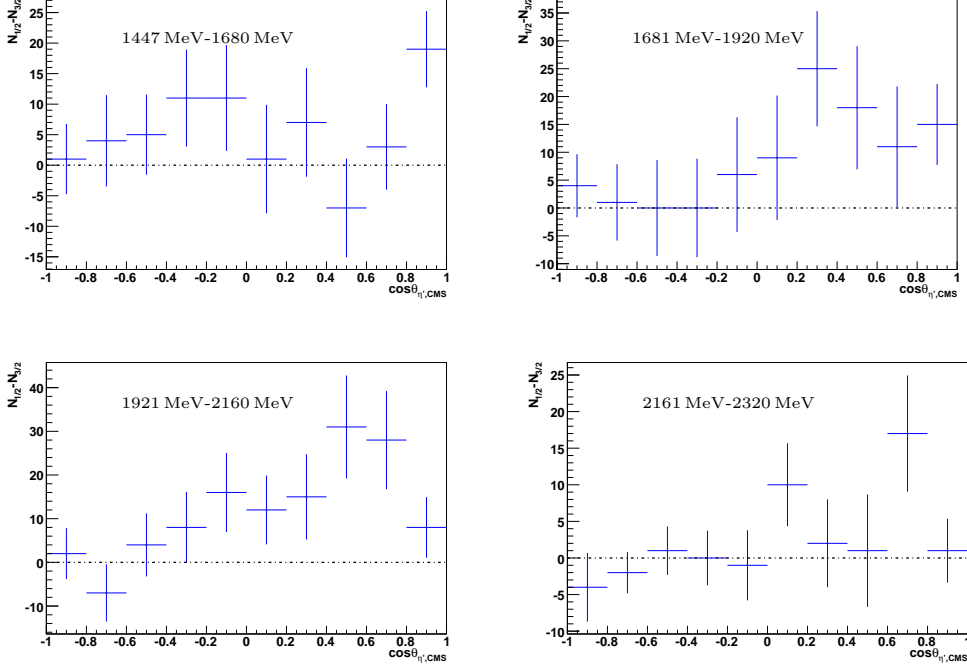


Figure 4.5.: The countrate difference in dependency of $\cos \theta_{\eta',\text{CMS}}$ for four energy bins.

For the exact ascertainment of the observable E , three different methods are applied. For all methods the polarization factor $1/(p_\gamma p_T)$ is needed (see figure 4.6). Whereas the beam photon polarization p_γ depends on the beam photon energy as already explained in section 2.2, the target polarization p_T is in average given by 70 % for all energies.

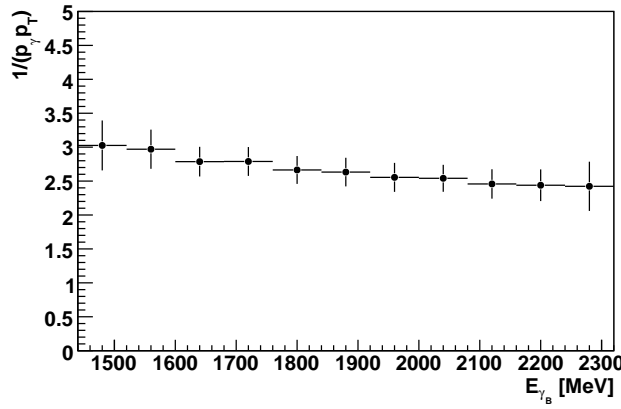


Figure 4.6.: The energy dependence of the polarization factor.

In order to ascertain the energy dependency of $1/(p_\gamma p_T)$, the beam photon energy histogram is scaled with the polarization factor and divided by the unweighted histogram.

The subsequently calculated error bars mirror the statistical uncertainties of the beam photon energy histogram but they do not correspond to the uncertainties of the polarization factor. Therefore, the polarization factor is taken without any error and the uncertainties are taken into account when looking at the systematic errors.

4.2. Determination of E using the dilution factor

The spin dependent differential cross sections of the antiparallel and parallel spin configurations for the butanol target can be split into a polarization dependent hydrogen part and a polarization independent carbon¹ part since only the hydrogen nuclei are polarized in the butanol target:

$$\frac{d\sigma}{d\Omega_B}^{1/2} = \frac{d\sigma}{d\Omega_H} \cdot [1 + p_T p_\gamma \cdot E] + \frac{d\sigma}{d\Omega_C} \quad (4.3)$$

$$\frac{d\sigma}{d\Omega_B}^{3/2} = \frac{d\sigma}{d\Omega_H} \cdot [1 - p_T p_\gamma \cdot E] + \frac{d\sigma}{d\Omega_C}. \quad (4.4)$$

The addition and subtraction of equations 4.3 and 4.4 lead to:

$$\frac{d\sigma}{d\Omega_B}^{1/2} - \frac{d\sigma}{d\Omega_B}^{3/2} = \frac{d\sigma}{d\Omega_H} \cdot 2p_T p_\gamma \cdot E \quad (4.5)$$

$$\frac{d\sigma}{d\Omega_B}^{1/2} + \frac{d\sigma}{d\Omega_B}^{3/2} = 2 \cdot \left(\frac{d\sigma}{d\Omega_H} + \frac{d\sigma}{d\Omega_C} \right). \quad (4.6)$$

Dividing equation (4.5) by equation (4.6), the observable E can be ascertained by

$$E = \frac{\frac{d\sigma}{d\Omega_B}^{1/2} - \frac{d\sigma}{d\Omega_B}^{3/2}}{\frac{d\sigma}{d\Omega_B}^{1/2} + \frac{d\sigma}{d\Omega_B}^{3/2}} \cdot \frac{1}{p_T p_\gamma} \cdot \frac{\left(\frac{d\sigma}{d\Omega_H} + \frac{d\sigma}{d\Omega_C} \right)}{\frac{d\sigma}{d\Omega_H}}. \quad (4.7)$$

The differential cross section is computed in the following way:

$$\frac{d\sigma}{d\Omega} = \frac{N}{A n_\gamma n_T \Gamma \Delta\Omega}, \quad (4.8)$$

whereas N denotes the countrate, A the acceptance of the detection and reconstruction of a generated event, n_γ the photon flux which states the number of photons that initiated a reaction, n_T the target area density, Γ the branching ratio and lastly $\Delta\Omega = 2\pi\Delta \cos\theta$ a certain solid angle element.

Using the definition for the differential cross section and assuming $n_{\gamma,B}^{1/2} \approx n_{\gamma,B}^{3/2}$, equation (4.7) can be simplified as

$$E = \frac{N_B^{1/2} - N_B^{3/2}}{N_B^{1/2} + N_B^{3/2}} \cdot \frac{1}{p_T p_\gamma} \cdot \frac{1}{d}, \quad (4.9)$$

¹Butanol consists of carbon and oxygen atoms aside from hydrogen atoms. Since the photoabsorption cross section is similar for different nuclei [Mac97], the total unpolarized background can be described well with the carbon cross section.

with d being the dilution factor. It specifies the ratio of reactions involving polarizable hydrogen nuclei to all selected reactions for the butanol target. This factor is of great importance due to the non-vanishing carbon part in the sum of spin-1/2 and 3/2 differential cross sections (compare equation (4.6)).

Since except for the dilution factor d all other needed parameters have already been presented, it is explained in the following how the dilution factor is determined.

The dilution factor

Using the formula for the differential cross section, the dilution factor can be rewritten as

$$\begin{aligned} d &= \frac{\frac{d\sigma}{d\Omega} H}{\left(\frac{d\sigma}{d\Omega} H + \frac{d\sigma}{d\Omega} C\right)} = \frac{H \cdot N_H}{H \cdot N_H + C \cdot N_C} = \frac{H \cdot N_H}{B \cdot N_B} = 1 - \frac{C \cdot N_C}{B \cdot N_B} \\ &= s_H \frac{N_H}{N_B} = 1 - s_C \frac{N_C}{N_B}. \end{aligned} \quad (4.10)$$

Here, N_H , N_C and N_B are the countrate histograms obtained with the corresponding target and $H = (A_H n_{\gamma,H} n_{T,H})^{-1}$, $C = (A_C n_{\gamma,C} n_{T,C})^{-1}$ and $B = (A_B n_{\gamma,B} n_{T,B})^{-1}$ characterize the differences of the hydrogen, carbon and butanol targets concerning the acceptance, photon flux and target area density.

In order to determine the scaling factors $s_H = H/B$ and $s_C = C/B$, the countrate histograms for all three targets are required. Adding the scaled hydrogen histogram to the scaled carbon histogram should result in the butanol histogram:

$$s_H \cdot N_H + s_C \cdot N_C = N_B. \quad (4.11)$$

Since the applied cuts on the butanol data are optimized for maximizing the reactions involving hydrogen nuclei, the scaling procedure is applied to e.g. the missing mass spectra after all cut conditions are already fulfilled and can be seen in figures 4.8, 4.9 and 4.11 for π^0 and η' photoproduction. The red colored histograms correspond to the scaled hydrogen histograms and the blue to the carbon histograms. The sum of both is represented by the green histograms and for comparison reasons the butanol missing mass spectra are depicted as well in black. Due to the beam photon energy dependence of the acceptance and the photon flux, the scaling factors have to be determined individually for each energy bin. These 11 energy bins correspond to the eleven points shown in the $N_{1/2}^B$ and $N_{3/2}^B$ histograms in figure 4.3. Hence, each point has a different dilution factor. Unfortunately, the statistics acquired for η' in the final state, especially with the carbon target, is not high enough to allow a precise determination of the scaling factors due to the low number of bins (compare figures 4.11, 4.8 and 4.9). A solution to this problem is the use of the missing mass spectra for the final state $p\pi^0 \rightarrow p\gamma\gamma$ instead of $p\eta' \rightarrow p\gamma\gamma$ in order to get the scaling factors. Thereby, the same cuts are applied to the data except for the invariant mass cut in order to get the missing mass spectra for π^0 . The target area density n_T and the photon flux n_γ do not depend on the meson in the final state. In contrast to this, the acceptance for π^0 and η' differ since the different meson masses lead to different

kinematics. But the scaling factors s_H and s_C do not depend directly on the development of the acceptances A_H and A_C , but on their ratio A_B/A_H or A_B/A_C . Assuming that these ratios behave similar for π^0 and η' , the scaling factors and thus the dilution factors should be almost equal. Whether or not this assumption holds, is investigated by explicitly calculating the acceptances using Monte Carlo data. The determination of the acceptance is discussed in detail in section 4.3. Figure 4.7 shows both ratios A_B/A_H and A_B/A_C for η' and π^0 . Deviations between the ratios for η' and π^0 are visible, whereas the deviations for the A_B/A_C are in average much smaller (up to 4%) than for A_B/A_H (up to 7%). The reason for this are the similarities of the carbon and butanol targets regarding their geometrical dimensions compared to the hydrogen target as mentioned in chapter 2.3.

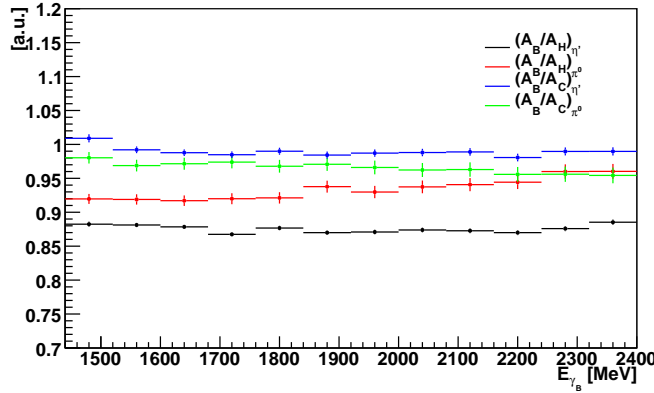


Figure 4.7.: The comparison of the ratios of acceptances for the butanol and the hydrogen target $\left(\frac{A_B}{A_H}\right)$ and for the butanol and carbon target $\left(\frac{A_B}{A_C}\right)$ for π^0 and η' .

The deviations are taken into account by calculating the scaling factors $s_{H,\eta'}$ and $s_{C,\eta'}$ of η' from the obtained π^0 scaling factors s_{H,π^0} and s_{C,π^0} as following:

$$s_{H,\pi^0} = \left(\frac{A_B}{A_H}\right)_{\pi^0} \frac{n_{T,B} n_{\gamma,B}}{n_{T,H} n_{\gamma,H}}, \quad s_{H,\eta'} = \left(\frac{A_B}{A_H}\right)_{\eta'} \frac{n_{T,B} n_{\gamma,B}}{n_{T,H} n_{\gamma,H}}$$

$$\Rightarrow s_{H,\eta'} = s_{H,\pi^0} \cdot \left(\frac{A_B}{A_H}\right)_{\eta'} / \left(\frac{A_B}{A_H}\right)_{\pi^0}. \quad (4.12)$$

$$s_{C,\pi^0} = \left(\frac{A_B}{A_C}\right)_{\pi^0} \frac{n_{T,C} n_{\gamma,B}}{n_{T,C} n_{\gamma,C}}, \quad s_{C,\eta'} = \left(\frac{A_B}{A_C}\right)_{\eta'} \frac{n_{T,B} n_{\gamma,B}}{n_{T,C} n_{\gamma,C}}$$

$$\Rightarrow s_{C,\eta'} = s_{C,\pi^0} \cdot \left(\frac{A_B}{A_C}\right)_{\eta'} / \left(\frac{A_B}{A_C}\right)_{\pi^0}. \quad (4.13)$$

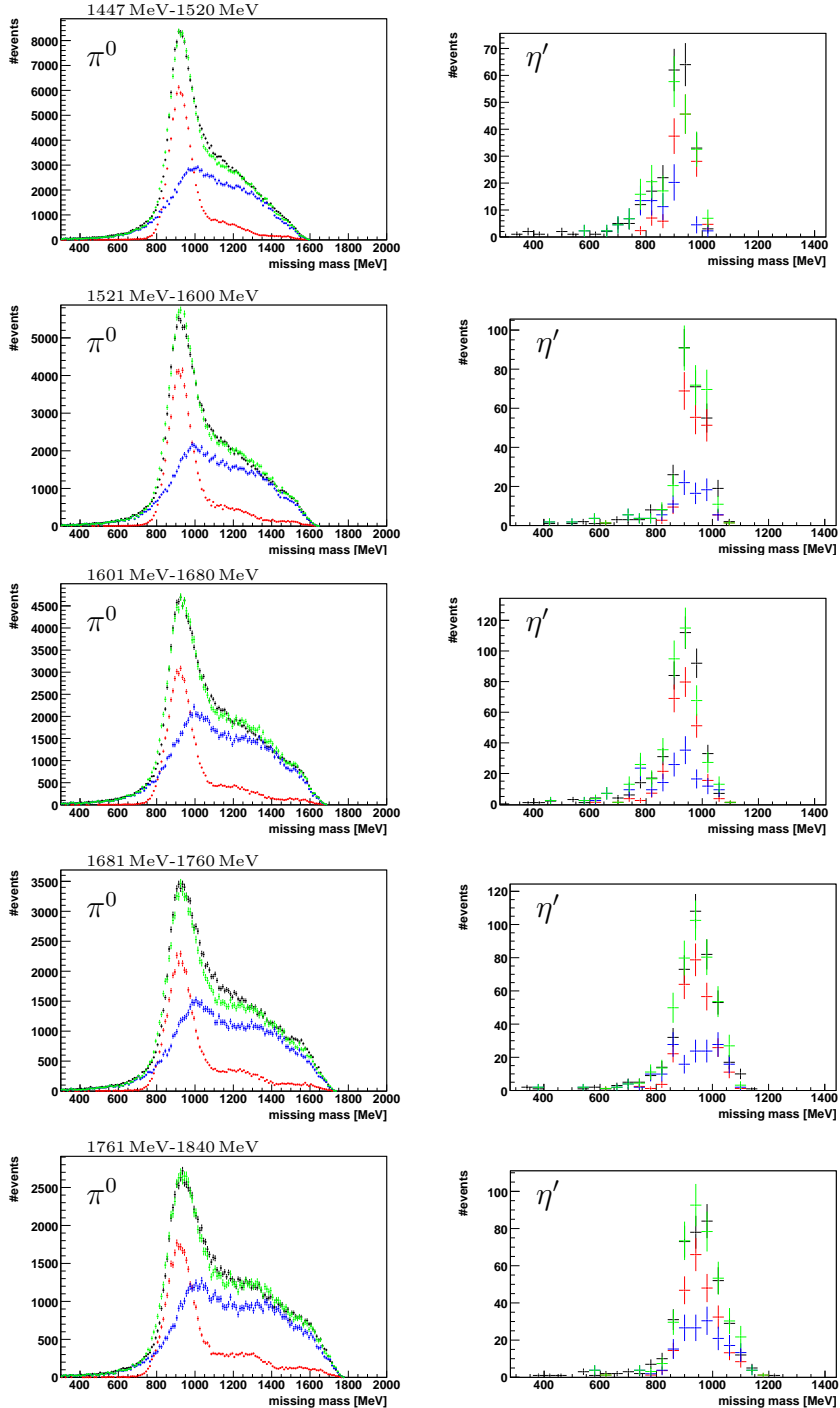


Figure 4.8.: The scaled missing mass spectra for π^0 and η' photoproduction belonging to the hydrogen target (red) and carbon target (blue) are shown together with the butanol missing mass spectrum (black) and the sum of the red and blue histograms (green) for different energy bins.

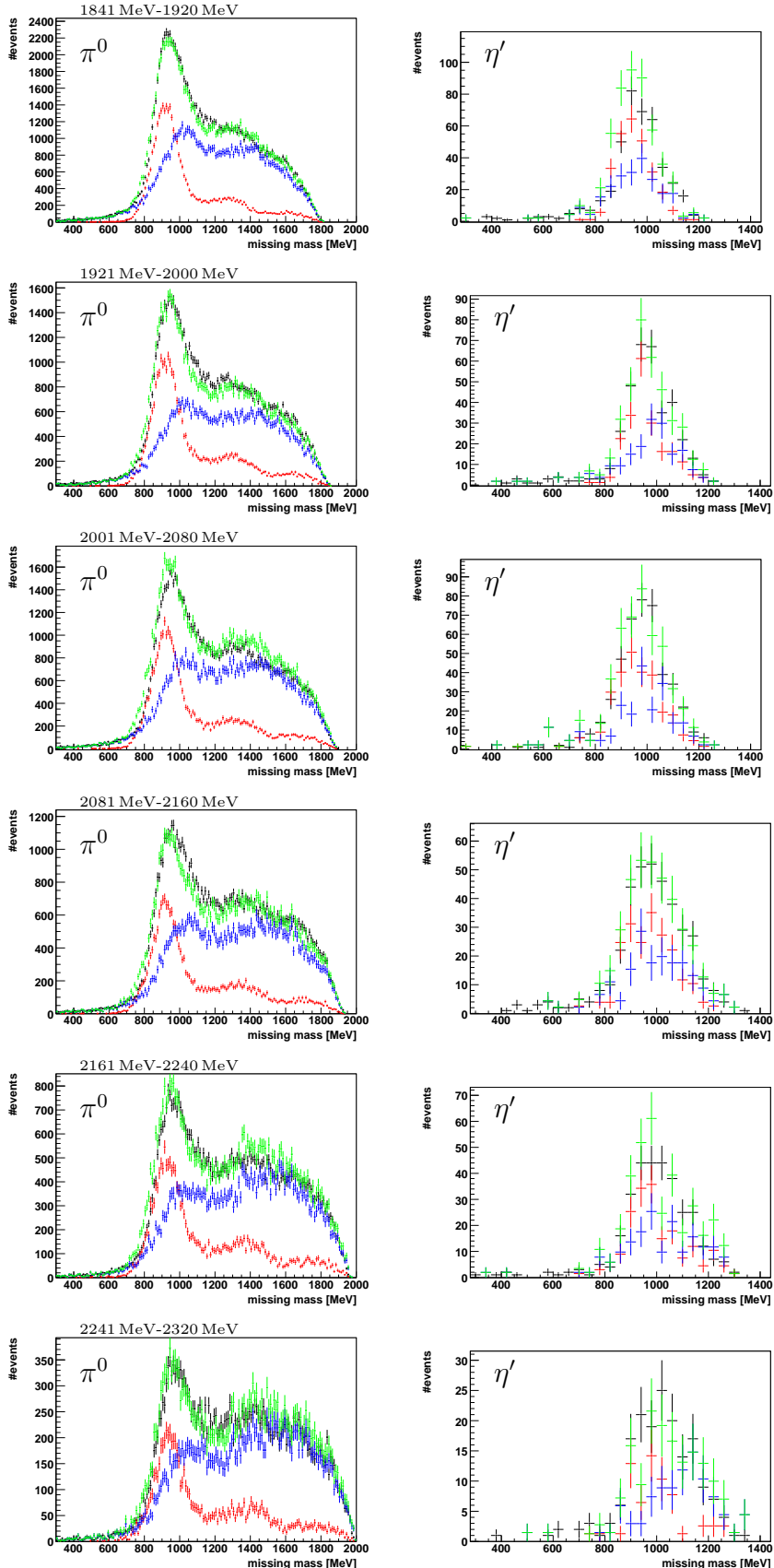


Figure 4.9.: The scaled missing mass spectra for π^0 and η' photoproduction. Colors as is in figure 4.8.

4. Extraction of the double polarization observable E

The obtained scaling factors are then applied to the missing mass spectra of η' . Figures 4.8 and 4.9 demonstrate that the butanol histogram and the sum of the scaled hydrogen and carbon histogram agree well for η' within their error bars.

The ratio of the acceptances as a function of $\cos\theta_{\eta'}$ is controlled for the four energy bins as used in figure 4.5. It is noticeable that the ratios of η' remain almost constant over the entire angular range except for the last bin (see figure 4.10). Therefore and since the photon flux does not have an angular dependence, it is not necessary to determine a scaling factor for each $\cos\theta$ -bin. For the acceptance ratios of π^0 , more fluctuations are visible, especially in the angular range of $0.4 < \cos\theta < 1$. These fluctuations for $(A_B/A_H)_{\pi^0}$ are again due to the differences of the hydrogen and butanol target. It seems, the fluctuations are more prominent for π^0 than η' , most probably due to the different kinematics of π^0 and η' . This indicates the necessity of determining the scaling factors for π^0 individually for each $\cos\theta$ -bin and the subsequent correction of these factors in order to get the η' scaling factors.

But since this procedure is rather time consuming and only four scaling factors are actually needed for η' , the scaling factors are ascertained directly from the η' missing mass spectra this time, as shown in figure 4.11. It works a bit better for the four energy bins than for the 11 energy bins because now the statistics per bin is much higher. A comparison of the η' missing mass spectra for the four and 11 energy bins indicates an equally well working principle.

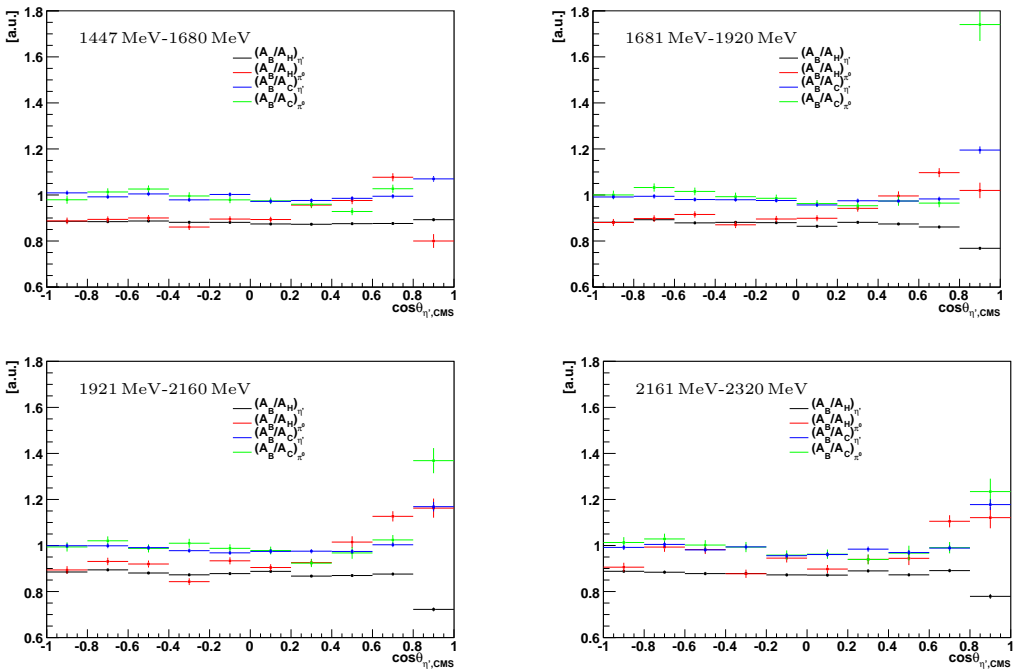


Figure 4.10.: The ratios of the acceptances for the four energy bins. The ratios corresponding to η' are almost constant over the entire angular range.

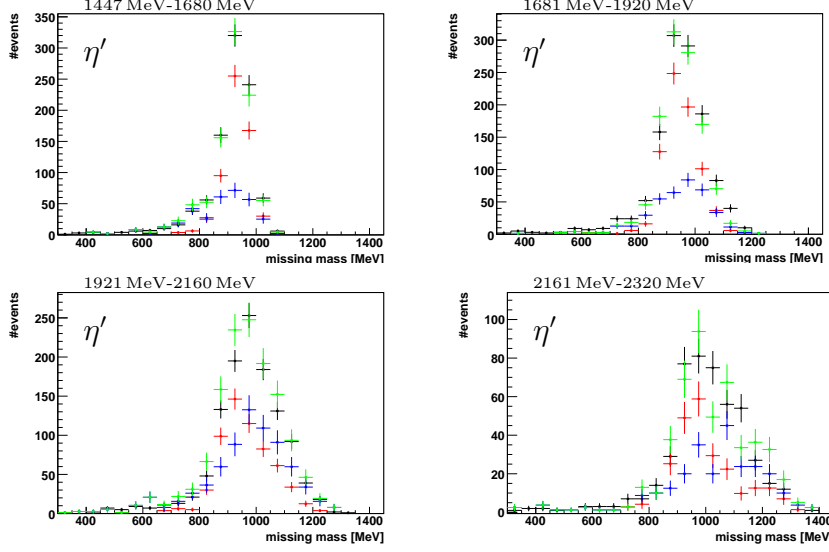


Figure 4.11.: The scaled missing mass spectra belonging to the hydrogen target (red) and carbon target (blue) are shown together with the butanol missing mass spectrum (black) and the results when adding the red and blue histograms (green) for four energy bins. These are needed for the $\cos \theta$ histograms.

Thereafter, the beam photon energy histograms of the hydrogen (red data points in figure 4.12) and carbon (blue in figure 4.12) beamtimes are scaled with the acquired η' scaling factors and added up (green in figure 4.12). Comparing the added histogram to the butanol histogram (black in figure 4.12) shows they are consistent with each other within the error bars except for the point at around $E_{\gamma_B} = 1900$ MeV that is most probably a spike/outlier. This indicates that the scaling factors were well determined. Besides, the same procedure is done for the $\cos \theta$ -histograms, which are shown in figure 4.13, in order to get the $\cos \theta$ dependency of the dilution factor for each energy bin. Again the green and black data points agree mostly well with each other.

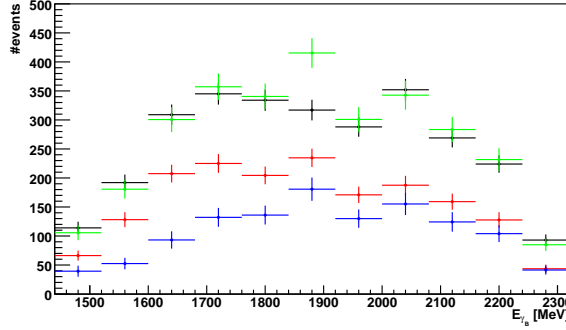


Figure 4.12.: The beam photon energy distributions for the butanol target (black), the hydrogen target scaled with s_H (red), the carbon target scaled with s_C and the sum of the latter two (green).

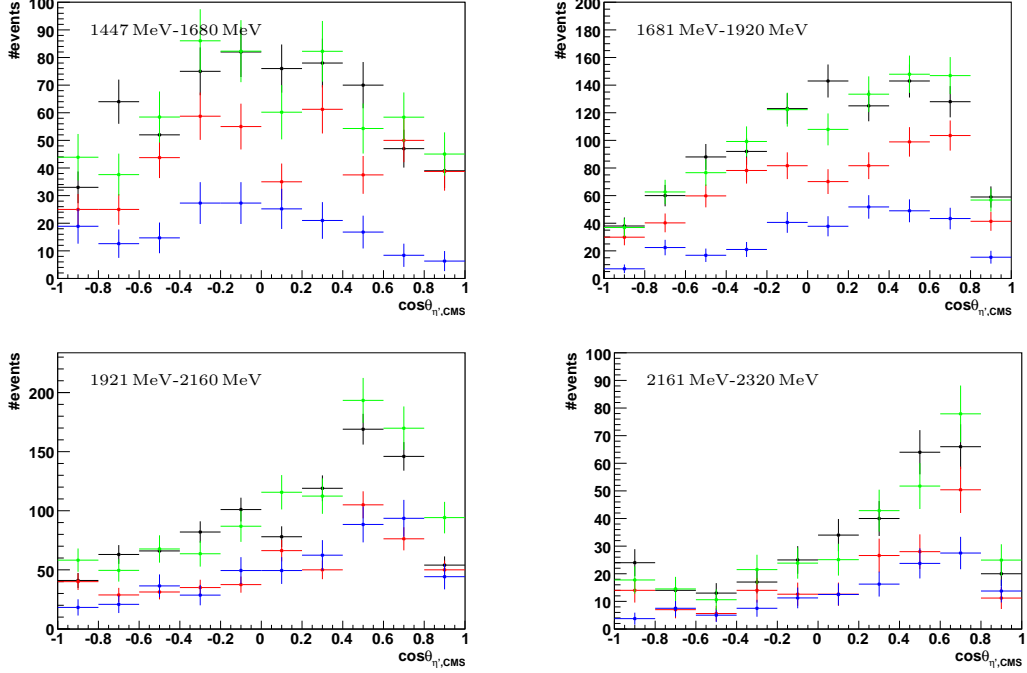


Figure 4.13.: The $\cos \theta$ - distributions for the butanol target (black), the hydrogen target scaled with s_H (red), the carbon target scaled with s_C and the sum of the latter two (green) for the four energy bins.

The dilution factor can be calculated now either with the hydrogen scaling factor s_H (compare red histogram in figure 4.14) or with the carbon scaling factor s_C (compare blue histogram in figure 4.14 and 4.15):

$$d = s_{H,\eta'} \cdot \frac{N_H}{N_B} = 1 - s_{C,\eta'} \cdot \frac{N_C}{N_B}, \quad (4.14)$$

whereas N_H , N_C and N_B denote beam photon energy or $\cos \theta$ spectra obtained with the corresponding target. In order to reduce the influence of spikes and reduce systematic errors originating from either the hydrogen or carbon beamtime, the average value of both method is taken for the dilution factor (green histogram in figure 4.14 and 4.15). Simultaneously, the error bars of the dilution factor are decreased.

Figure 4.14 shows the slight decrease of the dilution factor with higher beam photon energies. At lower energies the Fermi momenta of the bound protons (of e.g. carbon nuclei) are of the same order of magnitude as the momenta of the free protons (of hydrogen nuclei). The $\Delta\Phi$ and missing mass distributions are therefore broader for bound protons since energy and momentum conservation is not exactly described via equation (3.6) anymore. Thus, through the cuts on the coplanarity and missing mass cuts more free protons are chosen. At higher energies the influence of the Fermi motion is negligible due to the higher momenta of the protons. Thereby, the difference between bounded and free protons gets smaller. Hence, less bound protons can be removed by cuts and therefore the dilution factor decreases slightly.

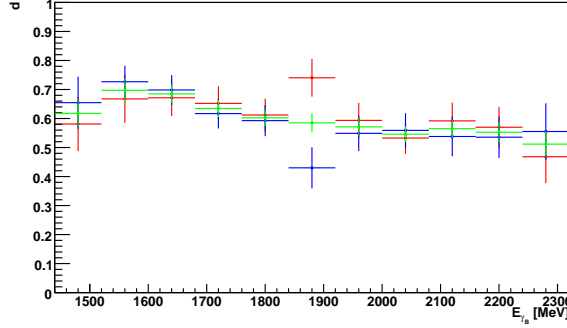


Figure 4.14.: The dilution factor in dependency of the beam photon energy extracted from the hydrogen data (red), carbon data (blue) and the average of both is shown in green.

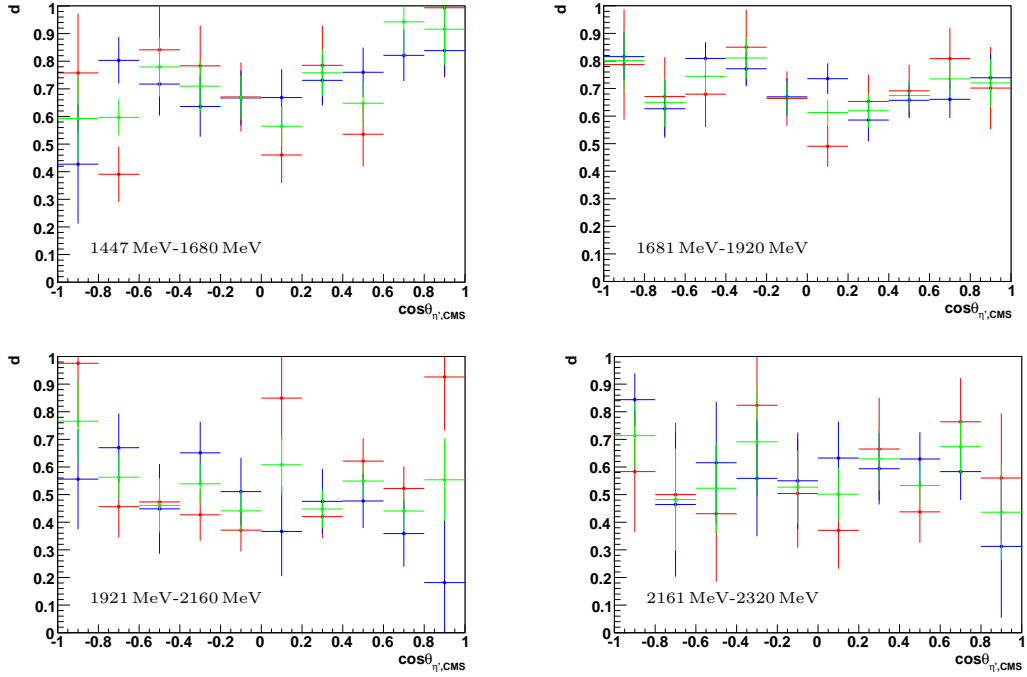


Figure 4.15.: The dilution factor in dependency of $\cos \theta$ extracted from the hydrogen data (red), carbon data (blue) and the average of both is shown in green for four different energy bins.

Results

Finally, figure 4.16 shows the development of the double polarization observable E in dependency of the beam photon energy. As it was already clear from the countrate difference, the sign of E is mostly positive. The interpretation considering the role of the resonances for η' is discussed in detail in section 4.6. The observable E is also plotted

4. Extraction of the double polarization observable E

as a function of $\cos \theta$ in figure 4.17 for the four energy bins. All errors are of statistical origin.

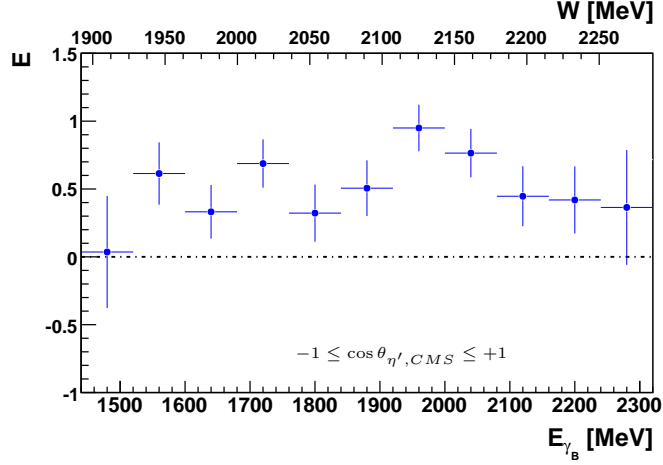


Figure 4.16.: The double polarization observable E as a function of the beam photon energy. It is determined with the dilution factor.

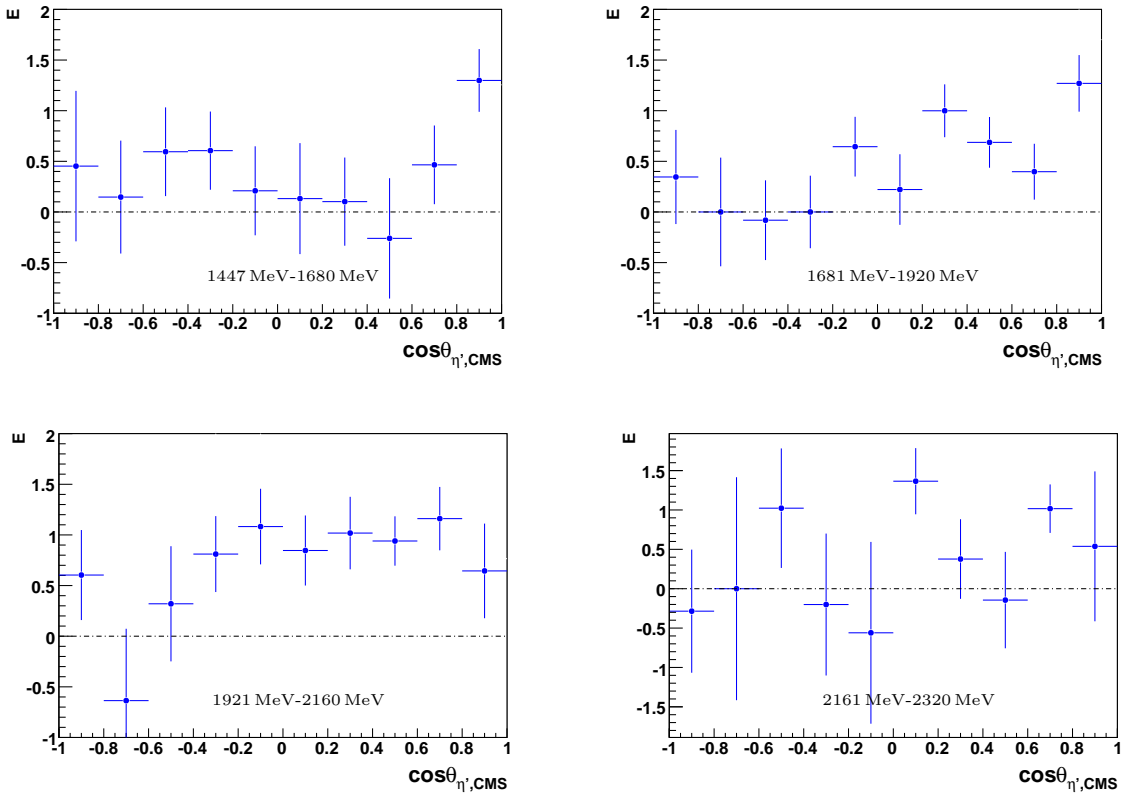


Figure 4.17.: The double polarization observable E as a function of $\cos \theta$ for four different energy bins. It is determined with the dilution factor.

4.3. Determination of E using the hydrogen data

Instead of trying to estimate the hydrogen percentage of the selected events with the dilution factor, it is possible to use the hydrogen data directly without any carbon contamination. Using equation (4.5), the observable E can also be calculated in the following way:

$$E = \frac{\frac{d\sigma}{d\Omega_B}^{1/2} - \frac{d\sigma}{d\Omega_B}^{3/2}}{2 \frac{d\sigma}{d\Omega_H}} \cdot \frac{1}{p_T p_\gamma} \quad (4.15)$$

$$= \frac{\left(N_B^{1/2*} - N_B^{3/2*}\right) \cdot (A_B n_T^B)^{-1}}{2 N_H \cdot (A_H n_\gamma^H n_T^H)^{-1}} \cdot \frac{1}{p_T p_\gamma}. \quad (4.16)$$

Here, $N_B^{1/2*}$ and $N_B^{3/2*}$ are the countrates that are already flux normalized. Since $N_B^{1/2}$ and $N_B^{3/2}$ each consist of six terms (compare equations 4.1 and 4.2), the formula 4.16 has to be corrected by this factor:

$$E = \frac{\left(N_B^{1/2*} - N_B^{3/2*}\right) \cdot (A_B n_T^B)^{-1}}{12 \cdot N_H \cdot (A_H n_\gamma^H n_T^H)^{-1}} \cdot \frac{1}{p_T p_\gamma}. \quad (4.17)$$

In contrast to the dilution factor method, the photon flux and the acceptance need to be calculated explicitly in order to obtain the observable E. The target area density is given by $n_T^B = 0.8706 \cdot 10^{23} \text{ cm}^{-2}$ for the butanol target and $n_T^H = 2.157 \cdot 10^{23} \text{ cm}^{-2}$ for the hydrogen target (compare section 2.3).

The photon flux

The photon flux specifies the number of photons which reach the target and initiate a reaction. The photon flux used in this thesis was calculated individually for all beam times and all four possible spin configurations by Manuela Gottschall. A detailed explanation about the calculation process can be found in her thesis [Got] and it is not further explained here. The results are shown in figure 4.18. All flux histograms show the characteristic $1/E_{\gamma_B}$ dependency due to the bremsstrahlung process. The histograms start at approximately 400 MeV since the beam photons are only tagged if their energy lies above the tagging threshold. Fluctuations are visible because the electron hits are registered by many different scintillating fibers and bars of the tagging system with different detector efficiencies.

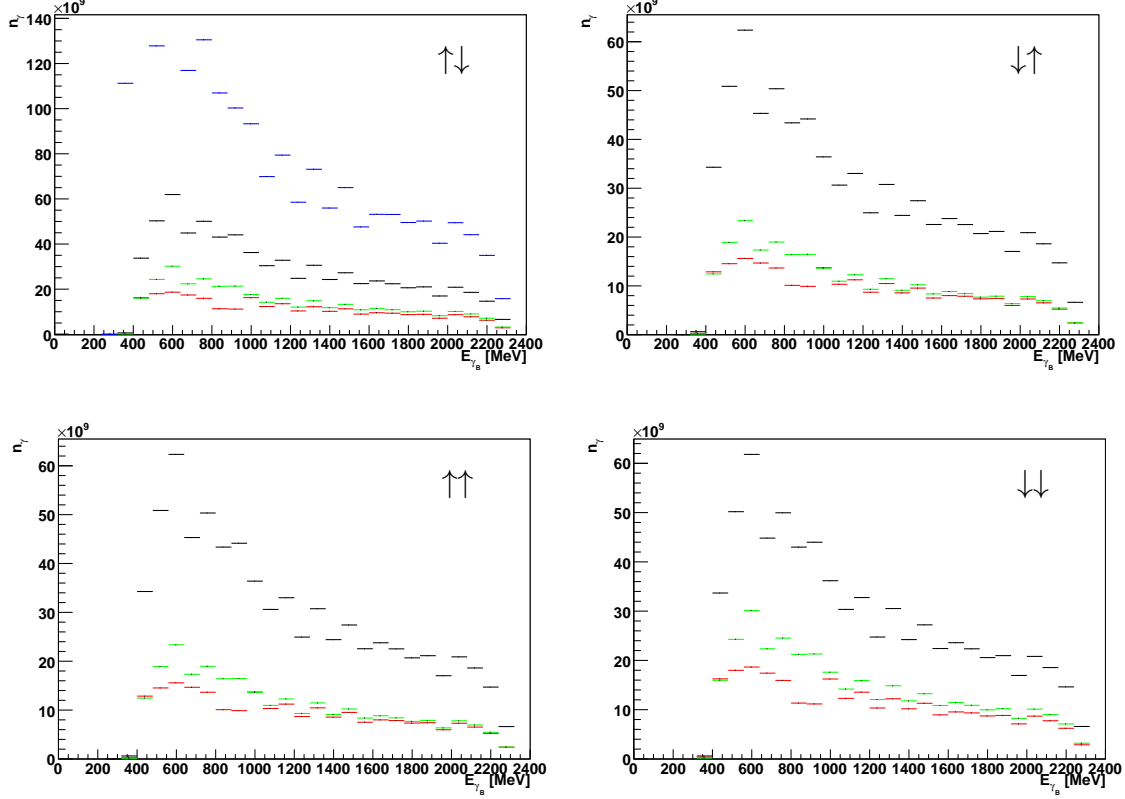


Figure 4.18.: The photon flux for all four helicity configurations and all used beamtimes (black: N09, green: S09 and red: N07). For comparison reasons, the flux of the hydrogen data (blue: N08) is depicted in the plot on the left top side.

The acceptance

The acceptance describes the probability for reconstructing a generated event. For its determination the Monte Carlo data are used. Here, the detector geometry of each detector is implemented. Applying the same cuts to the Monte Carlo data as to the measured data allows to further investigate the analysis efficiency. The acceptance is given by the ratio of reconstructed to generated events:

$$A(E_{\gamma_B}, \cos \theta_{\eta', CMS}) = \frac{N_{rec}(E_{\gamma_B}, \cos \theta_{\eta', CMS})}{N_{gen}(E_{\gamma_B})}. \quad (4.18)$$

Figure 4.19 shows a rather smooth course of the acceptance over the entire beam photon energy range except for a bump at 1800 MeV and amounts approximately 50% in average. Besides, the acceptance is slightly higher for the hydrogen target in comparison to the butanol target. The butanol target is a more dense target than the hydrogen target and has therefore a higher probability for multiple scattering.

In figure 4.20 the acceptance is plotted as a function of $\cos \theta_{\eta', CMS}$ for the four energy bins. A decrease in the development of the acceptance can be noticed sometimes. This originates

from the absence of 2PED events. A comparison of the 3PED and 2PED acceptances can be found in A.5. The proton does not get detected if it flies in the small gap between the Forward and MiniTAPS detector ($\cos \theta_{\eta',CMS} \approx -0.7$ in the last three energy bins) or the small gap between Crystal Barrel and Forward detector ($0 < \cos \theta_{\eta',CMS} < 0.2$ in the last two energy bins and for $\cos \theta_{\eta',CMS} > 0.2$ in the second energy bin). Additionally, low energetic protons fly towards backward direction which corresponds to the forward direction of η' ($0.8 < \cos \theta_{\eta',CMS} < 1$) and get lost in the surrounding material.

Figure 4.19: The acceptance of the decay channel $\eta' \rightarrow \gamma\gamma$ as a function of the beam photon energy and the entire angular range for the butanol target (black points) and hydrogen target (red points).

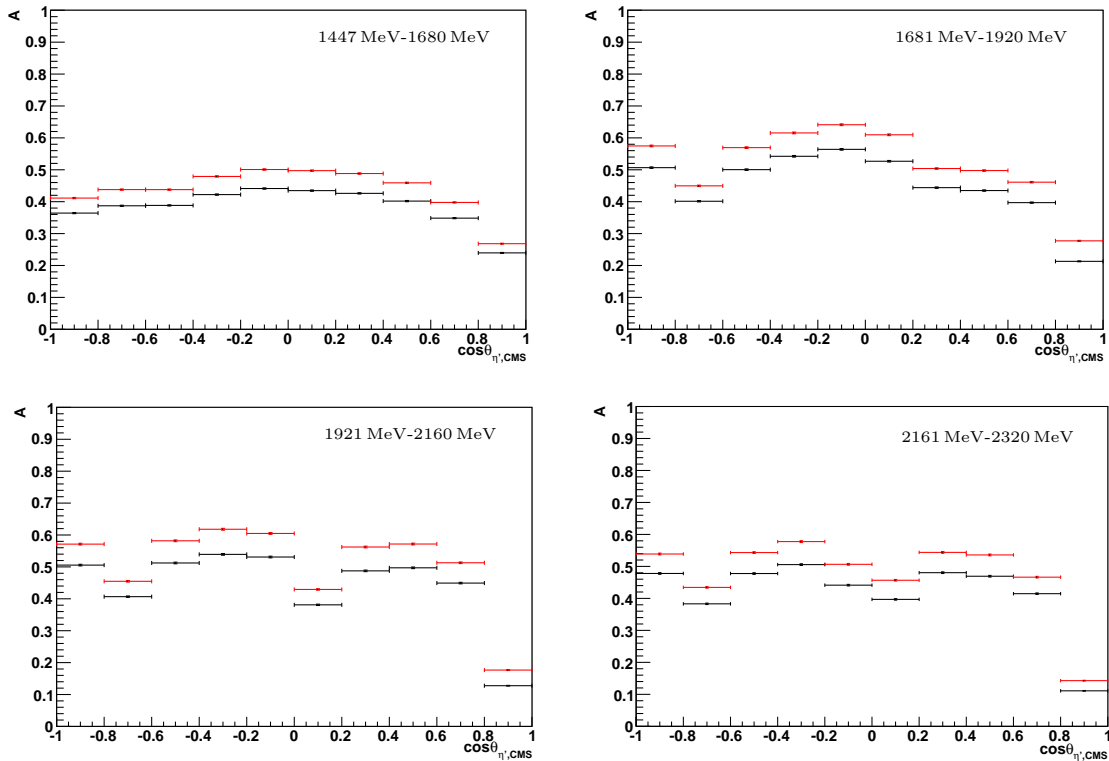
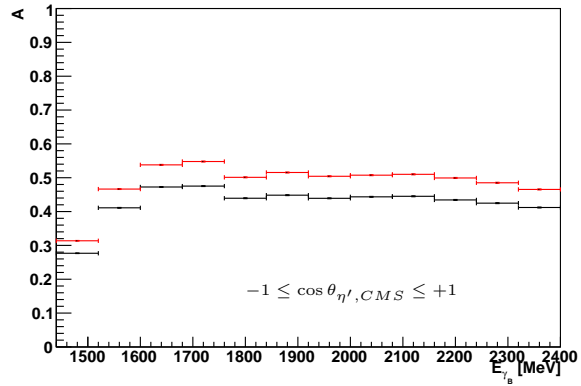


Figure 4.20.: The acceptance of the reaction $\gamma p \rightarrow \eta' p \rightarrow \gamma\gamma p$ is shown here as a function of $\cos \theta_{\eta',CMS}$ for four energy bins. In forward direction a decrease in the development of the acceptances is observed which originates from the absence of 2PED events.

Results

The results for the double polarization observable E are shown in figure 4.21 and 4.22.

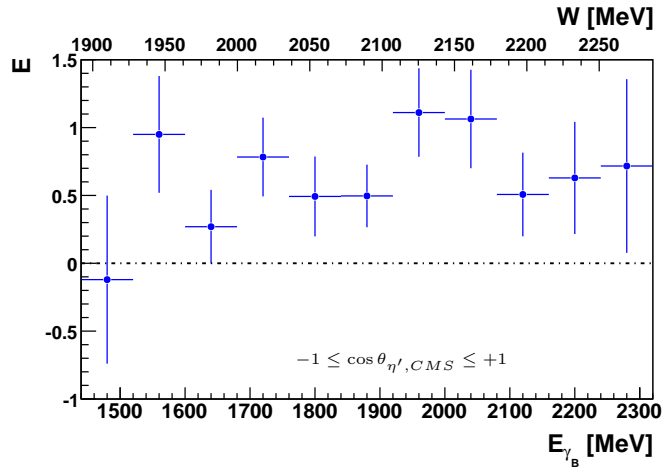


Figure 4.21.: The double polarization observable E as a function of the beam photon energy determined with the hydrogen data.

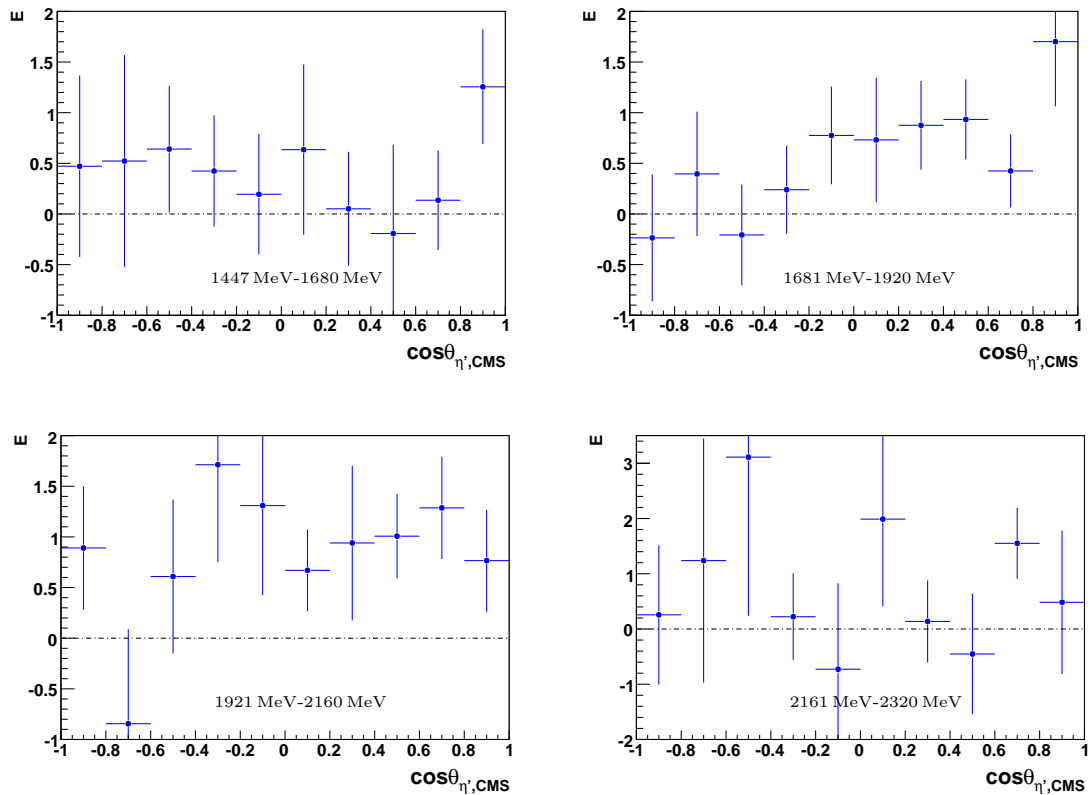


Figure 4.22.: The double polarization observable E as a function of $\cos \theta_{\eta',CMS}$ for four energy bins. The observable E is determined with the hydrogen data.

4.4. Determination of E using the cross section fits

Instead of using data taken with the hydrogen target, it is possible to use fits for the differential and total cross section (see section 1.2). It has the advantage of not relying on the low statistics of the hydrogen beamtime. Since the data used in this thesis was taken at the CBELSA/TAPS experiment, the fit results of Huang et al. [HHN12] to the previous measurements with the CBELSA/TAPS experiment [Cea09] are used here. Starting with formula 4.16, this leads to

$$E(\cos \theta) = \frac{\frac{d\sigma}{d\Omega}^{1/2} - \frac{d\sigma}{d\Omega}^{3/2}}{2 \frac{d\sigma}{d\Omega}_{fit}} \cdot \frac{1}{p_T p_\gamma} = \frac{\left(N_B^{1/2*} - N_B^{3/2*} \right) \cdot (A_B n_T^B \Gamma \Delta \Omega)^{-1}}{12 \cdot \frac{d\sigma}{d\Omega}_{fit}(\cos \theta)} \cdot \frac{1}{p_T p_\gamma}. \quad (4.19)$$

The branching ratio is given by $\Gamma_{\eta' \rightarrow \gamma\gamma} = 2.22\%$ and the solid angle interval by $\Delta \Omega = 2\pi \cdot \cos \theta$. Here, $\cos \theta = 0.2$ which corresponds to the chosen bin width. For the energy dependency of the observable E , the total cross section of the fits are needed which are given by $\sigma_{fit} = \sum_{\cos \theta = -1}^1 \frac{d\sigma}{d\Omega}_{fit}(\cos \theta)$. Now the observable E is determined by:

$$E(E_{\gamma_B}) = \frac{\sigma_B^{1/2} - \sigma_B^{3/2}}{2\sigma_{fit}} \cdot \frac{1}{p_T p_\gamma} = \frac{\left(N_B^{1/2*} - N_B^{3/2*} \right) \cdot (A_B n_T^B \Gamma)^{-1}}{12\sigma_{fit}} \cdot \frac{1}{p_T p_\gamma}. \quad (4.20)$$

Results

The obtained double polarization observable E is depicted in figure 4.23 and 4.24.

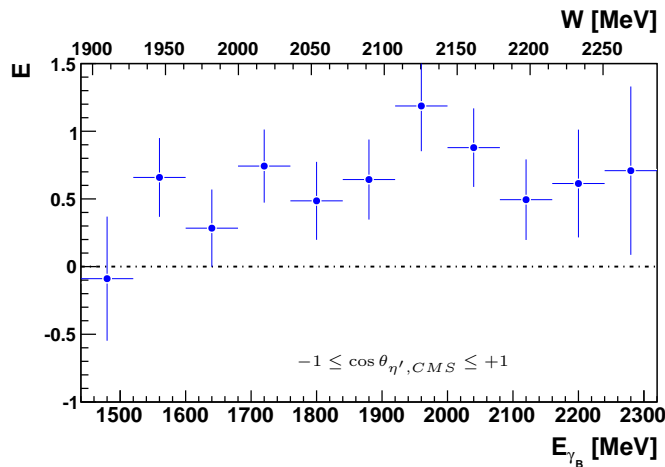


Figure 4.23.: The double polarization observable E determined with the cross section fit of Huang et al. [HHN12] in dependency of the beam photon energy.

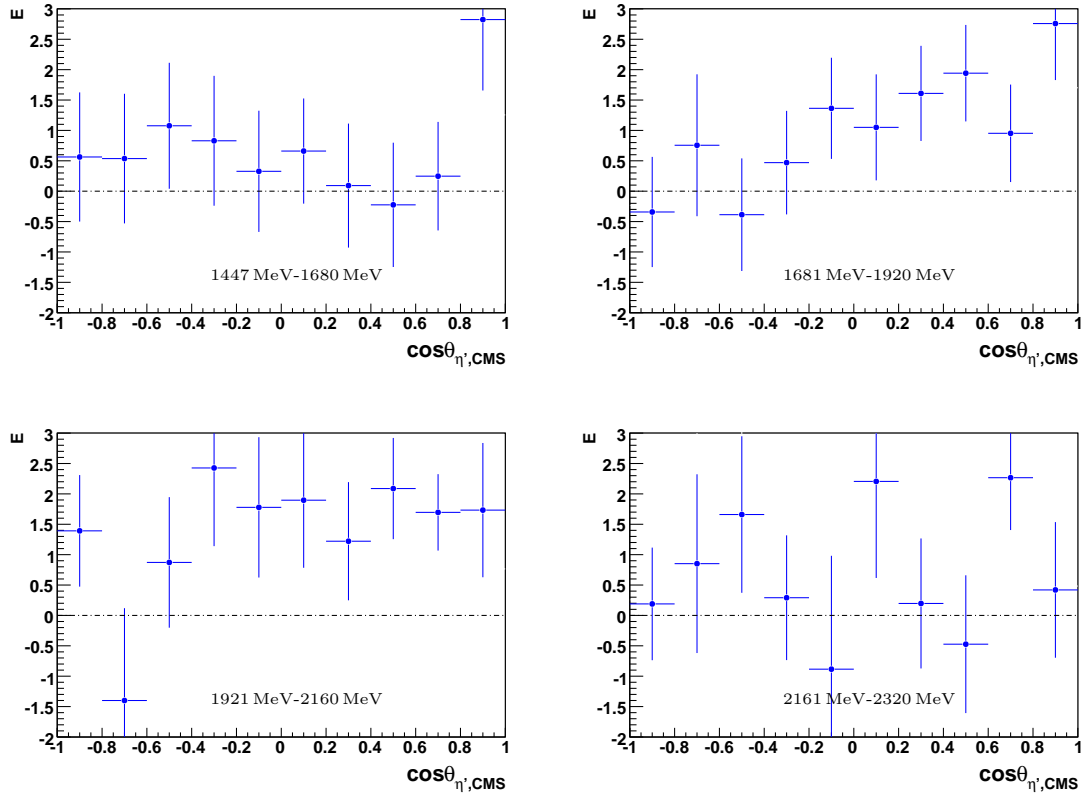


Figure 4.24.: The double polarization observable E as a function of $\cos \theta_{\eta',\text{CMS}}$ for four energy bins. E is determined with the fits to the differential cross section of Huang et al. [HHN12] to the CBELSA/TAPS data [Cea09].

4.5. Comparison of the methods

Three methods were presented that can be used to determine the double polarization observable E . They are compared with each other by means of figure 4.25 where the observable E is depicted as a function of the beam photon energy for all three methods. All methods show a similar development of the double polarization observable E over the complete energy range because the countrate difference is almost the same for all three methods. Within their error margins, all three methods are consistent with each other. The errors of the first method are the smallest of all. In this method, only the statistical errors of $N_{1/2,B}$ and $N_{3/2,B}$ play a role alongside the error of the dilution factor. A systematic error of the dilution factor can occur since the scaling factors were determined first for π^0 and then corrected for η' . In order to reduce or completely avoid a possible systematic error of the dilution factor, it was ascertained with the hydrogen and carbon data and subsequently the average value was taken. Nevertheless, a thorough investigation should be done in the future regarding this matter.

For the second method not only the statistical errors of the butanol data but also of the hydrogen data need to be considered together with the errors of the flux and the

acceptance. Therefore, the error bars are larger for the second method than for the first method. Furthermore, the selected events of the data taken with the hydrogen target is based on only 1300 events. Small deviations between the second and the other methods exist e.g. at $E_{\gamma_B} \approx 1580$ MeV, even though the three methods are consistent with each other within their uncertainties, which originates most likely from statistical fluctuations in the hydrogen data. Furthermore, there could be a probable systematic error of the photon flux which should be investigated in the future.

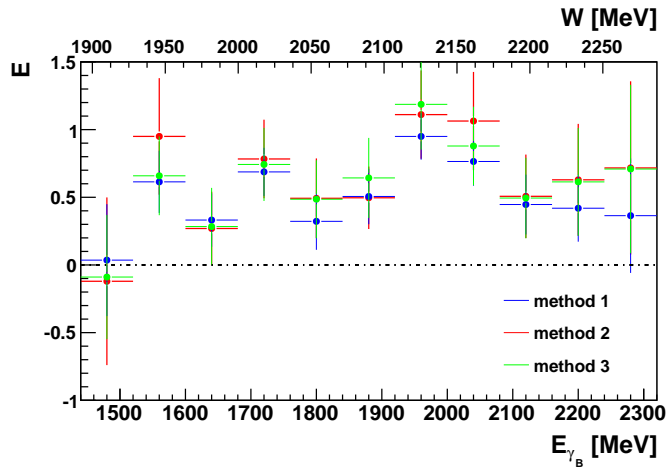


Figure 4.25.: The results for the observable E obtained with method 1 (blue), method 2 (red) and method 3 (green) are compared with each other.

For the third method, the same holds as for the second method except for the influence of the hydrogen data. Instead, this method has the disadvantage of being model dependent since the development of the differential and total cross section of η' differs due to the existing deviations of the CLAS and CBELSA/TAPS data (compare section 1.2). The results of the third and the second method agree very well with each other, especially for higher energies. Thus, it does not matter whether the cross section of the hydrogen data obtained from the decay channel $\eta' \rightarrow \gamma\gamma$ (second method) or the fit result of Huang et al. for the cross section based on the decay channel $\eta' \rightarrow \pi^0\pi^0\eta$ [Cea09] (third method) is used in order to determine the observable E . This indicates a consistency of the cross section data with the previous data of the CBELSA/TAPS collaboration. If the fit to the CLAS cross section is taken, large deviations between the third method and the other two methods are visible for higher beam photon energies as expected from the deviations of the CLAS and CBELSA/TAPS data (compare figure A.7).

Besides, all three methods use the polarization factor $1/(p_T p_\gamma)$. The target polarization p_T can lead to a systematic error of approximately 2% [Dut11] and the beam photon polarization p_γ to a systematic error of approximately 0.3% [Kam09].

Summarizing, it seems that the results of the first method are the most reliable, since the first method is not dependent on the flux or on a model and thus has less influence of systematic errors. Furthermore, both the first and second method were tested for the final state $\pi^0 \rightarrow \gamma\gamma$ and compared to the results of Manuela Gottschall (see figure A.4).

Both methods agree well with Manuela Gottschall's results which indicates the successful implementation of both methods.

4.6. Interpretation of the results

As mentioned in the introduction (compare section 1.2), both Tiator et al. [Tia07, Tia12] and Huang et al. [HHN12] predict within their models which resonances play an important role in the photoproduction of η' .

4.6.1. Comparison to fit results of Tiator et al.

First, all three predictions of Tiator et al. are compared to the results (see figure 4.26 and 4.27). The fit results of Tiator et al. are given in table 4.1.

	fit 1				fit 2			
resonance	M^* [MeV]	Γ_{tot} [MeV]	$\chi_{1/2}$	$\chi_{3/2}$	M^* [MeV]	Γ_{tot} [MeV]	$\chi_{1/2}$	$\chi_{3/2}$
$S_{11}(M^*)$	2123	132	87	-	1904	157	157	-
$P_{11}(M^*)$	-	-	-	-	2083	51	25	-
$P_{13}(M^*)$	1958	123	11	-39	1926	146	-15	10
$D_{13}(M^*)$	2143	212	102	-2	2100	91	65	-65

	fit 3				
resonance	M^* [MeV]	Γ_{tot} [MeV]	$\chi_{1/2}$	$\chi_{3/2}$	
$S_{11}(M^*)$	1961	358	209	-	
$P_{11}(M^*)$	2083	51	18	-	
$P_{13}(M^*)$	2065	74	-30	-57	
$D_{13}(M^*)$	2100	120	78	-94	

Table 4.1.: The three fit results of the η' -MAID model for the mass, the width and the effective couplings $\chi \propto A$ to the resonances for both spin configurations. Fit 1 does not include a P_{11} resonance. [Tia07, Tia12]

Overall, all three predictions show a different behavior for the observable E in dependency of the beam photon energy than the data. According to the fits, there should be a strong presence of a spin 1/2 resonance (e.g. $S_{11}(1904)$ of fit 2 or $S_{11}(1961)$ of fit 3) near threshold as the observable E is supposed to be one. But in the very first energy bin in figure 4.26, E is zero within the error bars which means there is equal strength of spin 1/2 and 3/2 resonances or there is only a 3/2 resonance with equal coupling strength $A_{1/2}$ and $A_{3/2}$. Furthermore, the development of E in dependency of $\cos\theta$ in the energy range of 1447 MeV-1680 MeV does not agree at all with Tiator's fits. This could indicate the necessity of e.g. the PDG resonance $P_{13}(1900)^{**}$ or a subthreshold

P_{13} resonance in addition to the S_{11} resonance near threshold. Another possibility are statistical fluctuations which can not be ruled out due to the low statistics, the results of the observable E are based on.

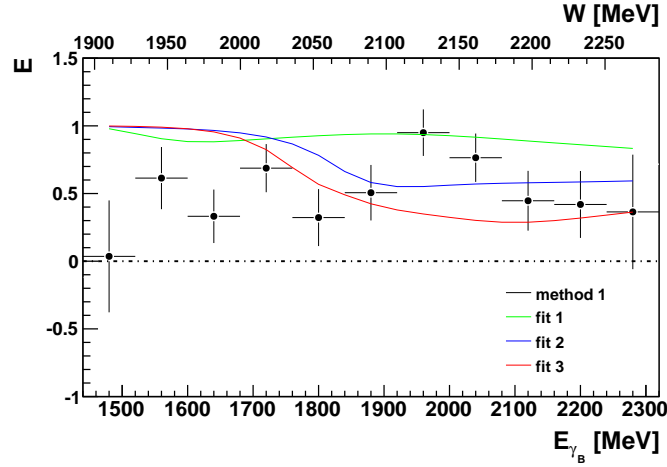


Figure 4.26.: The double polarization observable E determined with the first method is plotted together with three predictions of Tiator et al. [Tia07, Tia12].

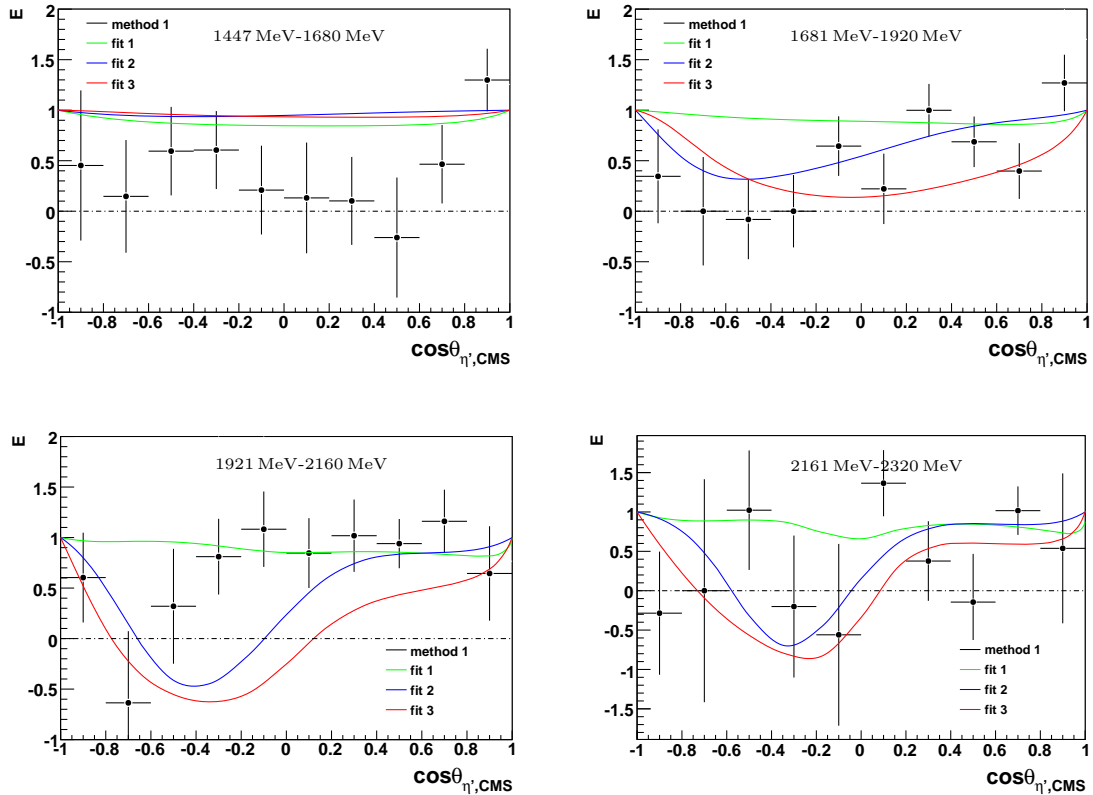


Figure 4.27.: The double polarization observable E as a function of $\cos \theta_{\eta',\text{CMS}}$ for four energy bins. The predictions of Tiator et al. [Tia07, Tia12] are depicted as well.

In the second energy range of 1681 MeV-1920 MeV, both figure 4.26 and 4.27 show a better agreement of fit 2 and 3 to the development of E than fit 1. Thus a better description of E is achieved when the $P_{11}(2083)$ resonance is not switched off as it is done in fit 1. The observable E reaches the value one in the third energy range of 1921 MeV-2160 MeV. Besides, figure 4.27 shows in the third plot how well the results for the observable E agree with fit 1 except for two data points in backward direction, where a $S_{11}(2123)$ resonance is considered.

4.6.2. Comparison of $\sigma_{1/2}$ and $\sigma_{3/2}$

The results for the observable E are used to ascertain the cross section for both spin configurations ($s=1/2$ and $s=3/2$). It holds:

$$\sigma_{1/2} - \sigma_{3/2} = 2\sigma_{tot}Ep_Tp_\gamma \quad (4.21)$$

$$\sigma_{1/2} + \sigma_{3/2} = 2\sigma_{tot} \quad (4.22)$$

$$\Rightarrow \sigma_{1/2} = \sigma_{tot}(1 + Ep_Tp_\gamma) \text{ and } \sigma_{3/2} = \sigma_{tot}(1 - Ep_Tp_\gamma), \quad (4.22)$$

whereas σ_{tot} is taken from the Huang et al.'s fits. They are plotted as a function of the beam photon energy for both the CLAS and CBELSA/TAPS cross sections (compare figure 4.28). The results of Huang et al. are listed in table 4.2 (compare also figure 1.5).

CLAS				
resonance	M^* [MeV]	Γ_{tot} [MeV]	$\chi_{1/2}$	$\chi_{3/2}$
$P_{13}(1720)$	1720	200	0.09 ± 0.03	-0.16 ± 0.05
$P_{13}(2050)$	2050 ± 4	140 ± 10	-5.71 ± 0.17	9.89 ± 0.30
$S_{11}(1925)$	1924 ± 4	112 ± 7	-11.84 ± 0.41	-
$P_{11}(2130)$	2129 ± 5	205 ± 12	-11.34 ± 0.62	-
CBELSA/TAPS				
resonance	M^* [MeV]	Γ_{tot} [MeV]	$\chi_{1/2}$	$\chi_{3/2}$
$P_{13}(1720)$	1720	200	0.09 ± 0.06	-0.13 ± 0.09
$P_{13}(2050)$	2045 ± 7	52 ± 184	-2.02 ± 0.26	7.31 ± 0.93
$S_{11}(1925)$	1926 ± 10	99 ± 23	-11.07 ± 1.43	-
$P_{11}(2130)$	2123 ± 23	246 ± 54	-18.80 ± 0.90	-

Table 4.2.: The fit results of Huang et al. for the CLAS and CBELSA/TAPS data. The mass, the width and the effective couplings $\chi \propto A$ to the resonances for both spin configurations are given. The mass and the total width of the subthreshold $P_{13}(1720)^{****}$ are fixed according to the PDG. [HHN12]

The advantage of plotting $\sigma_{1/2}$ and $\sigma_{3/2}$ is that the S_{11} and P_{11} resonances are switched off in $\sigma_{3/2}$ (compare quantum numbers in table 1.1), so that small contributions of resonances

with $J=3/2$ or higher are visible. The model calculations of Huang et al. suggest an existence of the $S_{11}(1925)$ resonance near threshold, the $P_{13}(2050)$ and $P_{11}(2130)$ for higher energies. There are little indications for the former two resonances as shown in figure 4.28. But more data is needed in order to be certain. The cross section for parallel spin configuration $\sigma_{3/2}$ drops to $0 \mu\text{b}$ and $\sigma_{1/2}$ shows a resonance like structure around 2120 MeV. This gives evidence for the proposed $P_{11}(2130)$ resonance since this resonance does not contribute to $\sigma_{3/2}$. Whether it is indeed the $P_{11}(2130)$ resonance or the $S_{11}(2123)$ suggested by Tiator et al. can not be extracted from the data, but both are possible. Overall, there is a clear dominance of $\sigma_{1/2}$ visible which is consistent with the overall positive sign of E .

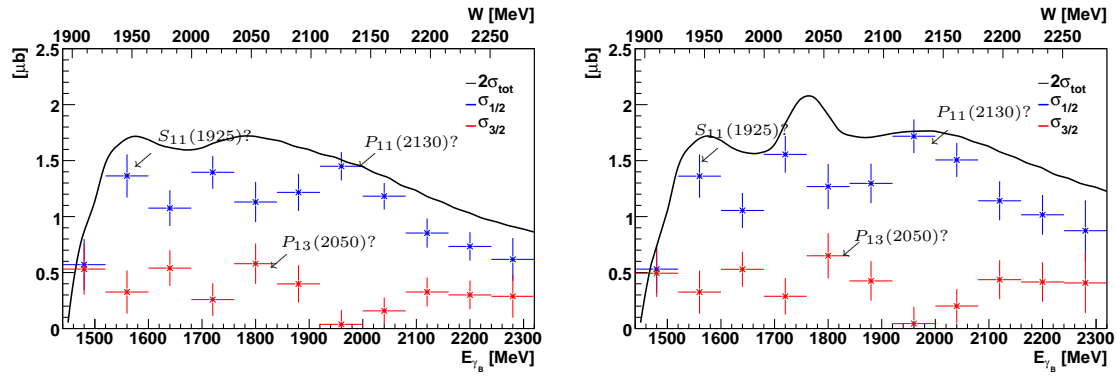


Figure 4.28.: The cross sections $\sigma_{1/2}$, $\sigma_{3/2}$ and $-2\sigma_{tot}$ are plotted together for the entire beam photon energy range. For comparison reasons, The results for $\sigma_{1/2}$ and $\sigma_{3/2}$ are shown when using σ_{tot} from the fits of the CLAS (left) and CBELSA/TAPS (right) differential cross section data [HHN12].

5. Summary

The investigation of the nucleon excitation spectrum through photoproduction reactions allows the study of the dynamics of constituents inside the nucleon. Currently, many more resonance states are predicted for higher masses by constituent quark models than there have been experimentally observed until now. Due to the high η' mass $m_{\eta'} = 958 \text{ MeV}$, the photoproduction of η' gives access to these high-lying resonances ($M_{N^*} > 1892 \text{ MeV}$). The measurement of the cross section gives only information about the sum of all resonances that decay in $\eta' p$. Furthermore, the broad resonances overlap strongly. Thus, additional measurements of polarization observables are necessary in order to disentangle all resonance contributions.

In this work, the double polarization observable E was determined in the photoproduction reaction $\vec{\gamma}\vec{p} \rightarrow \eta' p$ for a beam photon energy range of $1447 \text{ MeV} - 2320 \text{ MeV}$ for the first time. The analyzed data was taken at the CBELSA/TAPS experiment at ELSA in Bonn. A circularly polarized photon beam was used in combination with a longitudinally polarized butanol target.

The two decay modes $\eta' \rightarrow \gamma\gamma$ and $\eta' \rightarrow \pi^0\pi^0\eta$ were carefully reconstructed by using appropriate kinematic cuts. Additionally, a kinematic fit was successfully applied to the butanol data for the latter decay channel. Approximately 2400 and 1700 events were reconstructed for both decay channels, respectively.

Since the photon has a spin of $s = 1$ and the proton of $s = 1/2$, two spin configurations with a total spin of $1/2$ or $3/2$ are possible. The observable E describes the asymmetry between both helicity dependent cross sections. In this thesis, three different methods were tested in order to extract the observable E. Firstly, the observable E was determined by using the cross section asymmetry which is corrected with the dilution factor. The dilution factor gives the percentage of polarizable protons to all selected protons of the butanol data. The second possibility is given by replacing the sum of the cross sections measured with the butanol target with the cross section obtained with the hydrogen target. The third method uses instead fits that were performed to existing cross section data. The results of all three methods were consistent with each other within their error bars. The preliminary results of the observable E show an overall positive sign of E. Additionally, the comparison of the helicity dependent cross sections $\sigma_{1/2}$ and $\sigma_{3/2}$ shows a clear dominance of $\sigma_{1/2}$ in the photoproduction of η' . Furthermore, there is indication for the $S_{11}(2123)$ resonance suggested by Tiator et al. or $P_{11}(2130)$ resonance proposed by Huang et al. Both can probably be identified with the existing one-star PDG resonances ($S_{11}(2090)^*$ and $P_{11}(2100)^*$). Deviations to the η' -MAID model were observed as well. Thus, the obtained results will give new information for model calculations. All in all, this work demonstrates the importance of investigating the photoproduction re-

5. Summary

action $\gamma p \rightarrow \eta' p$. With improved statistics and thus smaller error bars in the future, it should be possible to get more precise results and hence to extract more information about high-lying resonances of the nucleon excitation spectrum.

A. Appendix

A.1. Example for a xml file

```
<explora>

<CBTAnalyseManager name="2ped"> <!-- container="p_pi0" -->
    <!-- = section to define base conditions, like uncharged... ===== -->
    <CBTRactionBaseConditions>
        <CBTParticleDefinition Role="target" Name="proton"/>
        <CBTIncludeXML file=".//ParticleCategories/Uncharged.xml"/>
        <CBTIncludeXML file=".//ParticleCategories/Charged.xml"/>
        <CBTIncludeXML file=".//ParticleCategories/Beam.xml"/>
        <CBTParticleFactory refname="mesonfactory" Name="pi0" container="pi0select">
            <CBTKombinatorik Name="ggCombine" Debug="0"
                Source="uncharged(2/2), uncharged(2/2)" Dstcontainer="ggrav"
                Persistent="Yes"/>
            <CBTParticleSelector Name="pi0" Source="ggrav" pdgname="pi0">
                <CBTHMassCut Min="0.0" Max="3000.0"/>
            </CBTParticleSelector>
        </CBTParticleFactory>
    </CBTRactionBaseConditions>
    <!-- = analyzing a special ped topology, e.g. 2 ped events ===== -->
    <CBTIncludeXML defineflag="REACTION=p_pi0"
        file=".//Selections/myProton23PED_mp.xml"/>
</CBTAnalyseManager>
</explora>
```

Figure A.1.: An example for a xml file. Here, the two photons of the final state for the decay mode $\eta' \rightarrow \gamma\gamma$ are combined to a meson.

A.2. Invariant mass of 2PED events

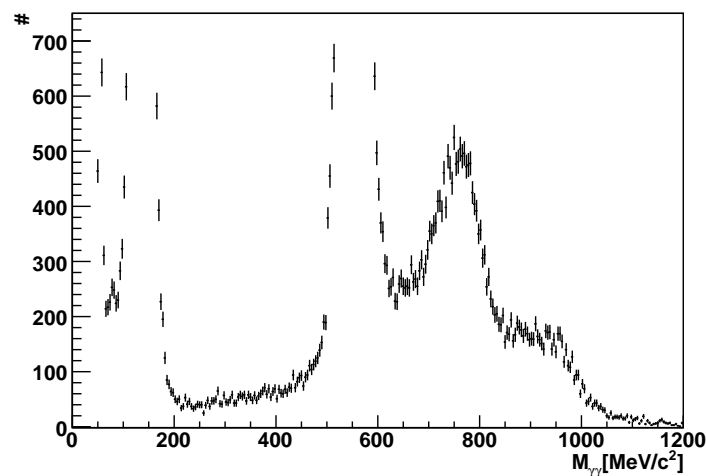


Figure A.2.: The invariant mass of 2PED events where the proton of the final state was not detected. The η' -peak is barely visible.

A.3. Pull distributions

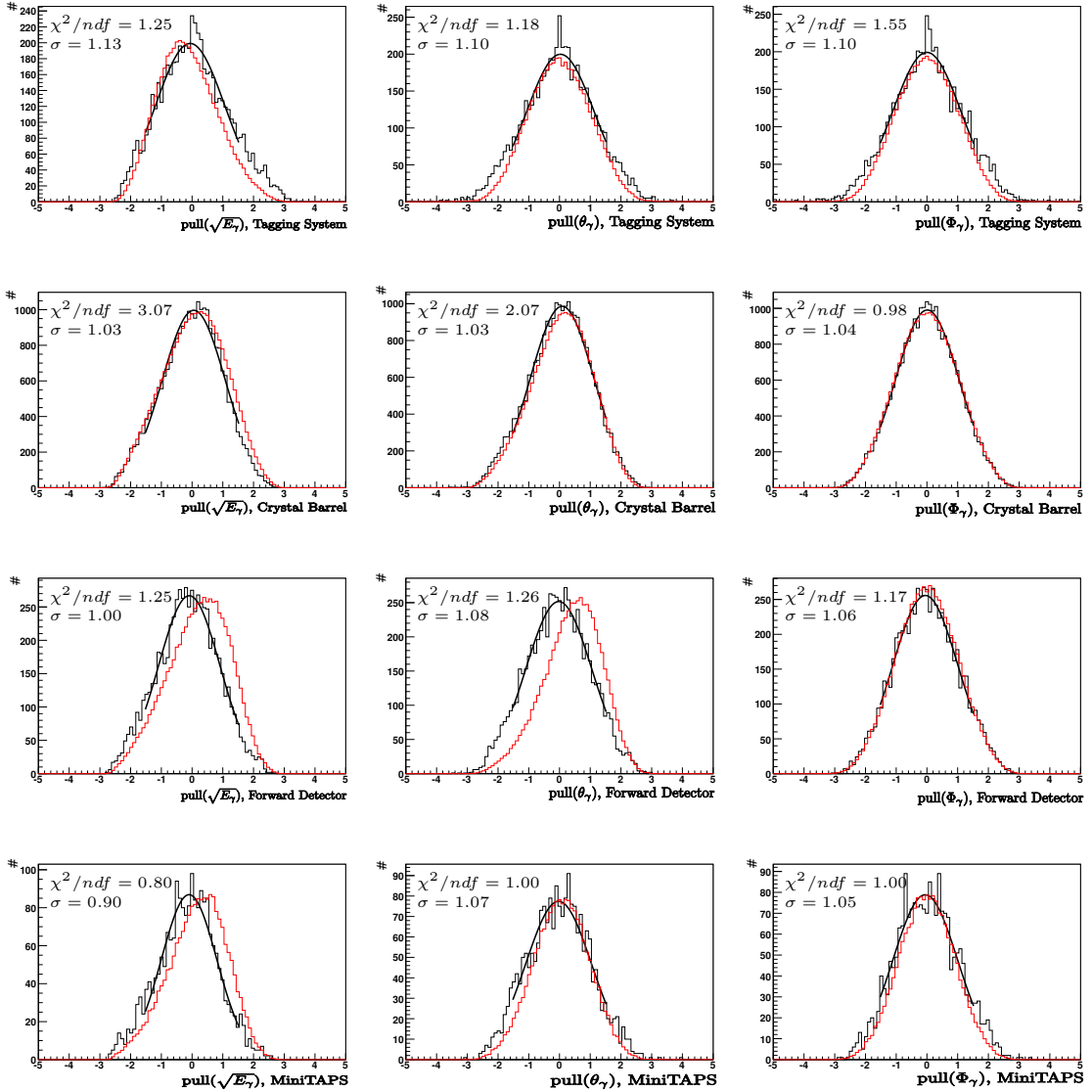


Figure A.3.: Pull distributions for the measured values $\sqrt{E_\gamma}$, θ_γ , Φ_γ of the beam photon and the six decay photons detected in the Crystal Barrel, Forward Detector and MiniTAPS Detector. A gaussian function is fitted to the data for a range of ± 2 (black). Additionally, the Monte Carlo distributions are depicted as well (red). Deviations of data and Monte Carlo distributions exist due to probable errors in the Monte Carlos.

A.4. The observable E for $\pi^0 \rightarrow \gamma\gamma$

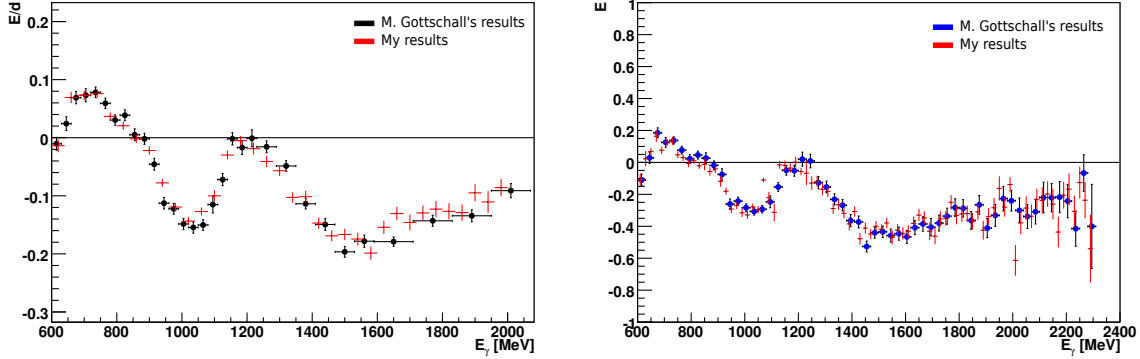


Figure A.4.: The observable E (or rather E/d) determined for the photoproduction reaction $\gamma p \rightarrow \pi^0 p$ obtained with method 1 (left) and 2 (right). For comparison reasons, M. Gottschall's results are plotted as well [Got].

A.5. The acceptance for $\eta' \rightarrow \gamma\gamma$

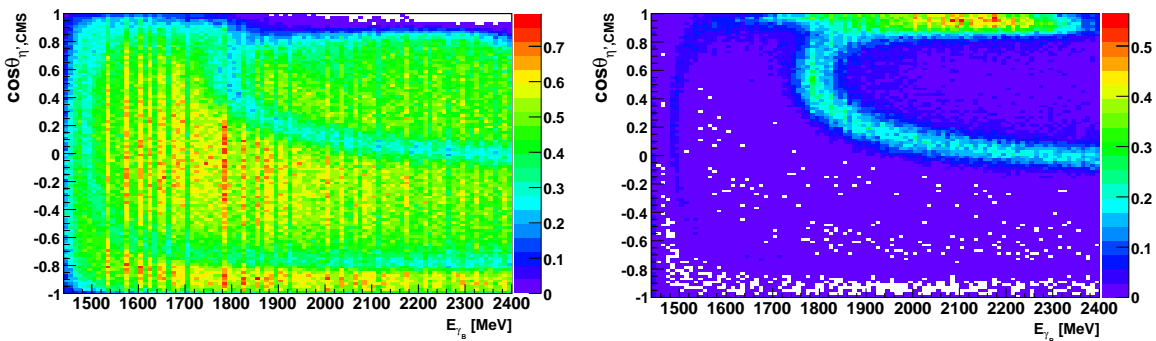


Figure A.5.: The acceptance as a function of the beam photon energy E_{γ_B} and $\cos\theta_{\eta',CMS}$ of the reaction $\gamma p \rightarrow \eta' p \rightarrow \gamma\gamma p$ for 3PED (left) and 2PED events (right) and the butanol target.

A.6. The observable E for $\eta' \rightarrow \pi^0\pi^0\eta \rightarrow 6\gamma$

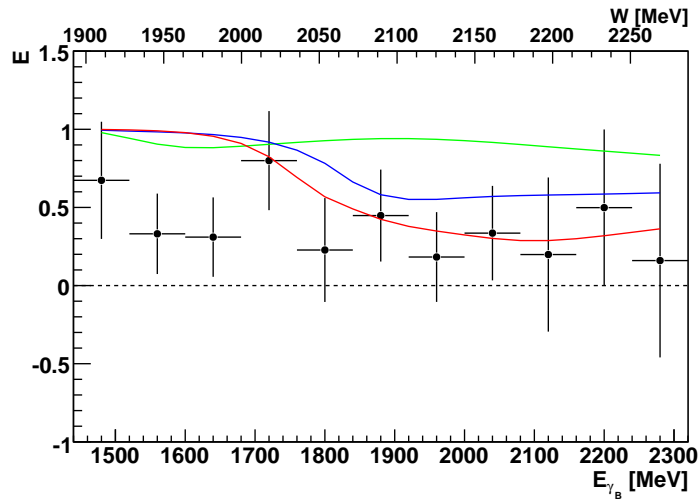


Figure A.6.: The observable E obtained from the decay mode $\eta' \rightarrow 6\gamma$. Exemplary, the second method was used to obtain the observable E. The predictions of the η' -MAID model are plotted as well [Tia07, Tia12].

A.7. Comparison of all methods

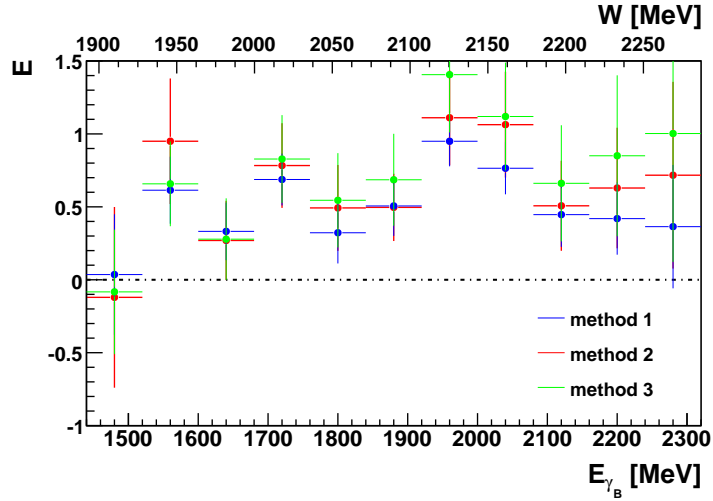


Figure A.7.: The comparison of all methods for the determination of E. The third method uses the fit result obtained from the CLAS cross section data.

List of Figures

1.1.	The strong coupling constant	1
1.2.	The nucleon excitation spectrum	2
1.3.	Feynman diagram of a photoproduction reaction	3
1.4.	Fits to CLAS and CBELSA/TAPS differential cross section data	7
1.5.	Fits to CLAS and CBELSA/TAPS cross section data	7
1.6.	Predictions of the η' -MAID model	9
2.1.	An overview of ELSA	11
2.2.	The goniometer and the energy dependency of the helicity transfer	13
2.3.	Schematic view of the tagging system	14
2.4.	The Møller polarimeter	15
2.5.	The butanol target	16
2.6.	Overview of the experimental CBELSA/TAPS setup	18
2.7.	Schematic view of the Inner detector	19
2.8.	The Cherenkov detector	21
3.1.	The invariant mass after the charge cut	26
3.2.	Time distributions of all particles	27
3.3.	Distribution of the reaction time	28
3.4.	Invariant mass after the time-cut	29
3.5.	The kinetic energy of the missing mass vs. the deposited energy of the measured proton	30
3.6.	The missing mass spectrum after applying all cuts	31
3.7.	The invariant mass spectrum after the missing mass cut	31
3.8.	The η' and proton momenta projected in the xy-plane	32
3.9.	The Φ -difference between proton and η'	33
3.10.	The θ -difference of the calculated and the measured proton	34
3.11.	The invariant mass after the coplanarity- and theta difference-cut	34
3.12.	The measured beam photon energy as a function of the calculated beam photon energy	35
3.13.	The invariant mass after the energy-cut	36
3.14.	The cut on the invariant mass	37
3.15.	The invariant mass distributions of η' and ω Monte Carlo data	37
3.16.	All possible combinations for the invariant mass of two of the six photons in the final state	39
3.17.	The energy, the missing mass, the Φ - and the θ -spectra are depicted for $\eta' \rightarrow 6\gamma$	40

3.18. The influence of the applied cuts on the invariant mass of $\eta' \rightarrow 6\gamma$	41
3.19. The combination of the six photons to $3\pi^0$	42
3.20. The influence of all cuts on the invariant mass ($\eta' \rightarrow 6\gamma$)	42
3.21. The invariant mass $m_{6\gamma}$ is plotted after all the applied cuts	43
3.22. The χ^2 distribution for four degrees of freedom	45
3.23. The invariant mass $m_{6\gamma}$ plotted after the kinematic fit and after each additional cut	46
3.24. A pull distribution before and after the cuts on the CL	47
3.25. The confidence level distributions for two different hypotheses	47
3.26. The invariant mass $m_{6\gamma}$ for both butanol and hydrogen data after the kinematic fit	48
3.27. The invariant mass distribution for the photoproduction reaction $\gamma p_{in} \rightarrow \pi^0 \pi^0 \eta p_{out}$	48
4.1. The possible spin configurations of beam photon and target proton	51
4.2. The countrate difference of the invariant mass spectra	52
4.3. The beam photon energy distributions for both spin configurations	53
4.4. The dependency of the countrate difference on the beam photon energy	53
4.5. The countrate difference in dependency of $\cos \theta_{\eta',CMS}$	54
4.6. The energy dependence of the polarization factor	54
4.7. The ratios of acceptances as a function of the beam photon energy for π^0 and η'	57
4.8. The scaled missing mass spectra for π^0 and η' photoproduction	58
4.9. The scaled missing mass spectra for π^0 and η' photoproduction	59
4.10. The ratios of acceptances for π^0 and η' over the entire angular range	60
4.11. The scaled missing mass spectra for four energy bins	61
4.12. The scaled beam photon energy distributions	61
4.13. The scaled $\cos \theta$ - distributions	62
4.14. The dilution factor in dependency of the beam photon energy	63
4.15. The dilution factor in dependency of $\cos \theta$	63
4.16. The observable E as a function of the beam photon energy obtained with method 1	64
4.17. The observable E as a function of $\cos \theta$ obtained with method 1	64
4.18. The photon flux for all four helicity configurations	66
4.19. The acceptance as a function of the beam photon energy	67
4.20. The acceptance as a function of $\cos \theta_{\eta',CMS}$ for four energy bins	67
4.21. The observable E as a function of the beam photon energy obtained with method 2	68
4.22. The observable E as a function of $\cos \theta$ obtained with method 2	68
4.23. The observable E as a function of the beam photon energy obtained with method 3	69
4.24. The observable E as a function of $\cos \theta$ obtained with method 3	70
4.25. Comparison of the results for the observable E obtained with three different methods	71
4.26. Comparison of the results for the observable E to the η' -MAID predictions	73

4.27. Comparison of the results for the observable E as a function of $\cos \theta$ to the η' -MAID predictions	73
4.28. The helicity dependent cross sections $\sigma_{1/2}$ and $\sigma_{3/2}$	75
A.1. An example for a xml file	79
A.2. The invariant mass of 2PED events	80
A.3. Pull distributions of all measured values	81
A.4. The observable E determined for $\gamma p \rightarrow \pi^0 p$ with method 1 and 2	82
A.5. The acceptance for 3PED and 2PED events	82
A.6. The observable E obtained from the decay mode $\eta' \rightarrow 6\gamma$	83
A.7. The comparison of all methods for the observable E whereas method 3 uses the CLAS cross section data	83

List of Tables

1.1.	All quantum numbers of initial, intermediate and final state	4
1.2.	Polarization observables	5
1.3.	Fit results of the η' -MAID model	8
2.1.	Overview of the different trigger conditions of trig42c	22
3.1.	The decay modes of η' with the corresponding branching ratios	23
3.2.	Analyzed data sets	24
3.3.	An overview of the used cut boundaries	40
4.1.	Fit results of the η' -MAID model	72
4.2.	Fit results of the Huang et al.	74

Bibliography

- [Aea92] E. Aker et al. The Crystal Barrel spectrometer at LEAR. *Nucl. Instrum. Methods Phys. Res.*, Sect. A 321:69–108, 1992.
- [BDS75] I. S. Barker, A. Donnachie, and J. K. Storrow. Complete Experiments in Pseudoscalar Photoproduction. *Nucl. Phys.*, B95:347–356, 1975.
- [Bea99] C. Bradtke et al. A new frozen-spin target for 4π particle detection. *Nucl. Instrum. Methods Phys. Res.*, Sect. A 436(3):430–442, November 1999.
- [Cea09] V. Credé et al. Photoproduction of η and η' Mesons off Protons. *Phys. Rev.*, C80:055202, 2009.
- [CGLN57] G. F. Chew, M. L. Goldberger, F. E. Low, and Y. Nambu. Relativistic dispersion relation approach to photomeson production. *Phys. Rev.*, 106(6):1345–1355, 1957.
- [CT97] Wen-Tai Chiang and Frank Tabakin. Completeness rules for spin observables in pseudoscalar meson photoproduction. *Phys. Rev.*, C55:2054–2066, 1997.
- [Dah08] Thomas Dahlke. *Bestimmung einer winkelabhängigen Energiekorrekturfunktion für das TAPS-Kalorimeter des Crystal-Barrel/TAPS-Experiments an ELSA*. Diploma thesis, Helmholtz-Institut für Strahlen- und Kernphysik, Rheinische Friedrich-Wilhelms-Universität Bonn, 2008.
- [Dea06] M. Dugger et al. η' Photoproduction on the Proton for Photon Energies from 1.527 to 2.227 GeV. *Phys. Rev. Lett.*, 96(062001):1–6, 2006.
- [Dre04] Peter Drexler. *Entwicklung und Aufbau der neuen TAPS-Elektronik*. PhD thesis, II.Physikalisches Institut, Justus-Liebig-Universität Gießen, 2004.
- [Dut11] H. Dutz. Privat communication, 2011.
- [Ebe06] Holger Eberhardt. *Messung der Targetpolarisation und Detektorstudie für das Møllerpolarimeter des Crystal-Barrel-Aufbaus an ELSA*. PhD thesis, Physikalisches Institut, Rheinische Friedrich-Wilhelms-Universität Bonn, 2006.
- [Eea68] R. Erbe et al. The Aachen-Berlin-Bonn-Hamburg-Heidelberg-München collaboration. *Phys. Rev.*, 175(1669), 1968.
- [Fas92] C. G. Fasano. Spin observables at threshold for meson photoproduction. *Phys. Rev.*, C46:2430–2455, 1992.

- [Fle01] Holger Flemming. *Entwurf und Aufbau eines Zellularlogik-Triggers für das Crystal-Barrel-Experiment an der Elektronenbeschleunigeranlage ELSA*. PhD thesis, Ruhr-Universität Bochum, 2001.
- [Fös00] Angela Fösel. *Entwicklung und Bau des Innendetektors für das Crystal Barrel Experiment an ELSA/Bonn*. PhD thesis, Friedrich-Alexander-Universität Erlangen-Nürnberg, 2000.
- [FP04] Kathrin Fornet-Ponse. *Entwurf eines Fokalebenendetektors für die Photonenmarkierungsanlage an ELSA*. Diploma thesis, Physikalisches Institut, Rheinische Friedrich-Wilhelms-Universität Bonn, 2004.
- [FP09] Kathrin Fornet-Ponse. *Die Photonenmarkierungsanlage für das Crystal-Barrel/TAPS-Experiment an ELSA*. PhD thesis, Rheinische Friedrich-Wilhelms-Universität Bonn, 2009.
- [Fun08] Christian Funke. *Analyse der Triggerfähigkeiten zur Selektion hadronischer Ereignisse und Entwicklung eines Hochgeschwindigkeits-Triggers für den Vorwärtskonus des Crystal-Barrel-Detektors*. PhD thesis, Rheinische Friedrich-Wilhelms-Universität Bonn, 2008.
- [Got] Manuela Gottschall. *Bestimmung der Doppelpolarisationsobservablen E für die Reaktion $\gamma p \rightarrow p\pi^0$ am CBELSA/TAPS-Experiment*. PhD thesis, Rheinische Friedrich-Wilhelms-Universität Bonn. In preparation.
- [Grü06] Marcus Grüner. Modifikation und test des innendetektors für das crystal barrel experiment. Diploma thesis, Helmholtz-Institut für Strahlen- und Kernphysik, Rheinische Friedrich-Wilhelms-Universität Bonn, 2006.
- [Ham09] Christian Hammann. *Aufbau eines Flüssigwasserstofftargets zur Durchführung von Kalibrationsmessungen am Crystal-Barrel Experiment an ELSA*. Diploma thesis, Helmholtz-Institut für Strahlen- und Kernphysik, Rheinische Friedrich-Wilhelms-Universität Bonn, 2009.
- [Har08] Jan Hartmann. *Zeitkalibrierung und Photonenflussbestimmung für das Crystal-Barrel-Experiment an ELSA*. Diploma thesis, Helmholtz-Institut für Strahlen- und Kernphysik, Rheinische Friedrich-Wilhelms-Universität Bonn, 2008.
- [HHN12] F. Huang, H. Haberzettl, and K. Nakayama. Combined analysis of η' production reactions: $\gamma N \rightarrow \eta' N$, $NN \rightarrow NN\eta'$, and $\pi N \rightarrow \eta' N$. *arXiv:1208.2279v1 [nucl-th]*, pages 1–18, 2012.
- [Hil00] Wolfgang Hillert. *Erzeugung eines Nutzstrahls spinpolarisierter Elektronen an der Beschleunigeranlage ELSA*. Habilitation thesis, Rheinische Friedrich-Wilhelms-Universität Bonn, 2000.
- [Hil06] W. Hillert. The Bonn Electron Stretcher Accelerator ELSA: Past and future. *Eur. Phys. J. A*, 28(s01):139–148, May 2006.

- [Jea11] I. Jaegele et al. Photoproduction of η' -mesons off the deuteron. *Eur. Phys. J. A*, 47(11):1–18, 2011.
- [Jun04] Jörg Junkersfeld. *Kalibration des Crystal-Barrel-ELSA Detektors mit Hilfe der Reaktion $\gamma p \rightarrow p\pi^0$* . Diploma thesis, Rheinische Friedrich-Wilhelms-Universität Bonn, 2004.
- [Jür12] Inke Jürgensen. Determination of the beam asymmetry σ in the reaction $\gamma c \rightarrow xp\pi^0$. Master’s thesis, Helmholtz-Institut für Strahlen- und Kernphysik, Rheinische Friedrich-Wilhelms-Universität Bonn, 2012.
- [Kai07] David Kaiser. *Aufbau und Test des Gas-Čerenkov-Detektors für den Crystal-Barrel-Aufbau an ELSA*. Diploma thesis, Helmholtz-Institut für Strahlen- und Kernphysik, Rheinische Friedrich-Wilhelms-Universität Bonn, 2007.
- [Kam09] Susanne Kammer. *Strahlpolarimetrie am CBELSA/TAPS Experiment*. PhD thesis, Rheinische Friedrich-Wilhelms-Universität Bonn, 2009.
- [KS03] B. Krusche and S. Schadmand. Study of Non-Strange Baryon Resonances with Meson Photoproduction. *Prog. Part. Nucl. Phys.*, 51:399–485, 2003.
- [Leo94] W. R. Leo. *Techniques for Nuclear and Particle Physics Experiments: A How-to Approach*. Springer-Verlag, second revised edition, 1994.
- [LMP01] U. Loering, B. C. Metsch, and H. R. Petry. The light-baryon spectrum in a relativistic quark model with instanton-induced quark forces: The non-strange baryon spectrum and ground-states. *Eur. Phys. J. A*, 10:395–446, 2001.
- [Mac97] M. MacCormick. Total photoabsorption cross section for 4He from 200 to 800 MeV. *Phys. Rev. C*, 55:1033–1038, 1997.
- [Nea98] S. Nakamura et al. Acceleration of polarized electrons in ELSA. *Nucl. Instrum. Methods Phys. Res., Sect. A* 411(1):93–106, July 1998.
- [Nov91] R. Novotny. The BaF₂ Photon Spectrometer TAPS. *IEEE Trans. Nucl. Sci.*, 38(2):379–385, 1991.
- [Nuh12] Patrick Nuhn. *Untersuchung von η' -Zerfällen mit dem Crystal-Barrel/TAPS-Detektor an ELSA*. Diploma thesis, Helmholtz-Institut für Strahlen- und Kernphysik, Rheinische Friedrich-Wilhelms-Universität Bonn, 2012.
- [Ols59] H. Olsen. Photon and Electron Polarization in High-Energy Bremsstrahlung and Pair Production with Screening. *Phys. Rev.*, 114(3), 1959.
- [PDG12] Particle Data Group PDG. 2012.
- [Pea98] R. Plötzke et al. Photoproduction of η' -mesons with SAPHIR. *Phys. Lett. B*, 444(555), 1998.
- [Pio07] Damian-Maria Piontek. *Entwicklung eines Online-Monitors für das Crystal-Barrel-Experiment an ELSA*. Diploma thesis, Helmholtz-Institut für Strahlen- und Kernphysik, Rheinische Friedrich-Wilhelms-Universität Bonn, 2007.

- [Roh03] Christian Rohlof. *Entwicklung polarisierter Targets zur Messung der Gerasimov-Drell-Hearn-Summenregel an ELSA*. PhD thesis, Rheinische Friedrich-Wilhelms-Universität Bonn, 2003.
- [Sea76] W. Struczinski et al. Study of Photoproduction on Hydrogen in a Streamer Chamber with Tagged Photons for $1.6 \text{ GeV} < E_\gamma < 6.3 \text{ GeV}$: Topological and reaction cross sections. *Nucl. Phys.*, B 108:45–47, 1976.
- [Tia07] L. Tiator. Photoproduction of Eta and Etaprime Mesons on the Nucleon. *Int. J. Mod. Phys.*, A22:297–304, 2007.
- [Tia12] Lothar Tiator. Privat communication, 2012.
- [vP03] Harald van Pee. *Untersuchung der Reaktion $\gamma p \rightarrow p\pi^0$ für Photonenenergien von 0.45 bis 1.3 GeV mit dem Crystal Barrel-Detektor an ELSA*. PhD thesis, Rheinische Friedrich-Wilhelms-Universität Bonn, 2003.
- [Wal07] D. Walther. Privat communication, 2007.
- [Wea09] M. Williams et al. Differential cross sections for the reactions $\gamma p \rightarrow p\eta$ and $\gamma p \rightarrow p\eta'$. *Phys. Rev.*, C 80(045213), 2009.
- [Wen04] Christoph Wendel. *Entwicklung eines Szintillations-Detektors zur Identifikation geladener Teilchen im Crystal-Barrel Vorwärtsdetektor*. Diploma thesis, Helmholtz-Institut für Strahlen- und Kernphysik, Rheinische Friedrich-Wilhelms-Universität Bonn, 2004.
- [Wen08] Christoph Wendel. *Design und Aufbau eines Szintillationsdetektors zur Identifizierung geladener Teilchen im Crystal-Barrel-Vorwärtsdetektor*. PhD thesis, Rheinische Friedrich-Wilhelms-Universität Bonn, 2008.
- [Win06] Alexander Winnebeck. *Entwicklung und Implementierung eines universellen, FPGA basierten Triggermoduls für das Crystal-Barrel-Experiment an ELSA*. Diploma thesis, Helmholtz-Institut für Strahlen- und Kernphysik, Rheinische Friedrich-Wilhelms-Universität Bonn, 2006.
- [Yea06] W.-M. Yao et al. The Review of Particle Physics. *J. Phys. G.*, 33, 2006.

Acknowledgement

“Nullum officium referenda gratia magis necessarium est.”

(Cicero, De officiis I, 15, 48)

First and foremost, I would like to express my utmost gratitude to my supervisor Prof. Reinhard Beck for giving me the opportunity to be part of his research group and entrusting me with a challenging project for my master's thesis. I am most grateful for his guidance and support throughout the last year.

I thank Prof. Dingfelder for accepting to be the second referee for this thesis.

I deeply thank Dr. Fei Huang and Dr. Lothar Tiator for providing me with fits and predictions that I could use for comparison.

My special thanks is forwarded to Dr. Annika Thiel for her continuous effort, patience and helpful advice.

I owe Manuela Gottschall a debt of gratitude for the fruitful discussions regarding the observable E and all the valuable suggestions she made.

Furthermore, I am grateful to Dr. Harald van Pee and Patrick Nuhn for their instructive advices concerning the use of the kinematic fit.

I thank Dr. Annika Thiel, Manuela Gottschall, Dr. Eric Gutz, Yannick Wunderlich and Inke Jürgensen for reading my thesis and giving me insightful comments.

Moreover, I would like to thank the whole group, especially Jorrit Drinhaus, Fahimeh Jahanbakhsh, Andreas Pitka, Viktor Ratza and once again Inke Jürgensen for the great time together.

Finally, I thank my parents and my sister for their support and encouragement. “You are my rock.” ;)

I hereby certify that the work presented here was accomplished by myself and without the use of illegitimate means or support, and that no sources and tools were used other than those cited.

Bonn,

Signature